Towards Geometrically Consistent Aerostructural Optimisation of Composite Aircraft Wings

Gillebaart, Erik

DOI
10.4233/uuid:a88f215a-3185-47ed-b3e4-bd309c4c8b34

Publication date
2018

Document Version
Final published version

Citation (APA)
Gillebaart, E. (2018). *Towards Geometrically Consistent Aerostructural Optimisation of Composite Aircraft Wings*. [Dissertation (TU Delft), Delft University of Technology]. https://doi.org/10.4233/uuid:a88f215a-3185-47ed-b3e4-bd309c4c8b34

Towards Geometrically Consistent Aerostructural Optimisation of Composite Aircraft Wings

Towards Geometrically Consistent Aerostructural Optimisation of Composite Aircraft Wings

Dissertation

for the purpose of obtaining the degree of doctor

at Delft University of Technology

by the authority of the Rector Magnificus, prof. dr. ir. T.H.J.J. van der Hagen,

chair of the Board for Doctorates

to be defended publicly on

Thursday 21 June 2018 at 12:30 o'clock.

by

Erik GILLEBAART

Master of Science in Aerospace Engineering

Delft University of Technology, the Netherlands

born in Heemskerk, the Netherlands.

This dissertation has been approved by the promotor and copromotor.

Composition of the doctoral committee:

Rector Magnificus,	chairperson	
Prof. dr. C. Bisagni,	Delft University of Technology,	*promotor*
Dr. R. De Breuker,	Delft University of Technology,	*copromotor*

Independent members:

Prof. dr. L.L.M. Veldhuis	Delft University of Technology
Prof. dr. E.H. van Brummelen	Eindhoven University of Technology
Prof. dr. W.R. Krüger	University of Berlin/DLR, Germany
Dr. B.K.S. Woods	University of Bristol, United Kingdom
Prof. dr. C. Vuik	Delft University of Technology, reserve member

This research work was supported by Delft University of Technology.

Keywords: Aeroelasticity, Aerostructural optimisation, Isogeometric analysis

ISBN 978-94-028-1081-3

An electronic version of this dissertation is available at
http://repository.tudelft.nl/.

SUMMARY

Air traffic has grown tremendously over the last century and is predicted to keep on growing at a rate of 4 to 5% per year for at least the next 20 years. Increasing air traffic also means increasing impact on the environment through the emission of greenhouse gasses and noise. The growing environmental awareness in society has lead to the formulation of a set of goals for the aerospace industry that are challenging, if not impossible, to achieve with the current aircraft development strategies. To significantly increase the efficiency of air transport, and thus decrease the environmental impact, radical new aircraft designs are necessary.

The traditional sequential design strategies do not allow for the proper trade-offs between the different disciplines involved in aircraft design. The traditional emphasis on aerodynamic performance of a wing, for example, may result in a heavier wing structure and as a consequence, a reduced overall performance when looking at the range or fuel consumption instead of only the drag. This problem can be overcome by using multi-disciplinary optimisation. Research done since the 1970's and 1980's has shown that significant improvements in aircraft performance can be obtained when aerodynamics and structures are designed in a simultaneous approach.

Typically, such multi-disciplinary optimisation frameworks use a number of different geometries and computational meshes for optimisation and analysis. Not only does this introduce extra computational cost, because information has to be transferred from one mesh to the other and back, but it also causes errors between the optimised and analysed geometries due to the approximative nature of these computational meshes. Furthermore, much of the research is limited in design freedom due to the use of the standard planform variables that describe the current generation aircraft wings. This obstructs the way towards disruptive new designs.

In the research presented in this dissertation, the goal was to remove these problems by developing a geometrically consistent aerostructural optimisation framework for the preliminary design of both conventional and non-conventional aircraft wings. The isogeometric analysis concept, a method where the analysis models use the same basis functions, and thus geometry, as those used in computer-aided design software, was identified as a potential solution to both issues. Implementing this method in both the aerodynamic and structural analysis models results in

a framework that uses the same geometry in optimisation and analysis, meaning no mesh generation or complex transfer algorithms are required. Furthermore, the computer-aided design geometries provide a smooth and flexible way of modifying the shape and thus automatically provides a basis for very broad shape optimisation.

The implementation of the isogeometric concept was first tested in a two-dimensional optimisation framework. An isogeometric boundary element potential flow solver was developed that uses the Greville abscissae for the collocation points. Multi-patch support was implemented to enable the analysis of more complex airfoil geometries. A Timoshenko beam model was coupled to the aerodynamic model through a coupling method based on gradient information related to the shared geometry for optimisation and analysis. A boundary layer model was added to estimate the viscous drag generated by the airfoil, as this is crucial for shape optimisation.

To demonstrate the complete two-dimensional optimisation framework, the landing performance of a morphing airfoil for a 25 kg UAV was optimised. A two-step optimisation approach was formulated in which in the first step the lift coefficient was maximised and in the second step the drag coefficient was included in the objective to ensure the airfoil was free of separated flow. The design variables consisted of the skin thickness and a version of lamination parameters suitable for describing the layup of beam structures. The actuation forces were also included as design variables. At this stage, the aerodynamic shape was optimised implicitly through the morphing design variables.

The optimisation of the airfoil, equipped with three actuators connecting the top and bottom skin behind the front spar, was performed multiple times with different sets of design variables. A clear trend was visible showing that including more design freedom resulted in more extreme landing configurations and higher lift coefficients. The inviscid results showed a maximum increase of 42% in lift coefficient when all design variables were included. The inclusion of the drag coefficient in the objective function in the second step of the optimisation indeed resulted in a design that did not suffer from flow separation in the most extreme landing configuration.

The experience and knowledge gained during the development of the two-dimensional aeroelastic optimisation framework were used in the next stage to create a more elaborate three-dimensional version. Again, an isogeometric boundary element potential flow model was selected as most suitable. A multi-patch formulation was developed to allow the analysis of more complex aircraft wing geometries and the Prandtl-Glauert correction was implemented to extend the validity of the model to higher subsonic flow conditions.

The Reissner-Mindlin shell theory was selected as most suitable for analysis of the multi-patch structural geometry. The isogeometric shell model combines naturally with the geometry representation and the aerodynamic boundary element model.

Lamination parameters were implemented to be able to vary the composite layups in a continuous fashion. To evaluate the failure of the composite material an existing Tsai-Wu failure envelope based on principle strains instead of stresses was implemented.

The aerodynamic geometry in the three-dimensional framework consists of only the outer mold line and the structural geometry of only the wingbox, making the coupling method developed in the two-dimensional framework cumbersome to use. Coupling the aerodynamic and structural models was thus done through a novel method based on radial basis function interpolation that properly deals with the non-interpolatory nature of the control points. The new coupling method was demonstrated to accurately transfer loads and displacements between the two models.

Besides the lift-induced drag provided by the potential flow model, the viscous drag was required for proper wing shape optimisation. The boundary layer model used in the two-dimensional framework was taken as the basis for a quasi-three-dimensional boundary layer model. Additionally, the buckling behaviour of the structural wingbox was analysed using an isogeometric plate buckling model. The buckling panels were modelled as simply-supported plates bordered by the ribs and stiffeners.

The three-dimensional isogeometric aeroelastic analysis framework was demonstrated through the analysis of the undeflected Common Research Model. Three different load cases were analysed. The cruise condition was analysed for aeroelastic deformation and boundary layer characteristics. The 2.5g pull-up and -1.0g push-down load cases were investigated for aeroelastic deformation and material and buckling failure. The presented results compared favourably with results from literature.

Implementation of the isogeometric aeroelastic model in an optimisation framework and application to the fully free optimisation of a rectangular wing exposed several challenges in the current implementation. Maintaining the mesh quality throughout the shape optimisation was found to be one of the main challenges. The non-smooth design sensitivities resulted in extreme local changes of the wing shape, resulting in severe distortion of the isogeometric mesh. Additionally, the discontinuous nature of the boundary layer model had a detrimental effect on the convergence of the optimisation and the low computational efficiency of the current implementation became more apparent in an optimisation environment. Potential solutions for these challenges were presented and discussed.

In conclusion, it was demonstrated that isogeometric analysis is a suitable approach to create a geometrically consistent aeroelastic analysis model. Implementation in an aerostructural optimisation framework for designing non-conventional aircraft wings, however, has exposed some shortcomings in the current implementation, but potential solutions were identified to overcome these challenges.

SAMENVATTING

Luchtverkeer is enorm gegroeid door de laatste eeuw heen en het wordt voorspeld dat het zal blijven groeien met 4 tot 5% per jaar voor ten minste de volgende 20 jaar. De toename in luchtverkeer betekent ook een toename van de invloed op het milieu door de uitstoot van broeikasgassen en lawaai. De toenemende aandacht voor het milieu in de samenleving heeft er voor gezorgd dat er een aantal doelen zijn geformuleerd voor de luchtvaart industrie die uitdagend, zo niet onmogelijk, te behalen zijn door middel van de huidige strategieën voor het ontwerpen van vliegtuigen. Om aanzienlijke verbeteringen te realiseren in de efficiëntie van het luchtverkeer, met als gevolg vermindering van de belasting van het milieu, zullen er ingrijpende nieuwe vliegtuig ontwerpen nodig zijn.

De traditionele sequentiële ontwerp strategieën staan het niet toe om de benodigde afwegingen te maken tussen de verschillende disciplines die een rol spelen binnen het ontwerpen van vliegtuigen. De nadruk die van oudsher op de aerodynamische prestaties wordt gelegd, kan bijvoorbeeld resulteren in een vleugelconstructie die zwaarder is met als gevolg verminderde prestaties als er naar het vliegbereik of brandstofverbruik wordt gekeken in plaats van naar alleen de weerstand. Dit probleem kan opgelost worden door gebruik te maken van multidisciplinaire optimalisatie. Onderzoeken gedaan sinds de jaren zeventig en tachtig van de vorige eeuw hebben aangetoond dat er aanzienlijke verbeteringen te behalen zijn als de aerodynamica en constructie tegelijkertijd worden ontworpen.

Zulke multidisciplinaire optimalisatie raamwerken gebruiken gewoonlijk een aantal verschillende geometrieën en discretisaties voor optimalisatie en analyse. Dit zorgt niet alleen voor extra rekenkundige kracht die nodig is om informatie tussen de verschillende discretisaties uit te wisselen, maar ook voor afwijkingen tussen de geoptimaliseerde en geanalyseerde geometrieën doordat dit soort discretisaties een benadering zijn van de daadwerkelijke geometrie. Veel van het bestaande onderzoek is bovendien gelimiteerd in ontwerpvrijheid vanwege het gebruik van standaard variabelen voor het beschrijven van het bovenaanzicht van de vleugel die gericht zijn op het ontwerp van de huidige generatie vliegtuigvleugels. Dit houdt de ontwikkeling van innovatieve nieuwe vleugelontwerpen tegen.

Het doel van het onderzoek dat in deze dissertatie wordt beschreven was om deze problemen weg te nemen door het ontwikkelen van een geometrisch consistent

optimalisatie raamwerk voor gelijktijdige optimalisatie van de aerodynamica en de constructie tijdens de voorontwerp fase van conventionele en onconventionele vliegtuig vleugels. Isogeometrische analyse is een methode die gebruikt maakt van dezelfde onderliggende wiskundige functies, en dus dezelfde geometrie, als die in computer-ondersteund ontwerpen worden gebruikt. De methode vormt een mogelijke oplossing voor de beschreven problemen. De implementatie van deze methode in zowel het aerodynamische als het constructiemodel resulteert in een raamwerk dat gebruik maakt van dezelfde geometrie in zowel de optimalisatie als de analyse. Er zal dus geen rekenkracht verloren gaan aan het creëren van discretisaties en het overdragen van informatie tussen de verschillende modellen. De computer-ondersteunde ontwerp geometrie voorziet bovendien in de mogelijkheid om de vorm van de vleugel vloeiend aan te passen over een breed bereik en vormt dus een goede basis voor uitgebreide vleugelvorm optimalisatie.

De implementatie van het isogeometrische concept is eerst getest in een tweedimensionaal optimalisatie raamwerk. Een isogeometrisch randelementen potentiaalstromingsmodel dat gebruik maakt van de Greville abscissen als *collocation* punten is ontwikkeld. De analyse van complexere vleugelprofielen is geïmplementeerd door middel van de toevoeging van ondersteuning voor geometrieën die uit meerdere stukken bestaan. Een Timoshenko balk model is gekoppeld aan het aerodynamische model door middel van een koppelingsmethode gebaseerd op gradiënt informatie gerelateerd aan de gedeelde geometrie voor optimalisatie en analyse. Een grenslaag model is toegevoegd om de viskeuze weerstand opgewekt door het vleugelprofiel te berekenen, omdat dit essentieel is voor de vorm optimalisatie.

Het tweedimensionale raamwerk is gedemonstreerd door middel van een toepassing in het optimaliseren van de landingscapaciteiten van een 25 kg zwaar onbemand vliegtuig door gebruik van *morphende* vleugelprofielen. Een twee-staps optimalisatiemethode is ontwikkeld waarin in de eerste stap de liftcoëfficiënt wordt gemaximaliseerd en in de tweede stap de weerstandscoëfficië}nt wordt toegevoegd in de doelfunctie om te zorgen dat er geen loslating voorkomt in de luchtstroming. De ontwerpvariabelen bestaan uit de huid dikte en een versie van laminatieparameters geschikt voor het beschrijven van het composieten laminaat voor balkconstructies. De *morphing* krachten zijn ook onderdeel van de ontwerpvariabelen. In deze fase van het onderzoek werd de aerodynamische vorm alleen geoptimaliseerd door middel van de ontwerpvariabelen die voor *morphing* gebruikt werden.

De optimalisatie van het vleugelprofiel, uitgerust met drie actuatoren die de huid achter de voorste langsligger aan de boven- en onderkant met elkaar verbinden, is meerdere keren uitgevoerd met verschillende combinaties van ontwerpvariabelen. Een duidelijke trend kon worden waargenomen waarbij het toevoegen van meer ontwerpvariabelen resulteerde in een extremere landing configuratie en hogere liftcoefficienten. De niet-viskeuze resultaten lieten een maximale toename in liftcoëfficiënt van 42% zien wanneer alle ontwerpvariabelen werden gebruikt in de optimalisatie. De toevoeging van de weerstandscoëfficiënt in de doelfunctie in

de tweede stap zorgde er inderdaad voor dat er geen loslating plaatsvond op het vleugelprofiel in de meeste extreme landingsconfiguratie.

De ervaringen en kennis opgedaan in de ontwikkeling van het tweedimensionale raamwerk is gebruikt in de volgende fase, waar een uitgebreidere versie voor driedimensionale problemen is ontwikkeld. Wederom is een isogeometrische randelementen potentiaalstromingsmodel gekozen als meest geschikt. Complexe vliegtuigvleugels behoren tot de analyse mogelijkheden door implementatie van de mogelijkheid om geometrieën bestaand uit meerdere stukken door te rekenen en de Prandtl-Glauert correctie is toegevoegd om de validiteit van het model uit te breiden naar hoog-subsonische snelheden.

De Reissner-Mindlin schaaltheorie was geselecteerd als de meest geschikte theorie voor de analyse van de vleugeldoos. Het isogeometrische schaalmodel vormt een natuurlijke combinatie met de representatie van de geometrie en het aerodynamische randelementen model. Laminatieparameters zijn geïmplementeerd om te zorgen dat de composieten laminaten op een continue manier gevarieerd kunnen worden. Om het falen van het materiaal te kunnen voorspellen is een Tsai-Wu bezwijkcriterium gebaseerd op de hoofdrekken in plaats van spanningen geïmplementeerd.

De aerodynamische geometrie in het driedimensionale raamwerk bestaat uit alleen de buitenste huid van de vleugel en de constructie geometrie uit alleen de vleugeldoos. Vanwege deze ongelijkheid in geometrie kan de koppelingsmethode ontwikkeld in het tweedimensionale raamwerk niet simpelweg gebruikt worden. Een nieuwe methode gebaseerd op radiale basis functie interpolatie is ontwikkeld die goed om kan gaan met de niet-interpoleerbare eigenschappen van de controle punten. Demonstratie van de nieuwe koppelingsmethode heeft aangetoond dat de krachten en verplaatsingen nauwkeurig worden overgegeven tussen de twee modellen.

Naast de lift geïnduceerde weerstand berekent in de potentiaalstromingsmodel, is ook de viskeuze weerstand nodig voor fatsoenlijke vleugelvorm optimalisatie. Het grenslaag model dat gebruikt werd in het tweedimensionale raamwerk is gebruikt om een quasi-driedimensionaal grenslaag model te creëren. Het knikgedrag van de vleugeldoos wordt bovendien geanalyseerd door een isogeometrisch knikmodel voor platen. Deze knik panelen worden gemodelleerd als vrij opgelegde platen omlijst door de dwarsliggers en verstijvers in de vleugel.

De mogelijkheden van het driedimensionale isogeometrische aeroelastische analyse raamwerk zijn gedemonstreerd door middel van de analyse van het *undeflected Common Research Model*. Drie verschillende belastingsgevallen werden geanalyseerd. De kruisvlucht omstandigheid werd geanalyseerd op het gebied van aeroelastische vervormingen en grenslaag gedrag. De 2.5g optrek- en -1.0g neerdrukcondities werden onderzocht op het gebied van aeroelastische vervormingen en materiaal en knik bezwijking. De gevonden resultaten waren vergelijkbaar met

resultaten gevonden in de literatuur.

Implementatie van het isogeometrische aeroelastische model in een optimalisatie raamwerk en toepassing op de volledig vrije optimalisatie van een rechthoekige vleugel onthulde een aantal uitdagingen die nog aanwezig waren in de huidige implementatie. Het behouden van de kwaliteit van de vermazing van de geometrie doorheen de gehele optimalisatie was een van de hoofduitdagingen gebleken. De piekerige ontwerpgradiënten resulteerden in extreme lokale veranderingen in vleugelvorm waardoor de vermazing zwaar vervormde. Een andere uitdaging was de discontinue eigenschap van het grenslaagmodel die een negatief effect had op de convergentie van de optimalisatie. De benodigde computerkracht vormde de laatste grote uitdaging. In een optimalisatie omgeving werd duidelijk dat de huidige implementatie relatief veel computerkracht vereist. Potentiele oplossingen voor deze uitdaging werden voorgesteld en besproken.

Concluderend kan er gezegd worden dat isogeometrische analyse succesvol is gebruikt om een geometrisch consistent aeroelastisch analyse model te creëren. Implementatie van dit model in een aerodynamisch en constructie optimalisatie raamwerk voor het ontwerp van onconventionele vliegtuigvleugels heeft echter laten zien dat er nog tekortkomingen zitten in de huidige implementatie, maar potentiele oplossingen zijn aangedragen om deze tekortkomingen te boven te komen.

NOMENCLATURE

ROMAN SYMBOLS

A	Cross-sectional area	m^2
A	Aerodynamic influence coefficient	
$\mathbf{A}$	Laminate in-plane stiffness matrix	N/m
$\mathbf{A_s}$	Laminate transverse shear stiffness matrix	N/m
b	Span	m
$\mathbf{B}$	Laminate coupling stiffness matrix	N
$\mathbf{B}$	Matrix with strain-displacement relations	
c	Chord	m
c_f	Skin friction coefficient	-
C	Boundary element jump term	
C_d	Section drag coefficient	-
C_D	Wing drag coefficient	-
C_l	Section lift coefficient	-
C_L	Wing lift coefficient	-
C_p	Pressure coefficient	-
C_T	Thrust specific fuel consumption	kg/N/s
$\mathbf{C}$	Material stiffness tensor	
d	Dimensionality	
$\mathbf{D}$	Laminate out-of-plane stiffness matrix	N m
E	Young's modulus	N/m^2
$\mathbf{f}$	Force vector	N
$\mathbf{F}$	Force vector	N
g	Gravitational acceleration	m/s^2
G	Fundamental solution	
G	Shear stiffness	N/m^2
$\mathbf{G}$	Normal velocity aerodynamic influence coefficient matrix	
h	Beam cross-sectional height	m
$\mathbf{H}$	Aeroelastic coupling matrix	

$\mathbf{H}$	Perturbation aerodynamic influence coefficient matrix	
I	Second moment of area	m^4
J	Jacobian	
$\mathbf{K}$	Stiffness matrix	
L	Lift	N
M	Mach number	
M	Mass	kg
n	Number of basis functions	
$\mathbf{n}$	Unit normal vector	
N	B-spline basis function	
p	Degree of basis functions	
p	Pressure	$\mathrm{N/m}^2$
$\mathbf{P}$	Control points	
Q	Velocity	m/s
r	Distance between two points	m
$\mathbf{r}$	Vector between two points	m
R	NURBS basis function	
R	Radius	m
R	Range	m
$\mathbf{R}$	Residual vector	
s	Curvilinear beam coordinate	m
S	Boundary surface	
S	Material strength in shear	$\mathrm{N/m}^2$
S	Surface area	m^2
t	Thickness	m
$\mathbf{t}$	Unit tangential vector	
$\mathbf{T}$	Transformation matrix	
u	Displacement	m
$\mathbf{u}$	Displacement vector	m
U	Elastic strain energy	N m
$\mathbf{U}$	Velocity vector	m/s
V	Potential energy	N m
V	Volume	m^3
w	Beam cross-sectional width	m
w	Control point weight factor	
$\mathbf{w}$	Mode shape	
W	Weight	N
x	Design variable	

x	x-coordinate	m
$\mathbf{x}$	Position vector	m
X	Material strength in 0-direction	N/m^2
y	y-coordinate	m
Y	Material strength in 90-direction	N/m^2
z	z-coordinate	m

Greek Symbols

α	Angle of attack	rad
α	Membrane beam lamination parameter	
β	Bending beam lamination parameter	
β	Prandtl-Glauert correction factor	
γ	Shear strain	-
Γ	Boundary	
ϵ	membrane strain	-
θ	Rotational deformation	rad
κ	Bending strain	-
λ	Eigenvalue	
ν	Poisson's ratio	-
ξ	Knot value	
Ξ	Knot vector	
Π	Total potential energy	N m
ρ	Density	kg/m^2
$\boldsymbol{\sigma}$	Normal velocity vector	m/s
ϕ	Perturbation velocity potential	m^2/s
$\boldsymbol{\phi}$	Perturbation velocity potential vector	m^2/s
Φ	Total velocity potential	m^2/s
χ	Bending strain	-
χ	Set of non-zero basis functions	

Sub/Superscripts

∞	Freestream conditions
0	Undeformed
a	Aerodynamic
b	Bending
b	Body surface

c	Compressive
C_0	C_0-continuous
m	Membrane
ref	Reference value
s	Shear
s	Structural
t	Tangential
t	Tensile
v	Viscous
w	Wake surface

Abbreviations

BEM	boundary element method
BIE	boundary integral equation
CAD	computer-aided design
CAE	computer-aided engineering
CFD	computational fluid dynamics
CRM	common research model
FEA	finite element analysis
FEM	finite element method
FFD	free form deformation
FSI	fluid-structure interaction
GCMMA	globally convergent method of moving asymptotes
IGA	isogeometric analysis
MDO	multi-disciplinary optimisation
MTOW	maximum take-off weight
NURBS	non-uniform rational b-splines
RANS	Reynolds-averaged Navier-Stokes
RBF	radial-basis function
SST	singularity subtraction technique
UAV	unmanned aerial vehicle
uCRM	undeflected common research model

CONTENTS

1 Introduction

Aircraft industry has grown tremendously in the 20th and 21st century, from the first flight of the Wright brothers to the multi-billion Euro industry it is today. A continued annual growth of 4 to 5 percent of the air traffic is predicted by Airbus for the foreseeable future, more than doubling the number of annual passenger kilometres within 20 years [1]. Whereas this growth is an opportunity from an economic point of view, it is problematic from an environmental standpoint.

The European Commission, together with key figures from the aircraft industry, formulated a set of, among others, environmental goals for the year 2050 for the aircraft industry [2]. These goals involve a 75% reduction in $C0_2$ and a 90% reduction in NO_x emissions per passenger kilometre compared to typical new aircraft in the year 2000. Achieving the aforementioned growth of the aircraft industry sector and at the same time accomplishing these challenging goals, requires significant technological advancements. The traditional incremental advances to the well-known "wing and tube" concept, observed in the last half a century, will have to make place for disruptive advances in aircraft design for the future generations of aircraft in order to significantly increase the likelihood of accomplishing these environmental goals.

Deviation from the "wing and tube" configuration renders large portions of the empirical data and knowledge currently used in aircraft design obsolete. Physics-based models are therefore necessary to fill up this void in knowledge and enable the design of new aircraft configurations. Traditionally, the disciplines involved in

the design process were relatively isolated from each other. The strive for lighter and, consequently, the trend towards more flexible structures and the increased use of composite materials, however, calls for a multi-disciplinary design and optimisation approach to ensure that the proper trade-offs can be made while considering the performance of the complete aircraft. A multi-disciplinary approach enables increased aircraft performance compared to the traditional design procedures where many disciplines are treated individually.

Multi-disciplinary design and optimisation of aircraft wings, specifically, is used to find the optimal aerodynamic shape and structural parameters at the same time. The aerodynamic and structural models typically have different requirements when it comes to their computational meshes. The difference can be found in, for example, mesh density, local refinements, or degree of the elements. The optimisation process, however, requires a single geometrical description. As a result, these optimisation frameworks typically use three different geometrical discretisations that need to be coupled to each in order to consistently transfer changes made to the optimisation model to the aerodynamic and structural computational meshes. This step can be computationally costly and may introduce geometrical errors in the computational meshes compared to the intended optimised geometry. These problems are more apparent when the optimisation process involves large changes in the wing shape. This explains why, generally, in existing research a limited set of variables for describing the shape is selected for optimisation. The range of possible geometries can in such a way be limited to ensure the shape modifications can be transferred to the analysis models relatively accurate.

These two problems can be avoided by ensuring the same geometrical description is used throughout the optimisation framework. Creating such a geometrically consistent framework can be achieved in one of two ways. A computational mesh can somehow be used as the geometrical description for the optimisation as well, or the optimisation model can be used directly as a mesh for the computational models. The first approach, although possible in a single-discipline optimisation, is infeasible for a multi-disciplinary optimisation because only one of the two computational meshes can be selected as geometrical description for the optimisation. The aforementioned problems will thus still occur when transferring the geometrical modifications from one mesh to the other. Additionally, this approach will remove any discrepancies between the optimisation and analysis models, but they will still differ from the exact geometry as described in a computer-aided design (CAD) model.

The second approach is more suitable for a multi-disciplinary framework, but requires a modification of the analysis methods. The methods can no longer use the conventional Lagrangian basis functions, but will have to be able to deal with, for example, B-splines or non-uniform rational b-splines (NURBS) basis functions, which are heavily used in CAD software. This is exactly what the isogeometric analysis (IGA) concept was developed for: to remove the gap between design and

analysis. IGA removes the necessity of a link between CAD and computer-aided engineering (CAE) since the exact model will now be available during the analysis. Mesh refinements or shape modifications, for example, can be directly done in the analysis environment, without the cumbersome process of going back to the CAD geometry first and generating a new mesh.

In the following two sections, an overview will be given of the state of the art of the two main research field relevant to this dissertation: aerostructural optimisation and isogeometric aeroelastic analysis. Subsequently, the goal and challenges of this research, as derived from the current state of the art, will be explained. Finally, the outline of this dissertation is presented.

1.1 MULTI-DISCIPLINARY WING DESIGN AND OPTIMISATION

The idea of combining structural and aerodynamic design of aircraft wings in a single multi-disciplinary optimisation (MDO) framework has received ample attention over the last half a century. The computational resources available to researchers has grown tremendously during this period, and alongside it a clear trend can be seen in the research on MDO of aircraft wings from simple one-dimensional to full computational fluid dynamics (CFD) and finite element method (FEM) models. In this section, an attempt is made to give an overview of how the field of aerostructural wing optimisation has progressed over the years.

The earlier work in the field focussed mainly on demonstrating the basic concept of applying this simultaneous aerodynamic and structural optimisation versus the traditional iterative, sequential strategy. Grossman et al. [3], for example, combined a lifting line aerodynamic model and a beam structural model to demonstrate that the results obtained with the combined optimisation strategy are superior compared to the sequentially obtained results. Due to the simplicity of the models, the design variables were limited to structural thickness and planform parameters. They applied their computational framework to the design of a sailplane wing and found that the integrated design approach was able to capitalise on favourable interactions between the aerodynamics and structure and in such a way increase the performance and, at the same time, lower the structural weight.

A similar fidelity-level was used in the work of Wakayama and Kroo [4, 5] to investigate the influences of various parameters, such as drag and weight, in the optimal planform of a subsonic wing. Although no structural design variables were included in the optimisation directly, the work can still be considered multi-disciplinary as a fully stressed and non-buckling structural design was obtained through several analytical constraint equations for the thickness of the wing panels. The results demonstrated that, in order to find sensible wing planforms, it is

necessary to take into account off-design conditions in the optimisation.

Grossman et al. [6] changed the aerodynamic model to a vortex lattice model and a more elaborate FEM model consisting of membrane, shear and rod elements in later work. The framework was used to design a wing for a transport aircraft. The more complex models increased the computational cost, so a more efficient method of computing the cross-disciplinary sensitivities and optimisation algorithm were introduced. A similar set of geometrical design variables as before was used and the structural ones were extended to take into account composite materials through a single ply orientation variable.

In these early stages, it was also recognised that to explore new aircraft configurations, MDO was of crucial importance. The work of Gallman [7], for example, explored the advantages of joined-wing aircraft using a framework consisting of vortex lattice aerodynamics and a structural beam model.

Later in the 1990's, as computational power grew rapidly, a transition towards higher-fidelity models occurred. The relatively simple lifting line or vortex lattice models were discarded in favour of Euler and Navier-Stokes models. The beam models had to make place for more complex finite element models. For example, Chattopadhyay and Pagaldipti [8] coupled a parabolised Navier-Stokes model to a box beam model and Baker and Giesing [9] combined an Euler model with a detailed FEM model. Both papers investigated the MDO of high speed civil transport aircraft. The increased computational expense of the more complex models was countered by innovations in sensitivity computations and more efficient optimisation formulations. Despite these efforts, the number of design variables had to remain very low, including only global shape parameters such as twist and sweep.

A different approach to include higher-fidelity models was presented by Giunta et al. [10]. Cheaper low-fidelity computational models were used to restrict the design space to the region of interest using a design of experiments approach. The points of interest were analysed using higher-fidelity models to build response surfaces for the actual MDO of the aircraft. This significantly reduced to computational cost and, furthermore, removed any computational noise present in the original models from the optimisation process.

Maute et al. [11] described an MDO framework consisting of Euler CFD and a detailed FEM model including spars, ribs, hinges and control surfaces. A simplified CAD model was used as an optimisation geometry, from which the computational meshes were derived. Despite the use of such a geometrical representation, the optimisation was still limited to only the sweep and twist, and the structural thicknesses of the wing. The analytical sensitivities were computed using different strategies. It was shown that the strategy using the exact sensitivities consistent with the aeroelastic model outperformed the alternative approximate strategies in the optimisation of the Aeroelastic Research Wing. The reduction in the num-

ber of iterations in the optimisation compensated for the increased computational cost of computing the exact sensitivities.

All the literature mentioned so far involves optimisations with a relatively low number of design variables. Especially the number of aerodynamic variables is kept low by only looking at planform parameters or global thickness to chord ratios. The reason behind this was computational cost, as was already mentioned. The step from finite-difference sensitivities to direct analytical sensitivities improved the situation, so that higher-fidelity models became feasible to use, but the computational cost still scales directly with the number of design variables. Shape optimisation of, for example, the outer mould line of the wing requires a relatively large number of design variables, which up to then was prohibitively expensive.

The introduction of the coupled-adjoint sensitivities in the high-fidelity aerostructural optimisation process meant that the number of design variables was no longer the main driver of the computational cost. The foundation of the implementation of the coupled adjoint was laid down by Reuther et al. [12] and Martins et al. [13] implemented the method and demonstrated the framework consisting of Euler or Navier-Stokes CFD and a FEM wingbox model. An aircraft wing was optimised for minimal drag using 10 variables for the wing twist and 180 variables for bump functions allowing actual shape optimisation of the outer mould line. In later work, the framework was used to optimise a supersonic business jet using 76 shape variables related to the twist, camber and bump functions of the wing and 10 structural thickness variables. Kreisselmeier-Steinhauser constraint aggregation functions were used to circumvent the problem of the adjoint sensitivity analysis now scaling with the number of constraint equations instead of the number of design variables. A 16% lower structural weight was found compared to the sequentially optimised aircraft.

The same computational framework, as presented in earlier work by Maute et al. [11], was extended to be able to use the coupled adjoint sensitivities as well [14]. The same wing optimisation case was used to demonstrate the accuracy of the new sensitivity analysis and, because the limit on the number of design variables was taken out, an outer mould line shape and thickness optimisation was performed. The stress constraints used previously were taken out to reduce the number of constraint equations and consequently the computational cost of the adjoint sensitivity formulation.

An MDO approach used in an industrial setting was presented by Piperni et al. [15]. A transonic small disturbance aerodynamic model was combined with a FEM model for the conceptual and preliminary design of a large business jet. Wing planform and airfoil shape variables and structural thickness variables were used in the optimisation. In a later development of the framework, an Euler/boundary-layer code was used instead of the transonic small disturbance model for high speed aerodynamics [16]. The low-speed performance was evaluated using a three-

dimensional panel code and a semi-empirical stall and post-stall model.

The European aerospace industry and research institutes have also presented various multi-disciplinary, multi-level and multi-fidelity aircraft design and optimisation frameworks [17, 18, 19]. The focus in these projects is often to maintain disciplinary design autonomy, so that the different design teams within an industrial setting (e.g. aerodynamic and structures) keep responsibility for their own design methodology. The frameworks are aimed to be used in a large part of the design process, from conceptual to detailed design. Consequently, different levels of fidelity are used in the analysis. The conceptual stage makes use of low-fidelity or (semi-) empirical tools, while in the later stages high-fidelity aerodynamic (Navier-Stokes, Euler) and structural (detailed FEM) models are used.

Martins and colleagues further improved their multi-disciplinary framework over the years. Kenway et al. [20] presented numerous computational improvements to the framework. By implementing more efficient algorithms and parallel computing capabilities, the computational efficiency was significantly improved. This was demonstrated by analysing the objective, constraints and sensitivities for an aircraft with more than 5000 design variables. The updated framework was used for the optimisation of a transport aircraft, taking into account multiple points in the flight envelope [21]. The free-form deformation method was used to parametrise the geometry and Euler CFD coupled to a detailed FEM wingbox model made up the aeroelastic analysis.

A similar aerostructural optimisation framework was presented by Zhang et al. [22]. Instead of the free-form deformation method, a B-spline parametrisation of the geometry was used for the shape optimisation. The parametrisation enabled an efficient and robust mesh movement algorithm that allows for large shape changes. The control points of the B-splines were used as shape variables in the optimisation, besides the structural thickness parameters, for aerostructural optimisation of a planar wing. The resulting drooped-wing concept improved the objective function by approximately 4%.

Most of the recent work on aerostructural optimisation focusses on increasing the fidelity-level and at the same time reducing the computational cost by implementing more efficient algorithms. However, it is also recognised that for preliminary design these high-fidelity optimisation frameworks are still prohibitively expensive as many different configurations have to be evaluated and optimised. Kennedy and Martins [23], for example, presented a framework consisting of a three-dimensional panel method with an empirical viscous drag prediction and a FEM wingbox model. The geometry is parametrised using the free-form deformation method, which would allow airfoil shape optimisation. In the presented work, however, the authors limit the optimisation to global wing shape parameters and structural thicknesses only.

Elham and van Tooren [24] described their low-fidelity framework consisting of a vortex lattice method coupled with a quasi-three-dimensional boundary layer model for drag computation and a beam FEM model. The geometry was parametrised using 6 planform design variables and 160 airfoil shape variables. The wingbox panel thicknesses were used as structural design variables. Kreisselmeier-Steinhauser functions were used for the constraint equations because adjoint sensitivities were computed.

1.2 ISOGEOMETRIC AEROELASTIC ANALYSIS

Isogeometric analysis (IGA), a term coined by Hughes et al. [25], is a method aimed at taking away the boundary between design and analysis. Instead of the conventional process, where the geometry created in a CAD environment has to be converted to analysis-suitable computational meshes, IGA provides a way to use the underlying CAD description in the analysis as well. The result is that, ideally, the CAD geometry can directly be transferred to the analysis framework and in such a way the exact geometry is available in the analyses models at all times. The main benefits are found in reduced computational effort, since the geometry does not need to be converted, and increased accuracy due to the use of the exact geometry in the analysis [26].

The application of IGA in the field of aeroelasticity is limited to the analysis of wind turbines. Most of the work comes from Bazilevs and co-workers and focusses on high-fidelity analysis of wind turbine. The earlier work used NURBS-based Navier-Stokes aerodynamics and Kirchhoff-Love shells with a matching interface [27, 28]. A framework based on T-splines and a non-matching fluid-structure interface enabled more tailored meshes for the two disciplines [29]. The computational model was extended to take into account the full wind turbine, including support and nacelle [30]. In later work, the framework was made suitable for the simulation of off-shore wind turbines by including the capability of free-surface fluid-structure interaction (FSI), which allows simulation of the interaction between the water and the support tower [31].

The recent work by Ferede et al. [32] on the analysis of wind turbine blades shows the implementation of IGA in the parametrisation of the geometry and the discretisation of the beam model that represents the turbine blade structure. The aerodynamics was represented by the standard blade element momentum theory. A conventional FEM shell model was added to analyse the stress response and buckling behaviour of the blade in more detail.

In the more general field of FSI, the IGA concept has been used in various fields of research. High-fidelity models have been used for the simulation of blood flow in blood vessels and bioprosthetics [33, 34, 35, 36, 37, 38]. The coupling of FEM

shell models with boundary element method (BEM) fluid models has recently gained more attention in an FSI application. Van Opstal et al. [39] and Heltai et al. [40] both used such a combination of Kirchhoff-Love shells and Stokes flow, demonstrating the favourable combination of the two types of discretisations.

1.3 GOAL OF THE RESEARCH

All of the references mentioned in section 1.1 share a common feature. A variety of geometries, parametrisations, discretisations and computational meshes is used throughout the optimisation frameworks. As mentioned before, this results in an extra computational burden for transferring data between different parts of the framework and induces geometrical errors in analysis and optimisation. Also, the generation of computational meshes from the parametrised geometry can be a costly step.

Additionally, in most of the recent literature, the parametrisation of the wing geometry is based upon the conventional planform variables such as span, sweep and taper, and a method for parametrising the airfoils in the wing. Although this works very well for aerostructural optimisation of conventional wing configurations, it prohibits the generation of innovative concepts that are essential for the progress of aircraft performance and the reduction of the environmental impact of the aerospace industry.

These two limitations in the current state of the art have resulted in the formulation of the following goal for this research:

> *Develop a preliminary wing design framework for geometrically consistent aerostructural analysis and optimisation that enables the design of non-conventional wing configurations.*

The IGA concept was identified as an ideal method for achieving this goal and was chosen as the route to take towards the geometrically consistent framework and the increased design freedom. The state of the art on isogeometric aeroelasticity only covers high-fidelity approaches, which would be computationally prohibitively expensive. As a result, the following challenges in achieving the aforementioned high-level goal were identified:

- Develop low-fidelity static aeroelastic analysis capabilities that are fully based on the IGA concept.
- Fit the aeroelastic analysis model in a geometrically consistent aerostructural optimisation routine that provides a high level of design freedom for exploring new wing configurations.

1.4 DISSERTATION OUTLINE

This dissertation is divided into one introductory chapter, three chapters comprising the main content of the dissertation, and one concluding chapter. The first chapter after the introduction covers a description and application of the two-dimensional isogeometric aeroelastic analysis and optimisation framework that was developed. An introduction into the IGA concept is given to make the reader familiar with the terminology. Subsequently, the implementation of the concept into a BEM potential flow model is described. It is explained how the conventional governing equations are modified to accept NURBS basis functions and the model is verified against reference solutions. Next, the structural model is presented. An overview of the linear curved Timoshenko beam model in the local reference frame is given, after which the modifications to express the model in a global reference frame are presented. The structural model is verified against some analytical benchmarks. The change of reference frame was required to accommodate the coupling of the aerodynamic and structural model based upon the gradient information obtained from the shared geometrical parametrisation. The missing viscosity in the potential flow model is compensated for by including a boundary layer model for the flow around the airfoil. The two-dimensional optimisation framework is demonstrated by applying it to the design of an actively morphing airfoil. The results of different optimisation cases are presented and discussed.

The third chapter covers the three-dimensional isogeometric aeroelastic analysis framework in a similar fashion as the second chapter. An explanation of the extension of the IGA concept into three-dimensional shells is given first. Subsequently, the aerodynamic model is presented. Contrary to the two-dimensional work, a stronger formulation of the Kutta condition had to be used in this model to ensure proper convergence of the pressure distribution at the trailing edge. The model was verified against solutions taken from the literature. The structural model described next is based on the Reissner-Mindlin theory as this provides both translational and rotational degrees of freedom, simplifying the multi-patch implementation compared to a Kirchhoff-Love implementation. Lamination parameters are employed to parametrise the composite material and allow for gradient-based optimisation of the layup of the composite material. The model was verified against a reference solution. A different coupling method compared to the two-dimensional work is presented. Although sharing the same model, the aerodynamic and structural analyses cover different parts of this model. As a result, a more elaborate coupling method is required where surface points are computed for evaluating the coupling matrix, which is subsequently projected back onto the control points. The coupled aeroelastic model is verified against a reference solution. The applicability of the framework is extended by including a quasi-three-dimensional boundary layer model and a plate buckling model. The resulting isogeometric

aeroelastic analysis framework is demonstrated in an application to the undeflected common research model (uCRM) wing model. Three different load cases are analysed and the results are discussed.

In the fourth chapter, a description of the geometrically consistent, fully free optimisation framework is given. The design case of a simple rectangular wing is presented, and the design sensitivities are verified through a comparison to finite difference sensitivities. The preliminary results of the optimisation are used to expose three main challenges that still remain in the current implementation. First, shortcomings in mesh quality maintenance are identified by investigating the shape sensitivity information and initial optimisation results. Two potential solutions are proposed for future implementation. Second, the boundary layer behaviour in the current framework is discussed and possible improvements are proposed. Third, the computational efficiency of the isogeometric aeroelastic analysis is reviewed, and possible measures are identified to reduce the computational cost.

Finally, this dissertation is concluded in chapter five. Conclusions are drawn about the work that is presented in this dissertation on the development of a geometrically consistent aerostructural optimisation framework. The goals formulated in the introduction of this dissertation are reflected upon. Besides the proposed improvements from chapter four, recommendations are made for extensions to the aerostructural optimisation framework for future work.

2

TWO-DIMENSIONAL ISOGEOMETRIC AEROELASTIC ANALYSIS AND OPTIMISATION [1]

Before diving into the full three-dimensional aeroelastic analysis and optimisation problem, a two-dimensional version of the framework is developed. The simpler geometry and computational models allow to built up experience and confidence in the isogeometric aeroelastic analysis and optimisation concept.

Low-fidelity models, although having a somewhat lower accuracy, can enable the use of extensive optimisation in early design stages. As was mentioned already in the introduction of this thesis, low-fidelity isogeometric aeroelastic analysis has been almost untouched, while, for example, aerodynamic analysis in the form of the BEM has been shown to be a suitable candidate for the implementation of IGA. The work of Politis et al. showed the application of IGA to exterior planar Neumann potential problems and they demonstrated superior convergence properties compared to a conventional BEM implementation [41]. Takahashi and Matsumoto demonstrated the application of the fast multipole method to the same type of problem, reducing the computational cost from quadratic to linear

[1] This chapter is largely based on the journal paper Gillebaart, E. and De Breuker, R. (2016). *"Low-fidelity 2D isogeometric aeroelastic analysis and optimization method with application to a morphing airfoil"*, Computer Methods in Applied Mechanics and Engineering, vol. 305, pp. 512-536.

with respect to the number of control points [42]. One of the most important challenges in BEM, computing the singular integrals, was tackled by Heltai et al. by desingularising the boundary integral equation. The application to 3D Stokes flow problems showed the accuracy of the method [43].

The fact that the BEM only requires a boundary description of the problem creates a perfect match with CAD, since the output of such software is only a boundary discretisation. Furthermore, analysing the exact geometry is beneficial for aerodynamic analysis, since small perturbations can have significant effects. Also in other fields it has been shown that the benefits of IGA work well in a BEM framework. Simpson et al. applied IGA to 2D elastostatic analysis [44] and later to acoustics, using T-splines instead of NURBS [45]. The elastostatic analysis was expanded to multipatch 3D analysis in the work of Lian et al. [46]. Scott et al. used T-spline instead of NURBS in 3D elastostatic analysis [47].

Another advantage of IGA is that it is very suitable for shape optimisation problems, especially in a BEM framework, as has been shown for structural shape optimisation in 2D, using a desingularised BEM formulation, by Lian et al. [48] and in 3D by Li and Qian [49]. The IGA implementation delivers very accurate shape sensitivities, resulting in precise optimisation results. Furthermore, the discretisation can be used directly in optimisation, removing the need for a separate shape parametrisation as demonstrated by Cho and Ha [50].

The benefits of the combination of CAD and BEM together with IGA are fully exploited in the aeroelastic framework presented in this chapter. An IGA potential flow solver is closely coupled to an IGA curved Timoshenko beam solver formulated in a global reference system. Subsequently, a one-way coupling is formed between the aeroelastic model and a boundary layer model. A gradient-based optimiser is used in combination with analytically computed sensitivities. To show the capabilities of the framework, it is applied to the aeroelastic optimisation of an active morphing airfoil.

The chapter is built up as follows. In Section 2.1 a short introduction into IGA is given, and the aerodynamic, structural and boundary layer models are described. The coupling of the models is also explained. The next section presents the design case of the morphing airfoil, together with the optimisation specifications. The results are presented and discussed in Section 2.3 and the chapter is summarised in Section 2.4.

2.1 COMPUTATIONAL TECHNIQUES

The low-fidelity aeroelastic framework consists of an isogeometric potential flow aerodynamic model and an isogeometric curved Timoshenko beam structural model. The flow diagram in Figure 2.1 shows the process of performing an aero-

structural optimisation. For the different parts of the process it is indicated what software is used. It starts with the development of the CAD geometry that will

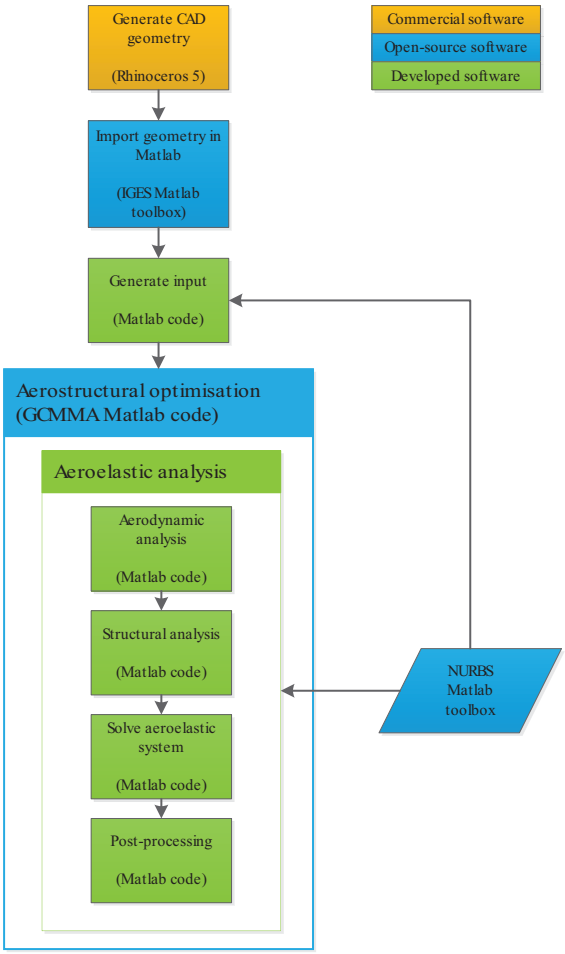

Figure 2.1: Flow diagram of the full aerostructural optimisation process

be used throughout the entire optimisation process. This is done in the commercial software Rhinoceros 5. The remainder of the process is performed in Matlab. The Matlab analysis code is developed by the author and is supported by three open-source Matlab codes. The IGES Matlab toolbox by Per Bergström is used to import the CAD geometry resulting from Rhinoceros 5 into Matlab. The GCMMA algorithm by Krister Svanberg is used for the optimisation and the NURBS Matlab toolbox by D.M. Spink is used for computing many things related to the NURBS functions, such as basis function values and derivatives.

This section will describe the theory and implementation of both the aerodynamic and structural model. The coupling between these models and the loads and displacements transfer method will also be presented. First a short introduction into NURBS and isogeometric analysis is given for completeness.

2.1.1 NURBS CURVES AND BASIS FUNCTIONS

In the present work NURBS basis functions are used, because these are the most common in CAD software. A NURBS curve is fully defined by three items:

- The control points $\mathbf{P}_i \in \mathbb{R}^d, 1 \leq i \leq n$, where d indicates the dimensionality of the problem.
- The degree p of the basis functions.
- The knot vector $\Xi = [\xi_1, \xi_2, ..., \xi_{n+p+1}]$.

An example of a two-dimensional NURBS curve of degree 3 is shown in Figure 2.2. From this example it can be seen that the control point may or may not

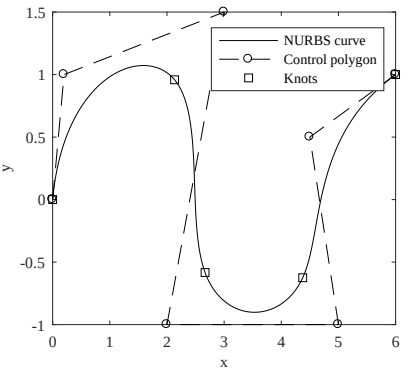

Figure 2.2: Example of a NURBS curve with control polygon and knot location

be on the curve. Only so-called open knot vectors are used in the present work, meaning that the first and last knots are repeated $p+1$ times. As a consequence the NURBS curve is always interpolatory at the start and end of the curve. The order of continuity of the rest of the curve can be modified by repeating the other knots. The order of continuity at a knot is equal to $p+1-r$, where r is the multiplicity of this knot.

Mathematically a NURBS curve can be represented as follows:

$$\mathbf{C}(\xi) = \sum_{i=1}^{n} R_{i,p}(\xi)\mathbf{P}_i \tag{2.1}$$

where $\mathbf{C}(\xi)$ is the vector with Cartesian coordinates of the point described by the parametric point $\xi_1 \leq \xi \leq \xi_{n+p+1}$, and $R_{i,p}(\xi)$ is the i^{th} rational basis functions of degree p. These basis functions are given by

$$R_{i,p}(\xi) = \frac{N_{i,p}(\xi)w_i}{\sum_{j=1}^{n} N_{j,p}(\xi)w_j} \tag{2.2}$$

where $N_{i,p}(\xi)$ is a B-spline basis function of order p, and w_i is the weight factor corresponding to the i^{th} control point. The B-spline basis functions of degree 0 are defined as

$$N_{a,0}(\xi) = \begin{cases} 1 & \text{if } \xi_i \leq \xi \leq \xi_{i+1} \\ 0 & \text{otherwise} \end{cases} \tag{2.3}$$

and for higher degrees

$$N_{i,p}(\xi) = \frac{\xi - \xi_i}{\xi_{i+p} - \xi_i} N_{i,p-1}(\xi) + \frac{\xi_{i+p+1} - \xi}{\xi_{i+p+1} - \xi_{i+1}} N_{i+1,p-1}(\xi) \tag{2.4}$$

The recursive character results in higher cost for computing the basis functions. However, several efficient algorithms exist to speed up the computations, of which the Cox-de-Boor algorithm [51] is most popular. This algorithm was also used in this work.

NURBS basis functions (as well as B-spline basis functions) possess some properties that are favorable for their implementation into analysis models. The basis functions possess the local support property, meaning that in every knot span $[\xi_i, \xi_{i+1})$ at most $p+1$ non-zero basis functions exist, namely $N_{i-p,p}, \ldots, N_{i,p}$. Furthermore, they are non-negative and form a partition of unity at each parametric location. In the interior of the knot span all derivatives of the non-zero basis functions exist and at a knot itself the functions are $p-r$ times continuously differentiable.

The principle of IGA, as was mentioned before, is to use the NURBS basis functions both for describing the geometry and to approximate the unknowns. For the aerodynamic model the unknowns are the doublet strength, as will be explained in Subsection 2.1.2, and for the structural model the unknowns are the displacements, as will be explained in Subsection 2.1.3. The power in this approach lies in the fact that the geometry and its boundary discretisation can be completely done in CAD software and this geometry can immediately be analysed in the IGA analysis software.

Even though the exact geometry is provided by the CAD software, the discretisation might not be detailed enough to enable the analysis to provide accurate results. This problem can be easily solved by either knot refinement or degree elevation, or a combination of both [26]. The computational algorithms to perform such operations on NURBS functions are well documented in literature [51]. The knot refinement and degree elevation operations have no effect on the geometry itself, making these operations efficient and simple.

2.1.2 AERODYNAMIC MODEL

The aerodynamic model is based on the potential flow model, which is characterised by Laplace's equation:

$$\nabla^2 \Phi^* = 0 \tag{2.5}$$

where Φ^* is the total velocity potential. The boundary conditions for the flow over an airfoil are the flow tangency condition at the boundary of the airfoil and that the disturbance of the flow should go to zero far away from the airfoil:

$$\frac{\partial \Phi^*(\mathbf{x})}{\partial \mathbf{n}} = 0 \text{ for } \mathbf{x} \in \Gamma_b \tag{2.6}$$

$$\lim_{r \to \infty} \nabla \Phi = 0 \tag{2.7}$$

where $\mathbf{n}$ is the outward unit normal vector to the boundary of the body Γ_b, r is the distance from the body, and Φ is the perturbation velocity potential. This problem is reduced to solving the following boundary integral equation (BIE) [52]:

$$C(\mathbf{x}_0)\Phi(\mathbf{x}_0) = \int_{\Gamma_b} \left(\frac{\partial \Phi(\mathbf{x})}{\partial \mathbf{n}(\mathbf{x})} G(\mathbf{x}_0, \mathbf{x}) - \Phi(\mathbf{x}) \frac{\partial G(\mathbf{x}_0, \mathbf{x})}{\partial \mathbf{n}(\mathbf{x})} \right) dS(\mathbf{x}) - \int_{\Gamma_w} \Delta\Phi(\mathbf{x}) \frac{\partial G(\mathbf{x}_0, \mathbf{x})}{\partial \mathbf{n}(\mathbf{x})} dS(\mathbf{x}) \tag{2.8}$$

where $\mathbf{x}_0$ is the point under consideration, $\mathbf{x}$ the point of integration on the surface of the body and the wake, C the jump term, Γ_w the wake surface, and G the fundamental solution as is given in Equation 2.9.

$$G(\mathbf{x}_0, \mathbf{x}) = \frac{1}{2\pi} \log \left(\frac{1}{|\mathbf{x}_0 - \mathbf{x}|} \right) \tag{2.9}$$

The normal derivative of the fundamental solution is given by

$$\frac{\partial G}{\partial \mathbf{n}}(\mathbf{x}_0, \mathbf{x}) = \frac{(\mathbf{x}_0 - \mathbf{x}) \cdot \mathbf{n}(\mathbf{x})}{2\pi |\mathbf{x}_0 - \mathbf{x}|^2} \tag{2.10}$$

Setting the normal derivative of the perturbation potential to zero and assuming the notation $C = C(\mathbf{x}_0), \Phi_0 = \Phi(\mathbf{x}_0), \Phi = \Phi(\mathbf{x}), G = G(\mathbf{x}_0, \mathbf{x}), S = S(\mathbf{x}), \mathbf{n} = \mathbf{n}(\mathbf{x})$, gives the following solution:

$$C\Phi_0 = -\int_{\Gamma_b} \Phi \frac{\partial G}{\partial \mathbf{n}} dS - \int_{\Gamma_w} \Delta\Phi \frac{\partial G}{\partial \mathbf{n}} dS \tag{2.11}$$

When the point $\mathbf{x}_0$ approaches point $\mathbf{x}$ on the boundary of the body, a singularity will be encountered. To desingularise Equation 2.11, the potential inside the body is investigated. The flow tangency boundary condition in Equation 2.6 implies that the potential inside the body is constant. Furthermore, the normal vector is

opposite compared to that of the external problem and the jump term becomes $1 - C$ [53]. The following equation thus holds for the interior problem:

$$1 - C = -\int_{\Gamma_b} \frac{\partial G}{\partial \mathbf{n}} dS \tag{2.12}$$

This relation is fully dependent on the geometry of the problem. Multiplying the equation with the total potential at point $\mathbf{x}_0$ and subtracting it from Equation 2.11 gives

$$\Phi_0 = \int_{\Gamma_b} (\Phi - \Phi_0) \frac{\partial G}{\partial \mathbf{n}} dS \tag{2.13}$$

which is no longer singular. Combining Equation 2.11 and 2.13 and introducing the free stream potential Φ_∞, gives the equation for the total velocity potential:

$$\Phi_0^* = -\int_{\Gamma_b} (\Phi - \Phi_0) \frac{\partial G}{\partial \mathbf{n}} dS - \int_{\Gamma_w} \Delta\Phi \frac{\partial G}{\partial \mathbf{n}} dS + \Phi_\infty \tag{2.14}$$

For the internal problem, the constant velocity potential is set to zero, which results in the final form of the problem that needs to be solved to find the velocity potential along the boundary:

$$-\int_{\Gamma_b} (\Phi - \Phi_0) \frac{\partial G}{\partial \mathbf{n}} dS - \int_{\Gamma_w} \Delta\Phi \frac{\partial G}{\partial \mathbf{n}} dS + \Phi_\infty = 0 \tag{2.15}$$

The velocity potential jump in the wake is related to the unknown velocity potential distribution on the body through the Kutta condition [54].

The geometry is now discretised using a NURBS curve and the unknown doublet strength is approximated using the same basis functions.

$$\mathbf{x}(\xi) = \sum_{i=1}^{n} R_{i,p}(\xi)\mathbf{P}_i; \quad \Phi(\xi) \approx \sum_{i=1}^{n} R_{i,p}(\xi)\Phi_i \tag{2.16}$$

Using the dot to indicate derivatives with respect to ξ to simplify notation, the Jacobian of the transformation from the Cartesian coordinate system to the parametric space becomes

$$J(\xi) = \sqrt{\dot{x}_1^2 + \dot{x}_2^2} \tag{2.17}$$

The non-zero knot spans in the knot vector of the curve can be considered as the elements that build up the geometry. The collocation method is used to set up a linear system of n equations for the $n+1$ unknown velocity potentials. The final equation is provided by the Kutta condition. The resulting system is as follows:

$$\begin{bmatrix} A_{1,1} & \cdots & A_{1,n} & A_{1,n+1} \\ \vdots & \ddots & \vdots & \vdots \\ A_{n,1} & \cdots & A_{n,n} & A_{n,n+1} \\ -1 & 0 & 1 & -1 \end{bmatrix} \begin{bmatrix} \Phi_1 \\ \vdots \\ \Phi_n \\ \Delta\Phi \end{bmatrix} = \begin{bmatrix} \Phi_\infty^1 \\ \vdots \\ \Phi_\infty^n \\ 0 \end{bmatrix} \tag{2.18}$$

where $A_{i,j}$ are the aerodynamic influence coefficients. The wake is modelled as a single element with a constant value, so its influence can be computed analytically. The other, non-singular, influence coefficients are computed numerically in the parametric domain. The integrals, as given in Equation 2.19, are computed using standard Gaussian quadrature. An adaptive scheme is used for the number of integration points to ensure accurate values for near-singular integrals. The number of integration points is increased as a collocation point is closer to the element over which the integral has to be computed.

$$A_{i,j} = \int_0^1 R_{j,p}(\xi) \frac{\partial G(\xi_i, \xi)}{\partial \mathbf{n}} J(\xi) d\xi \tag{2.19}$$

The desingularised contributions are computed by summing up the non-singular contributions and multiply it with the basis function values in the collocation point.

To find the pressure distribution over the airfoil the flow velocity tangential to the airfoil boundary has to be found. This is found by taking the derivative of the doublet strength in the tangential direction. In conventional panel methods the derivative has to approximated using a finite difference scheme, but since the NURBS curve representing the doublet strength is easily differentiable this can be done exactly:

$$Q_t = \frac{d\Phi}{ds} = \frac{1}{J}\frac{d\Phi}{d\xi} \tag{2.20}$$

The pressure distribution is now found using Equation 2.21

$$p = -\frac{\rho}{2}\left(Q_t^2 - Q_\infty^2\right) \tag{2.21}$$

where p is the pressure, Q_t the tangential velocity, and Q_∞ the free stream velocity. To find the force acting in the control points of the aerodynamic mesh, the pressure is integrated over the element e after multiplication with the corresponding non-zero basis functions in the set $\chi^{(e)}$:

$$\mathbf{f}_n^{\chi(e)} = \int_{\Gamma_e} p(\xi) \mathbf{R}_{\chi(e),p}(\xi) J(\xi) d\xi \tag{2.22}$$

The aerodynamic model is verified by comparing the results to those obtained using XFOIL [55]. XFOIL is also based on potential flow theory, but uses the traditional discretisation into linear panels. When using the inviscid solver within XFOIL, the same results as the model described before should be found. Figure 2.3 shows the pressure distribution obtained using the present model and XFOIL for a NURBS approximation of the NACA2412 airfoil at an angle of attack of 3 degrees. The control points and weights for the coarse mesh of the airfoil can be found in Appendix A. A good match is observed between the two distributions over the entire chord length. The lift coefficient of the same airfoil for an angle

of attack ranging from -8 to 8 degrees is compared in Figure 2.4. Again a good match is found. Comparison to the experimental results from Abbot and Doenhoff (1959) [56] shows that the inviscid results from both the present model and XFOIL have a slightly higher slope.

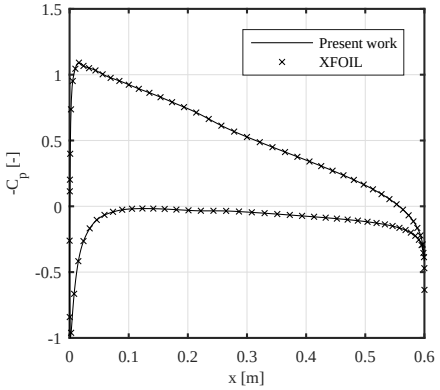

Figure 2.3: Comparison of results of the present aerodynamic model and XFOIL for the pressure distribution on a NACA 2412 airfoil at an angle of attack of 3 degrees

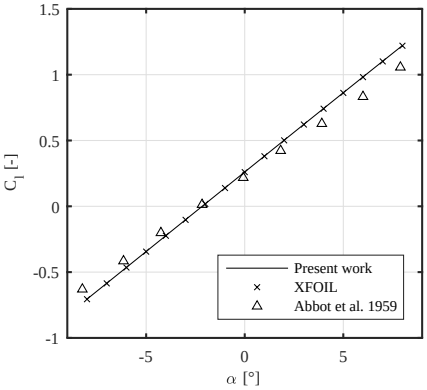

Figure 2.4: Comparison of results of the present aerodynamic model, XFOIL and experimental data for the lift coefficient of a NACA 2412 at various angles of attack

2.1.3 Structural model

The structural model is based on linear curved Timoshenko beams using an isogeometric formulation. Existing work in this field makes use of the local Frenet coordinate system to formulate the beam model [57, 58]. In the present framework, however, a global coordinate system was required to enable the transfer of loads from the aerodynamic model to the structural model and the displacements the other way around. For clarity first the formulation in the Frenet coordinate system is described, followed by the derivation of the formulation in the global coordinate system.

Local formulation

In the Frenet coordinate system, defined by the tangential, normal and bi-normal unit vectors $(\mathbf{t}, \mathbf{n}, \mathbf{b})$, the membrane, transverse shear and bending strain components of a planar curved beam are defined as

$$\varepsilon_m(s) = \frac{du_t(s)}{ds} - \frac{u_n(s)}{R(s)} \tag{2.23}$$

$$\gamma_s(s) = \frac{u_t(s)}{R(s)} + \frac{du_n(s)}{ds} - \theta_b(s) \tag{2.24}$$

$$\chi_b(s) = \frac{d\theta_b(s)}{ds} \tag{2.25}$$

where u_t, u_n and θ_b are the mid line tangential and normal displacements, and the cross-section rotation, respectively. They are all expressed in the curvilinear coordinate s, as shown in Figure 2.

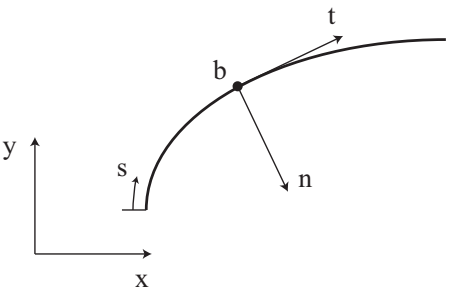

Figure 2.5: Curved beam coordinate systems

The total potential energy of the planar Timoshenko beam is the sum of the elastic strain energy U, and the potential energy of applied external forces V:

$$\Pi = U + V \tag{2.26}$$

$$U = \frac{1}{2}\int_0^L \left(EA{\varepsilon_m}^2 + GA\gamma_s^2 + EI\theta_b^2\right)ds \tag{2.27}$$

$$V = -\int_0^L (\mathbf{f}\cdot\mathbf{u})ds - \mathbf{F}\cdot\mathbf{u} \tag{2.28}$$

where E and G are the Youngs modulus and shear modulus respectively, A is the cross-sectional area and I is the moment of inertia along $\mathbf{b}$. The vectors $\mathbf{F}$, $\mathbf{f}$ and $\mathbf{u}$ are the concentrated loads, distributed loads, and displacements and rotations, respectively.

The IGA implementation starts with the representation of the geometry using NURBS curves. For simplicity the explanation will first be given for a geometry built up out of a single NURBS curve (single patch). The required modifications for a multi-patch geometry will be described later. The geometry is described by Equation 2.29, where the control points P_i contain the x and y coordinates.

$$\mathbf{x}(\xi) = \sum_{i=1}^{n} R_{i,p}(\xi)\mathbf{P}_i \tag{2.29}$$

Using the dot to indicate derivatives with respect to ξ to simplify notation, the Jacobian of the transformation from the Cartesian coordinate system to the parametric space becomes

$$J(\xi) = \sqrt{\dot{x}_1^2 + \dot{x}_2^2} \tag{2.30}$$

and the radius of the beam

$$R(\xi) = \frac{J^3}{|\dot{x}_1 \ddot{x}_2 - \ddot{x}_1 \dot{x}_2|} \tag{2.31}$$

The unknown displacements and rotations are approximated using the same basis functions as those that are used to describe the geometry:

$$u_t(\xi) \approx \sum_{i=1}^{n} R_{i,p}(\xi) u_t^i; \quad u_n(\xi) \approx \sum_{i=1}^{n} R_{i,p}(\xi) u_n^i; \quad \theta_b(\xi) \approx \sum_{i=1}^{n} R_{i,p}(\xi) \theta_b^i \tag{2.32}$$

In the parametric space the strains now become

$$\varepsilon_m(\xi) = \frac{\dot{u}_t}{J} - \frac{u_n}{R} \tag{2.33}$$

$$\gamma_s(\xi) = \frac{u_t}{R} + \frac{\dot{u}_n}{J} - \theta_b \tag{2.34}$$

$$\chi_b(\xi) = \frac{\dot{\theta}_b}{J} \tag{2.35}$$

Substituting Equations 2.32 to 2.35 in total potential energy equation and taking the second derivative of the strain energy U and the first derivative of the potential energy V with respect to the displacement and rotation control points, will result in the stiffness matrix, $\mathbf{K}$, and force vector, $\mathbf{f}$, respectively. The integrals are computed using Gaussian quadrature at the knot span level. The unknown displacements and rotations, $\mathbf{u}$, are found by simply solving $\mathbf{Ku} = \mathbf{f}$ and substituting the control point values in Equation 2.32.

When the geometry is more complex and cannot be described by a single NURBS patch, multiple patches have to be created and connected to each other. All the patches are interpolatory at the start and end of the curve, simplifying the process of connecting them. In the present work a master-slave technique is used to make sure the patches are connected properly and the redundant slave degrees of freedom are eliminated. The approach also allows connecting patches through hinges by only matching the displacement degrees of freedom between two patches and leaving the rotation degree of freedom as it is.

GLOBAL FORMULATION

To obtain a structural model in a global frame of reference some straightforward changes have to be made to the model described in the previous part. The tangential and normal displacements from the local coordinate system are expressed in the global x and y displacements:

$$u_t(\xi) = \mathbf{u}_g(\xi) \cdot \mathbf{t}(\xi); \quad u_n(\xi) = \mathbf{u}_g(\xi) \cdot \mathbf{n}(\xi) \tag{2.36}$$

where $\mathbf{u}_g$ is a vector with x and y displacements u and w, and $\mathbf{t}$ and $\mathbf{n}$ are the local tangential and normal vectors, respectively. These unit vectors are derived from the NURBS curve describing the geometry:

$$\mathbf{t} = \begin{bmatrix} \frac{\dot{x}_1}{J} \\ \frac{\dot{x}_2}{J} \end{bmatrix}; \quad \mathbf{n} = \begin{bmatrix} -t_2 \\ t_1 \end{bmatrix} \tag{2.37}$$

Substituting Equation 2.36 into the strain Equations 2.33 to 2.35, results in the strains in a global coordinate system:

$$\varepsilon_m(\xi) = \frac{\dot{\mathbf{u}}_g \cdot \mathbf{t} + \mathbf{u}_g \cdot \dot{\mathbf{t}}}{J} - \frac{\mathbf{u}_g \cdot \mathbf{n}}{R} \tag{2.38}$$

$$\gamma_s(\xi) = \frac{\mathbf{u}_g \cdot \mathbf{t}}{R} + \frac{\dot{\mathbf{u}}_g \cdot \mathbf{n} + \mathbf{u}_g \cdot \dot{\mathbf{n}}}{J} - \theta_b \tag{2.39}$$

$$\chi_b(\xi) = \frac{\dot{\theta}_b}{J} \tag{2.40}$$

The derivatives of the unit tangent and normal vectors are equal to

$$\dot{\mathbf{t}} = \begin{bmatrix} \frac{\ddot{x}_1}{J} - \frac{\dot{x}_1 \dot{J}}{J^2} \\ \frac{\ddot{x}_2}{J} - \frac{\dot{x}_2 \dot{J}}{J^2} \end{bmatrix}; \quad \dot{\mathbf{n}} = \begin{bmatrix} -\dot{t}_2 \\ \dot{t}_1 \end{bmatrix} \tag{2.41}$$

where the derivative of the Jacobian can be found with Equation 2.42:

$$\dot{J} = \frac{\dot{x}_1 \ddot{x}_2 + \ddot{x}_1 \dot{x}_2}{J} \tag{2.42}$$

The global displacements are again approximated by the NURBS basis functions:

$$u(\xi) \approx \sum_{i=1}^{n} R_{i,p}(\xi) u^i; \quad w(\xi) \approx \sum_{i=1}^{n} R_{i,p}(\xi) w^i \tag{2.43}$$

The stiffness matrix and force vector in the global coordinate system can now be found by taking the second derivative with respect to the displacements and rotations of the strain energy and the first derivative with respect to the displacements and rotations of the potential energy of the externally applied forces.

Verification of the structural model is performed by comparing its results to some analytical solutions obtained by Cazzani et al. (2014) [58]. The single patch implementation is tested using the vertically loaded cantilever arch shown in Figure 2.6. The radius R is 2 m, the Young's modulus is 80 GPa, and the Poisson's ratio is 0.2. The cross-section of the arch is rectangular with the thickness h equal to 0.01 m and the depth equal to 0.2 m. A vertical unit load P is applied at the tip of the arch. The vertical displacement at the tip of the arch is computed using the described structural model for an increasing number of elements. The convergence plot in Figure 2.7 shows that the displacement converges nicely to the analytical value.

The multi-patch implementation of the structural model is verified using the vertically loaded incomplete ring shown in Figure 2.8. The single patch making up

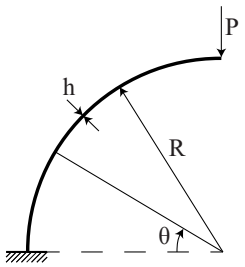

Figure 2.6: Sketch of the vertically loaded cantilever arch

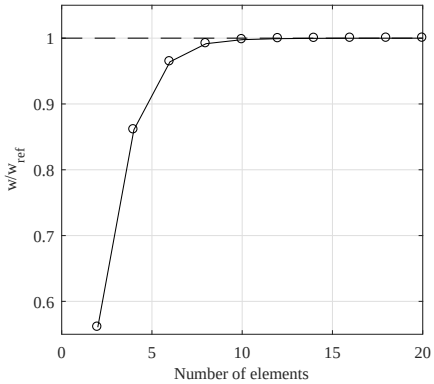

Figure 2.7: Convergence plot for the single patch cantilever arch

the geometry is split at point A to create two separate patches. The radius R is 2.935", the Young's modulus $1.05 \cdot 10^7$ psi, and the Poisson's ratio 0.3. The cross-section of the beam is rectangular with a thickness h of 0.125" and a depth of 1.2". The vertical displacement in point A is computed for an increasing num-

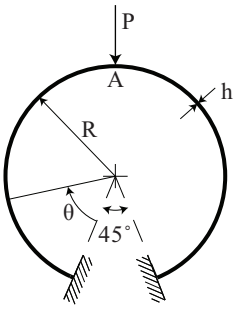

Figure 2.8: Sketch of the vertically loaded incomplete ring

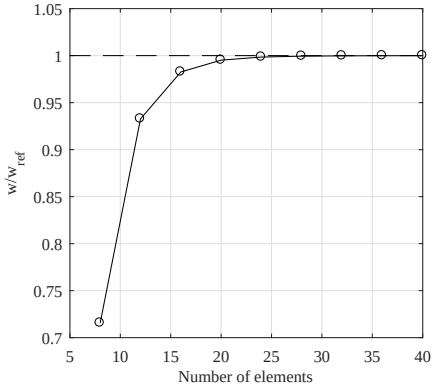

Figure 2.9: Convergence plot for the multi-patch incomplete ring

ber of elements and the convergence plot is shown in Figure 2.9. Again a nice convergence towards the analytical result is observed.

2.1.4 COUPLING

The aerodynamic and structural models are closely coupled, to enable fast computation of the converged solution. The coupling scheme is based on the conservation of energy, meaning that the virtual work, δW, done by the aerodynamic loads on the aerodynamic mesh should be equal to the work done by the equivalent set of loads on the structural mesh [59]:

$$\delta W = \delta \mathbf{u}^T \cdot \mathbf{f}_{aero} = \delta \mathbf{u}_a^T \cdot \mathbf{f}_{aero}^a \tag{2.44}$$

where $\delta \mathbf{u}$ and $\delta \mathbf{u}_a$ are the virtual displacements of the structural and aerodynamic control points and $\mathbf{f}_{aero}$ and $\mathbf{f}_{aero}^a$ are the aerodynamic forces acting on the structural and aerodynamic control points. To achieve a close coupling, a coupling matrix $\mathbf{H}$ is required which couples the aerodynamic displacements to the structural displacements:

$$\mathbf{u}_a = \mathbf{H} \cdot \mathbf{u} \tag{2.45}$$

Inserting Equation 2.45 into Equation 2.44 shows that in that case the following relation also holds:

$$\mathbf{f}_{aero} = \mathbf{H}^T \cdot \mathbf{f}_{aero}^a \tag{2.46}$$

Conventional methods for finding this coupling matrix, such as radial basis function interpolation, fail in the current work due to the fact that the control points of the IGA mesh are not always located on the boundary. In the present work both the structural mesh and aerodynamic mesh originate from a coarse initial mesh, as is illustrated in Figures 2.10 to 2.12.

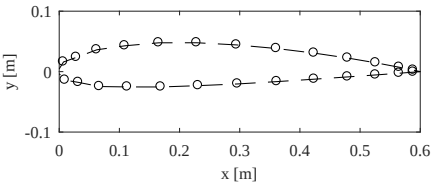

Figure 2.10: Example of a coarse control polygon

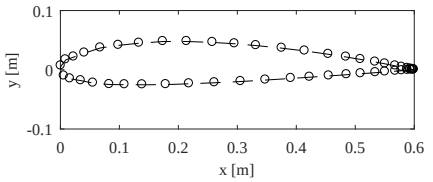

Figure 2.11: Aerodynamic mesh derived from the control polygon in Figure 2.10

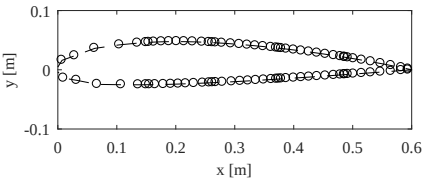

Figure 2.12: Structural mesh derived from the control polygon in Figure 2.10

To obtain the required coupling matrix the sensitivity matrices for the structural and aerodynamic mesh with respect to the coarse mesh are used. These sensitivity matrices describe how the control points in either the aerodynamic or structural mesh move as the control points in the coarse mesh are moved and can thus be used to link the aerodynamic displacements, $\mathbf{u}_a$, to the structural displacements, $\mathbf{u}$:

$$\mathbf{u}_a = \mathbf{H} \cdot \mathbf{u} = \frac{d\mathbf{P}_{aero}}{d\mathbf{P}_{struct}} \cdot \mathbf{u} = \frac{d\mathbf{P}_{aero}}{d\mathbf{P}_{coarse}} \cdot \left(\frac{d\mathbf{P}_{struct}}{d\mathbf{P}_{coarse}} \right)^{-1} \cdot \mathbf{u} \tag{2.47}$$

Both the aerodynamic and structural model are linear, so a single Newton-Raphson iteration gives the converged displacement field:

$$\begin{aligned} (\mathbf{K}_s - \mathbf{K}_a^s) \cdot \mathbf{u} &= \mathbf{f}_{aero,0}^s + \mathbf{f}_0 \\ \mathbf{K}_a^s &= \mathbf{H}^T \cdot \mathbf{K}_a \cdot \mathbf{H} \\ \mathbf{f}_{aero,0}^s &= \mathbf{H}^T \cdot \mathbf{f}_{aero,0} \end{aligned} \tag{2.48}$$

where $\mathbf{K}$ are the stiffness matrices and $\mathbf{f}_0$ any external force besides the aerodynamic load. The superscript s indicates that the values are in terms of the structural degrees of freedom and the subscript 0 indicates that the forces are those acting on the undeformed geometry. The converged aerodynamic forces are computed using the displacement field obtained by solving Equation 2.48:

$$\mathbf{f}_{aero} = \mathbf{f}_{aero,0} + \mathbf{K}_a \cdot \mathbf{H} \cdot \mathbf{u} \tag{2.49}$$

From these converged aerodynamic forces the lift coefficient can be determined, by taking into account the angle of attack.

2.1.5 Boundary layer model

To gain some insight in the viscous effects, such as drag and flow separation, a boundary layer model is coupled to the aeroelastic model described in the previous subsections. The input into this boundary layer model is the deformed geometry obtained from the aeroelastic analysis. A flow-chart of the system is given in Figure 2.13.

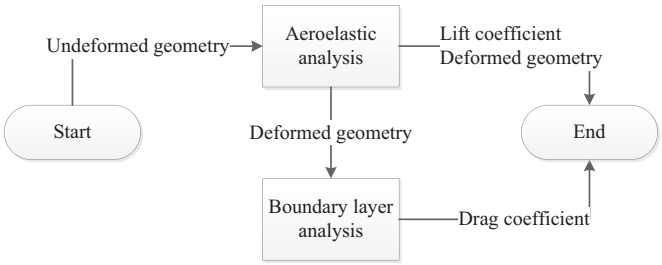

Figure 2.13: Flowchart of the analysis module

The deformed geometry is used to obtain the tangential velocity distribution along the boundary of the airfoil. Using a boundary layer model based on the one described by Moran [60], which is based upon several semi-empirical methods, the growth of the boundary layer along the airfoil is computed. The laminar part of the boundary layer is described by Thwaites' method and the turbulent part by Head's method. The transition between the two different flow states is determined using Michel's method. The tangential velocity distribution is discretised into small elements along the boundary and using these methods the development of the boundary layer is computed step-by-step from the front stagnation point to the trailing edge.

The main modifications compared to the original implementation are made in the transition and separation steps. To be able to use the drag coefficient in a gradient-based optimisation process the response surface should be continuous. Therefore, instead of only determining the element in which transition or separation occurs and assuming that the full element is turbulent or separated, an interpolation is done to find the location of transition or separation more accurately. This prevents any jumps in the response when the location switches from one element to the next.

The profile drag coefficient is subsequently determined using the Squire-Young formula, which takes into account the momentum thickness and displacement thickness at the upper and lower side of the trailing edge of the airfoil [61].

For verification of the boundary layer model, its results are compared to those obtained using XFOIL. The drag coefficient of a NACA2412 airfoil at an angle of attack ranging from 0 to 10 degrees at a Reynolds number of one million is computed using the presented boundary layer model and XFOIL. The results are shown in Figure 2.14. For this range of interest the results match quite well,

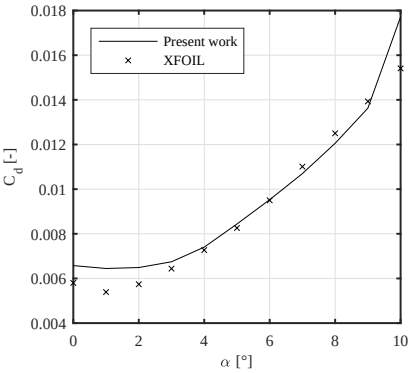

Figure 2.14: Comparison of results of the present boundary layer model and XFOIL for the drag coefficient of a NACA2412 airfoil for different angles of attack at a Reynolds number of one million

especially when realising that whereas XFOIL makes use of a two-way coupling of the aerodynamic and boundary layer model and a more sophisticated drag prediction, the present framework only uses a one-way coupling in combination with the Squire-Young formula. The deviation at higher angles of attack is probably caused by flow separation, as the results from the Squire-Young formula become inaccurate as soon as separation takes place. Most important is that the trend matches the XFOIL results, making the present implementation suitable for optimisation.

2.2 Morphing airfoil optimisation

The aeroelastic framework described in the previous section is applied to the optimisation of an active morphing airfoil. The goal is to morph the baseline airfoil shape, designed for optimal performance during cruise flight, into an airfoil shape more suitable for landing conditions. This means that the lift coefficient of the airfoil at a certain angle of attack needs to be maximised resulting in a reduced minimum landing speed and thus increased landing performance. In Subsection 2.2.1, a description is given for the design case, including the unmanned aerial vehicle (UAV) under consideration and the flight conditions of interest to the optimisation problem. Subsection 2.2.2 covers the setup of the optimisation problem. The objective, constraints and design variables will be presented.

2.2.1 Design case

The UAV considered for the optimisation has a mass of 25 kg and its wings are rectangular with the NACA2412 airfoil. The wingspan is 3.0 m and the chord length is 0.6 m. The cruise and landing flight conditions are listed in Table 2.1.

Table 2.1: Flight conditions for UAV in cruise and landing flight

		Cruise	Landing
Speed	[km/h]	110	56.02
Altitude	[m]	304.8	304.8
Angle of attack	[deg]	-	6.373
Lift coefficient	[-]	0.2425	-

The internal structure of the airfoil consists of a stiff wing box in the leading edge, with a single spar at 25.00% of the chord. The actuators are located at 43.75%, 62.50% and 81.25% of the chord and have a vertical orientation in the undeformed NACA2412 airfoil. The actuators are connected to the skin through hinges. Throughout all the analyses and optimisation runs the front spar of the airfoil is fully clamped. An illustration of the structure is shown in Figure 2.15.

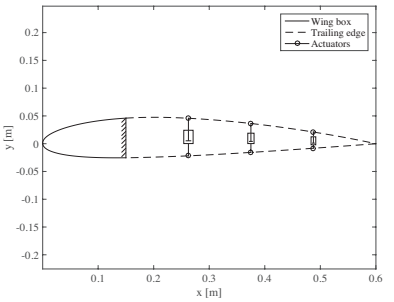

Figure 2.15: Geometry and internal structure of the morphing airfoil

2.2.2 OPTIMISATION SETUP

The main objective of the optimisation is to maximise the lift coefficient in landing flight conditions, while the NACA2412 geometry is maintained during other flight conditions. Without taking into account viscous effect, however, this would lead to infeasible results where flow separation would cause bad performance in landing conditions. The viscous effects are introduced into the optimisation by including the drag coefficient into the objective function. Instead of simply optimising the lift coefficient, the ratio of the lift and drag coefficient is optimised. The emphasis is put on the lift coefficient by raising it to a certain power. In the present work a power of 1.5 is used, which leads to realistic results where the influence of the lift coefficient is still dominating. This approach requires a two-step optimisation to avoid conservative results due to local minima present in the objective function, as is demonstrated in the next section.

Two separate analysis runs are done. One at landing conditions with the actuators enabled and one at 2.5g flight conditions with the actuators locked. Additional constraints are added to ensure a feasible design is found:

- Strain constraints are used for the airfoil skin in the morphing section. The IGA framework allows easy strain evaluations at any point on the geometry. In the present work the strain at 100 evenly spaced points were taken into account as constraints. The maximum allowed strain is 4000 microstrain.

- Constraints on the maximum actuation forces and maximum actuator strokes are implemented to avoid infeasible actuator requirements. The maximum value for the actuation force is set to 500N and the actuator stroke may be at most 40% of the initial length.

- When lamination parameters are included as design variables a set of constraint equations is implemented to ensure feasible laminate designs.

Besides the lamination parameters, the thickness and actuation forces are also included as design variables. The lamination parameters, however, deviate from the standard lamination parameters, because the current framework only covers two-dimensional problems. A modified set of lamination parameters is used to scale the membrane and bending stiffness of the laminate [62]:

$$EI = \alpha \frac{wh^3 E_{ref}}{12} \tag{2.50}$$

$$EA = \beta whE_{ref} \tag{2.51}$$

where h and w are the thickness and width of the laminate, and E_{ref} is the reference Young's modulus of the material. In the current work the modulus in the fibre direction of the material used in the optimisation, carbon fibre AS4/8773, was selected as the reference Young's modulus. The specifications of the material are given in Table 2.2.

Table 2.2: Material properties of carbon fibre AS4/8773

		AS4/8773
E_1	$[N/m^2]$	1.198×10^{11}
E_2	$[N/m^2]$	9.08×10^9
G_{12}	$[N/m^2]$	5.29×10^9
ν	[-]	0.32
t_{ply}	$[m]$	1.83×10^{-4}

A set of boundaries for the feasible design space was found by simply checking many different laminates and take the outer boundaries of the dataset. For unidirectional pre-impregnated carbon fiber in an epoxy material AS4/8773 the bounding box is created by the following equations:

$$\begin{aligned}
-\beta_i + 0.474\alpha_i + 0.0368 \leq 0, &\quad \text{for } i = 1 \dots N_p \\
\beta_i - 1.3013\alpha_i + 0.5656 \leq 0, &\quad \text{for } i = 1 \dots N_p \\
\beta_i - 9.4808\alpha_i + 8.8408 \leq 0, &\quad \text{for } i = 1 \dots N_p \\
-\beta_i + 0.4694\alpha_i + 0.5306 \leq 0, &\quad \text{for } i = 1 \dots N_p \\
-\beta_i + 1.2842\alpha_i + 0.2476 \leq 0, &\quad \text{for } i = 1 \dots N_p \\
\beta_i - 8.9981\alpha_i + 0.5595 \leq 0, &\quad \text{for } i = 1 \dots N_p
\end{aligned} \tag{2.52}$$

The design space of a laminate with fewer layers is conservative with respect to the design spaces of a laminate with more layers, so a minimum thickness can be chosen and the design space for this thickness can be safely used for thicker lamina as well.

The globally convergent method of moving asymptotes (GCMMA) [63] is used to perform the gradient-based optimisation. The objective, constraints and design variables are all normalised or scaled such that their magnitudes are similar. The

direct sensitivities are computed using algorithmic differentiation in all three models, ensuring efficient computation and accurate sensitivities [64]. The Karush-Kuhn-Tucker optimality conditions are used as convergence criterion.

Four different optimisation cases are studied in the present work.

- First of all, a baseline optimisation is done where only the actuation forces are included as design variables. The thickness for the baseline is chosen such that the cruise geometry can still be closely maintained during the 2.5g load case and is equal to 20 plies, or 3.66 mm. The laminate is set to a quasi-isotropic one by setting the lamination parameters to 0.5.

- The second optimisation also includes the thickness of the skin as design variable besides the actuation forces.

- The third case uses the actuation forces and lamination parameters to obtain an optimal result.

- The final optimisation includes all the design variables and should theoretically give the best result.

Table 2.3 gives and overview of the settings per optimisation case.

Table 2.3: Settings for the four optimisation cases

#		Skin thickness	Actuation forces	Lamination parameters
1	Baseline	3.66 mm	Free	a = b = 0.5
2	Thickness	Free	Free	a = b = 0.5
3	Laminate	3.66 mm	Free	Free
4	Thickness + laminate	Free	Free	Free

2.3 RESULTS

As was mentioned in the previous section, the drag coefficient was included in the objective function to ensure a feasible result without flow separation. To show the influence of the objective function formulation on the final morphed airfoil, both single step and double step optimisation approaches will be discussed. In the first subsection the single step optimisation approaches, using the inverse of the lift coefficient or the fraction of drag and lift coefficient as objective function, are presented . Subsequently, the final two-step optimisation formulation result is shown and the results for the four optimisation cases are presented and discussed.

2.3.1 SINGLE STEP OPTIMISATION

The single step optimisation approaches are only demonstrated for the fourth optimisation case, which includes both thickness and lamination parameters as design variables. The effect of the objective function will be most pronounced for this case. The results from the optimisation based on only the lift coefficient is presented first. Subsequently, the results from the optimisation using both drag and lift coefficient are presented.

$1/C_l$ MINIMISATION

In Figure 2.16 the deformed airfoil is shown. At the trailing edge a large deformation can be seen. This deformation causes the flow to separate, which is unfavourable during any flight condition. The lift coefficient for the deformed

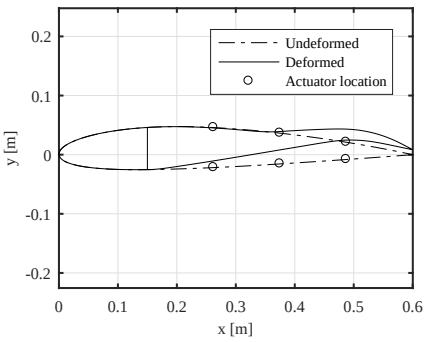

Figure 2.16: Deformed airfoil for lift coefficient maximisation for optimisation case 4

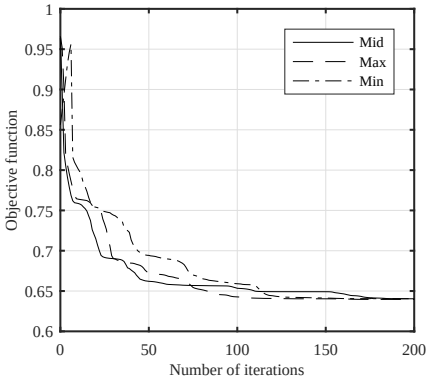

Figure 2.17: Objective function optimisation history for three different initial design variable sets for optimisation case 4

airfoil is 1.56 and the drag coefficient is equal to 0.0181.

The solution of this optimisation approach is insensitive with respect to the initial design vector. In Figure 2.17 the optimisation history of the objective function is shown for three different starting points. The solid line represents the starting point as mentioned in the previous section, with the design variables in the middle of their ranges. The dashed and dashed-dotted lines result from starting close at the maximum and minimum of the variable ranges, respectively. The figure shows that all optimisations converge to the same objective function value and on inspection of the resulting geometries it can indeed be concluded that the same solution has been found in all three cases.

$C_d/C_l^{1.5}$ MINIMISATION

Taking the objective function equal to $C_d/C_l^{1.5}$ results in a much more conservative solution. The increased complexity of the objective functions introduces more local minima, so the chances of the optimiser ending up in one of these minima is increased. The resulting deformation in Figure 2.18 indeed shows that the deformation is less pronounced compared to Figure 2.16. A lift coefficient of

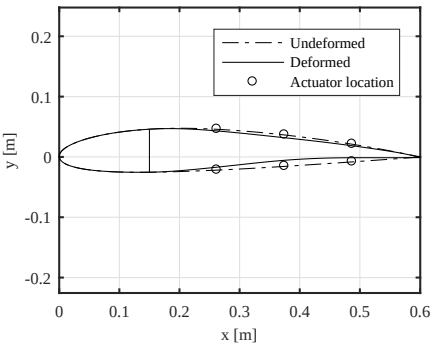

Figure 2.18: Deformed airfoil for $C_l^{1.5}/Cd$ maximisation for optimisation case 4

1.148 and a drag coefficient of 0.0106 is found for this airfoil.

2.3.2 TWO-STEP OPTIMISATION RESULTS

Neither of the morphing airfoils found in the previous subsection satisfy the requirements. The first airfoil experiences too much deformation, causing flow separation. The second airfoil is still far away from the possible increase in lift as demonstrated by the first airfoil. From these results the idea was formulated to create a hybrid two-step optimisation approach. The two steps are as follows:

1. The maximum possible lift coefficient is found by using the inverse of the lift coefficient as objective function.
2. From that point in the design space, the next optimisation step is started with the drag coefficient included in the objective function and the lift coefficient raised to the power 1.5.

The benefit of this approach is that it will be insensitive to the initial design vector, as was shown in Subsection 2.3.1. The second step is more sensitive to the starting design, but as this point is always the same this is not a problem.

The optimiser will thus find a solution close to the solution with the maximum lift coefficient, but a little bit more conservative to avoid flow separation.

This two-step optimisation approach is used for the four optimisation cases described in previous section. The results are presented in the remainder of this section. A summary of the optimisation results is given in Table 2.4. An increase in the lift and drag coefficient is observed for all designs compared to the NACA2412 airfoil. The optimisation histories for the objective function in the first and second optimisation step are collected in Figures 2.19 and 2.20. In

Table 2.4: Objective function and lift and drag coefficient for the NACA2412 and the four optimisation cases

	Objective function $[\cdot 10^{-3}]$	**Lift coefficient [-]**	**Drag coefficient [-]**
NACA2412	10	1.028	0.0105
Baseline	9.58	1.074	0.0107
Thickness	9.54	1.318	0.0144
Laminate	9.46	1.259	0.0134
Thickness + laminate	8.80	1.459	0.0155

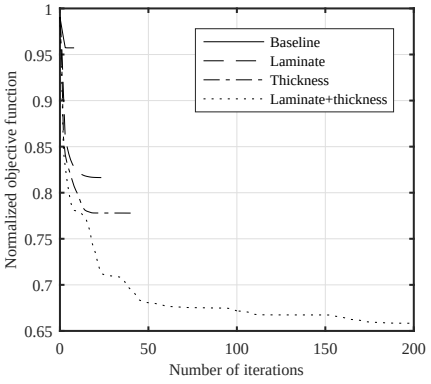

Figure 2.19: Objective function optimisation histories for the first optimisation step for the four cases normalised with respect to the undeformed NACA2412 performance

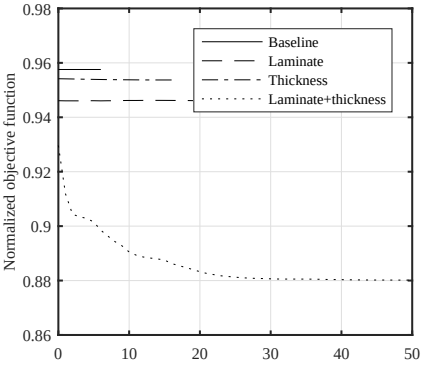

Figure 2.20: Objective function optimisation histories for the second optimisation step for the four cases normalised with respect to the undeformed NACA2412 performance

the first step the objective function converges faster as less design variables are involved. In the second step only the case with both the thickness and lamination parameters included changes significantly. The other cases were not able to achieve a solution with flow separation in the first optimisation step due to the bounds on the design variables. The minimum in the second step thus coincided with that of the first step. The combined effect of the thickness and lamination

parameters enables a more extreme deformation and thus results in flow separation and a large increase in drag in the first step.

In the following subsections more details will be given per design. First the baseline result is presented to understand what the performance of a non-optimised structure would be. The results of the other optimisation cases are compared with the baseline, but also with each other. Finally, the absence of flow separation is investigated.

BASELINE

The undeformed NACA2412 airfoil in landing conditions has a lift coefficient of 1.028 and a drag coefficient of 0.0105, resulting in a value of 0.01 for the objective function. For the baseline configuration only the actuation forces are optimised, as was explained before.

The resulting deformed shape with the constant skin thickness and quasi-isotropic layup is shown in Figure 2.21, together with the undeformed shape and actuator connection points.

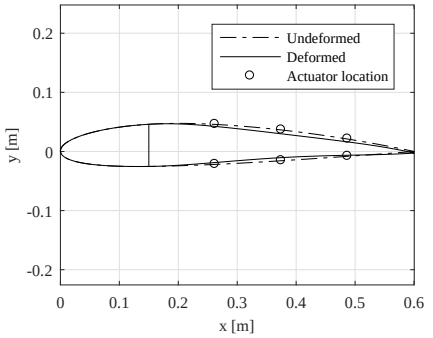

Figure 2.21: Baseline deformed and undeformed shape in landing flight conditions

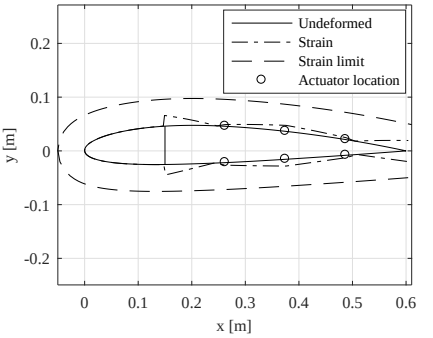

Figure 2.22: Strain in the skin of the baseline configuration

It is visible that the thickness of the trailing edge is decreased and the camber is slightly increased, which indeed results in an increase in lift coefficient. The objective function for the baseline case is equal to $9.58 \cdot 10^{-3}$, which translates into a lift coefficient of 1.074 and a drag coefficient of 0.0107. A slight increase in both lift and drag is thus achieved compared to the NACA2412 airfoil.

Because the thickness and lay-up is uniform throughout the skin, the deformation is almost symmetric. The actuation force in this case limits the deformation.

All three actuation force design variables are hitting their upper limit of 500N, preventing the optimiser to move towards more extreme camber lines. None of the other constraints are active. The cruise shape is maintained during the 2.5g load case. The strain in the skin is shown in Figure 2.22, which shows that it does not reach the limit anywhere. Similar as the deformation, the strain is also nearly symmetric on the upper and lower surface.

Skin thickness optimisation

Figure 2.23 shows the deformed shape resulting from the skin thickness optimisation. The actual skin thickness distribution is shown in Figure 2.24, where also the skin thickness of the baseline structure is shown for comparison. The variation in skin thickness allows the optimiser to introduce more camber compared to the baseline result. This results in an increased lift coefficient of 1.318, which is significantly higher than that of the NACA2412 and baseline airfoils.

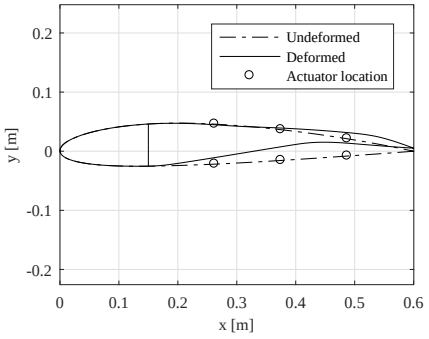

Figure 2.23: Thickness optimisation resulting deformation

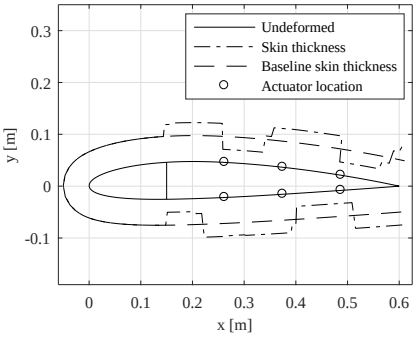

Figure 2.24: Thickness optimisation resulting thickness distribution

The thickness distribution shows that most of the thickness design variables are at their limit values. The thickness of the skin connected to the spar at the bottom side has the lowest thickness possible to introduce a compliant hinge. At the top the opposite is observed. The thickness is increased to the maximum value in order to maintain a stiff connection in this location. This allows for more camber to be introduced in the structure.

The middle and last actuators are at their maximum stroke and force, and the strain approaches the strain limit in most of the thin sections, as is shown in Figure 2.25. The cruise shape is again maintained during the 2.5g load case.

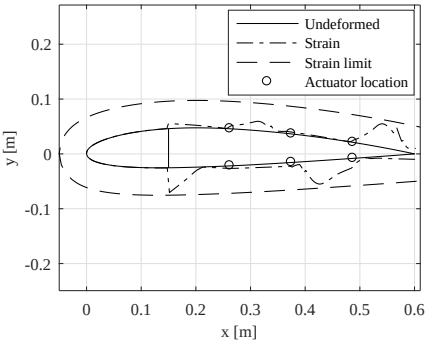

Figure 2.25: Strain in the skin of the thickness optimised configuration

LAMINATE OPTIMISATION

The skin deformation and lamination parameters for the laminate optimisation case are shown in Figure 7, and Figures 8 and 9, respectively. The deformation is again larger compared to the baseline, but less severe compared to the thickness optimisation case. This is also reflected in the resulting lift coefficient of 1.259, which is in between the baseline and thickness optimisation values.

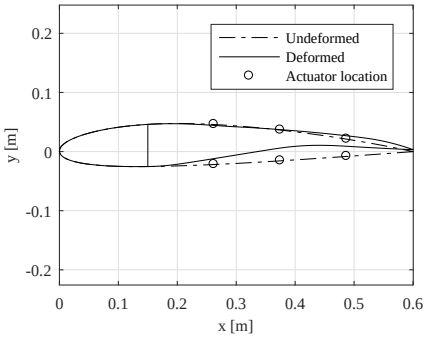

Figure 2.26: Laminate optimisation resulting deformation

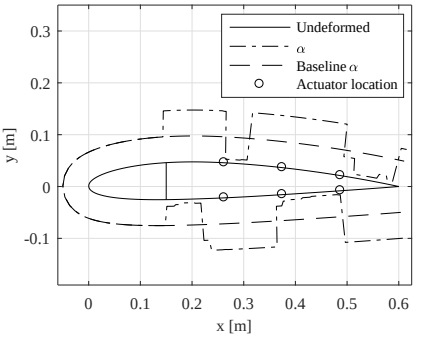

Figure 2.27: Laminate optimisation resulting α distribution

The lamination parameters both show similar behaviour as the thickness distribution in the previous case. The stiffness is strongly reduced and increased in same sections as where the thickness was reduced and increased in the previous results. The thickness, however, has a larger influence on the bending stiffness,

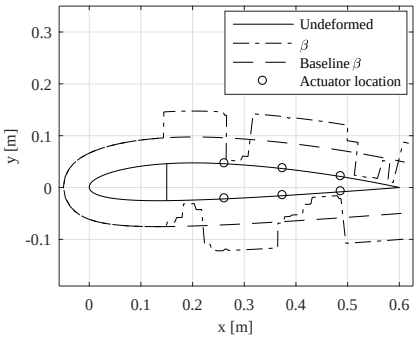

Figure 2.28: Laminate optimisation resulting β distribution

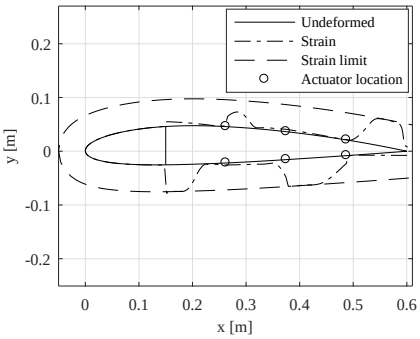

Figure 2.29: Strain in the skin of the laminate optimised configuration

explaining the larger displacement for the skin thickness optimisation.

Similar as to the previous results, the middle and last actuator reach their maximum stroke and force. Figure 2.29 shows that the strain limit is now reached in three out of four flexible sections. The cruise shape is maintained during the 2.5g load case.

Skin thickness and laminate optimisation

Figures 2.30 and 2.31 to 2.33 show the deformation and design variable distribution for the optimisation case with both the thickness and lamination parameters included as variables. The increased design freedom results in the highest lift coefficient of 1.459, achieved by the bigger displacement and larger curvature of the trailing edge compared to the previous results.

Contrary to the previous results, which showed very similar trends, this design case shows different behavior near the trailing edge. In the previous results both the upper and lower skin at the trailing edge were stiff, but in this case all design variables go the to minimum value on the upper side. When comparing the design variables within the optimisation case, it can be seen that the results are very similar in terms of stiff and compliant sections.

The actuator closest to the trailing edge reaches maximum force and stroke, while the one furthest away from the trailing edge reaches an actuation force of zero. The middle actuator exerts a force of approximately 215N. The strain in the skin close to the trailing edge reaches the limit, as well as the strain at the bottom of the spar. This is illustrated in Figure 2.34.

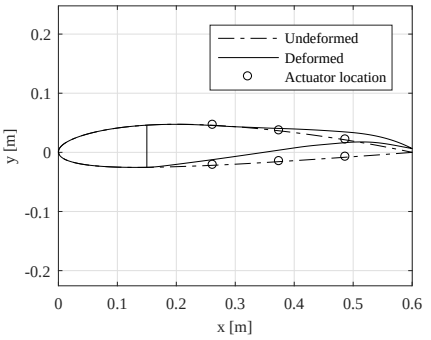

Figure 2.30: Thickness and laminate optimisation resulting deformation

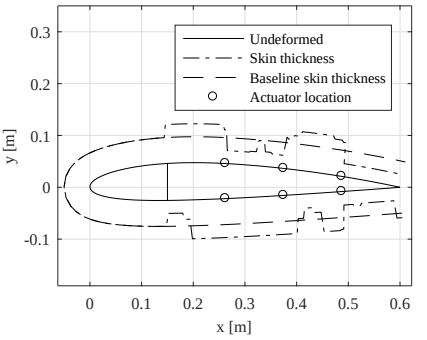

Figure 2.31: Thickness and laminate optimisation resulting thickness distribution

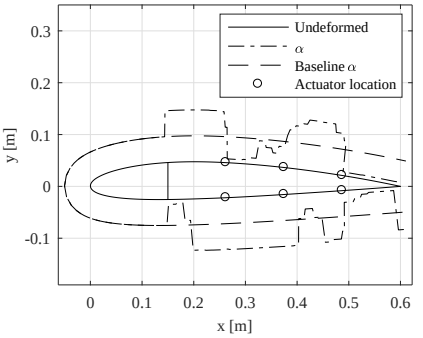

Figure 2.32: Thickness and laminate optimisation resulting α distribution

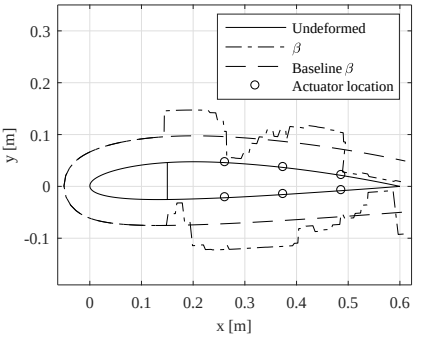

Figure 2.33: Thickness and laminate optimisation resulting β distribution

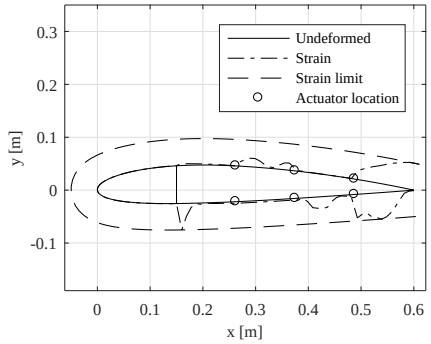

Figure 2.34: Strain in the skin of the thickness and laminate optimised configuration

2.3.3 Attached flow

The drag coefficient was added to the objective function to make sure the optimised results would be separation free, as was mentioned before. In Figure 2.35 the skin friction coefficient on the upper and lower surface of the last airfoil is shown, as computed by XFOIL. The curve for the upper surface clearly shows the transition point at around 14% of the chord, because the friction coefficient rises sharply at that point. On the bottom surface the same phenomenon can be observed at the transition point at around 69% chord. At the trailing edge the friction coefficient on the upper surface decreases towards zero, but is still slightly above. When the friction coefficient is equal to or lower than zero the flow has separated, so this shows that indeed no flow separation is taking place.

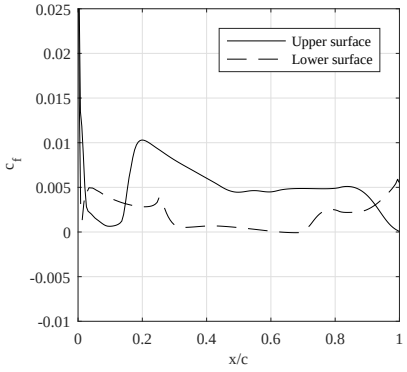

Figure 2.35: Development of skin friction coefficient in the boundary layer on the upper and lower surface of the airfoil with optimised skin thickness and laminate

2.4 SYNOPSIS

A two-dimensional low-fidelity isogeometric aeroelastic optimization framework was presented and applied to the optimization of an active morphing airfoil. The framework consists of an isogeometric BEM potential flow solver and an isogeometric curved Timoshenko beam solver, which are closely coupled. The coupling matrix is derived from the sensitivity matrices of the structural and aerodynamic control points with respect to a shared coarse control polygon. Both solvers make use of NURBS basis functions to describe the geometry and approximate the unknown variables. A boundary layer model is included in the framework to enable the computation of viscous effects.

The integrals for the aerodynamic model are desingularized, enabling easy calculation of the originally singular contributions to the aerodynamic influence coefficients. The multi-patch beam model is formulated in a global frame of reference to simplify the coupling to the aerodynamic model. The patches are connected through a master slave technique, enabling both rigid connections and hinged connections. The boundary layer model is based on existing semi-empirical integral methods improved with interpolation techniques to accurately determine points of flow transition or separation.

The aeroelastic optimization framework was used to optimize the landing performance of a 25kg UAV. The airfoil shape for cruise conditions was set to a NACA2412 and the goal was to maximize the lift coefficient during landing flight conditions by adding three actuators in the trailing edge of the airfoil and optimizing the skin thickness and lamination parameters. Four cases were optimized with varying design variables. To ensure feasible results without significant flow separation the drag coefficient was added to the objective function.

The results showed that higher lift coefficients were achieved, as more design variables were included, as was expected. The skin thickness was shown to be the most important design variable in the presented design case, because the structure is predominantly loaded in bending. The inviscid results showed an increase in lift coefficient of up to 42% for the case with both skin thickness and lamination parameter as design variables. Analysis of the airfoil in Xfoil showed that indeed no flow separation was taking place, caused by the use of the drag coefficient in the objective function.

3

THREE-DIMENSIONAL ISOGEOMETRIC AEROELASTIC ANALYSIS [1]

This chapter presents a further development of the 2D isogeometric aeroelastic analysis from the previous chapter and describes a geometrically consistent aeroelastic framework for the analysis of 3D aircraft wings. Adding an extra dimension of course calls for other aerodynamic and structural models. The potential flow BEM is still used for the aerodynamic part, but now for complete wings instead of just the airfoils. The structural beam model is replaced by a shell model. Similar as in the two-dimensional framework, the combination of these models with IGA creates a geometrically consistent analysis framework that can directly use the boundary representation obtained from CAD software. The two models are closely coupled through a radial-basis function (RBF) interpolation routine and in a post-processing step, the structural strength and buckling and the aerodynamic viscous drag are computed.

In Section 3.1 of this chapter, the computational models and techniques are described and their implementations are verified against reference solutions. In the next section the framework is demonstrated through the analysis of a realistic 3D wing. Three load cases are analysed and the results are discussed. Finally, a summary of the chapter is given.

[1] This chapter is largely based on the journal paper Gillebaart, E. and De Breuker, R. (2017). *"Geometrically consistent static aeroelastic simulation using isogeometric analysis"*, Computer Methods in Applied Mechanics and Engineering, under review.

3.1 COMPUTATIONAL TECHNIQUES

The isogeometric aeroelastic analysis method presented in this chapter consists of four distinct modules that interact with each other to find the final aeroelastic result. In Figure 3.1, an overview of the complete method with the internal interactions is presented to get a better understanding of how the model is assembled.

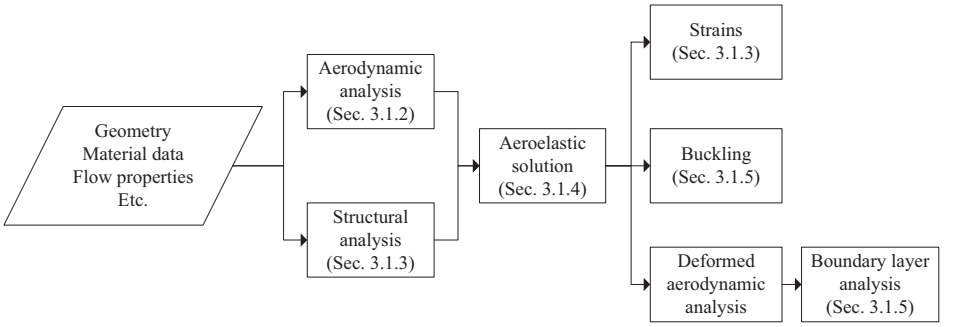

Figure 3.1: Overview of the isogeometric aeroelastic analysis framework

The flow diagram in Figure 2.1 presented in Section 2.1 also holds for the three-dimensional framework. The only difference is that instead of the GCMMA algorithm, the built-in Matlab function fmincon is used.

The main modules of the framework are the aerodynamic and structural ones, which are described in Subsections 3.1.2 and 3.1.3. These models are coupled to each other to enable the computation of the aeroelastic equilibrium, as explained in Subsection 3.1.4. The results from this aeroelastic analysis are used to compute the strains (Subsection 3.1.3), the buckling behaviour (Subsection 3.1.5) and the viscous drag of the aeroelastically deformed geometry (Subsection 3.1.5). First a short overview of the extension of the isogeometric principle to three dimensions is given in Subsection 3.1.1.

3.1.1 ISOGEOMETRIC ANALYSIS IN THREE DIMENSIONS

The same principles as shown in Chapter 2 for 2D NURBS curves hold for 3D curves, but also for surfaces, as will be used in the models presented later on in this chapter. A control net is obtained for a surface instead of the control polygon formed by the control points $\mathbf{P}_i$ for a curve. An additional knot vector $H = [\eta_1, \eta_2, ..., \eta_{n+q+1}]$ defines the bivariate NURBS surface of degree p in one direction and degree q in the other. An example is given in Figure 3.2

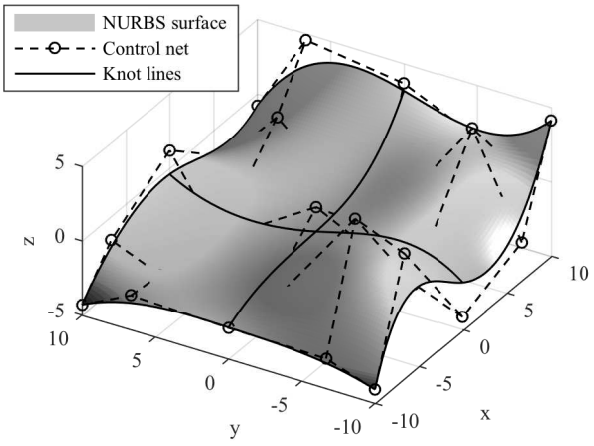

Figure 3.2: Example of a NURBS surface with control net and knot locations

3.1.2 AERODYNAMIC MODEL

The implementation of the aerodynamic model is based on the work by Kim et al. [65]. The potential flow model used for the hydrodynamic analysis of ship propellers in that work is in principle directly applicable to the aerodynamic analysis of aircraft wings. However, to enable the analysis of more complex wing models, multipatch analysis has to be added to the existing work. Furthermore, the Prandtl-Glauert correction is implemented in the model to extend the validity of the model up to high-subsonic Mach numbers. In the following subsection, a short overview of the aerodynamic model as presented by Kim et al. is given for completeness, together with the extension to multipatch analysis and the implementation of the Prandtl-Glauert correction.

The aerodynamic model is based on the potential flow theory, which assumes incompressible, inviscid and irrotational flow. A flow of this type is described by Laplace's equation. The boundary integral equation resulting from the flow tangency boundary condition is the governing equation for the flow around an wing:

$$\frac{\phi(\mathbf{x}_0)}{2} = -\iint_{S_b}\left(\phi(\mathbf{x})\frac{\partial G(\mathbf{x},\mathbf{x}_0)}{\partial \mathbf{n}} + \frac{\partial \phi(\mathbf{x})}{\partial \mathbf{n}} G(\mathbf{x},\mathbf{x}_0)\right)\mathrm{d}S - \iint_{S_w}\left(\Delta\phi(\mathbf{x})\frac{\partial G(\mathbf{x},\mathbf{x}_0)}{\partial \mathbf{n}}\right)\mathrm{d}S \quad (3.1)$$

where $\mathbf{x}$ are the boundary coordinates, $\mathbf{x}_0$ is a specific point on the surface, ϕ is the perturbation velocity potential, $\Delta\phi$ the potential jump in the wake, $\mathbf{n}$ the surface

unit normal, S_b and S_w the wing body and wing wake surfaces, respectively, and G the 3-dimensional fundamental solution of Laplace's equation:

$$G = \frac{1}{4\pi r} \tag{3.2}$$

where $r = |\mathbf{x} - \mathbf{x}_0|$ is the distance between the point of interest and the integration point. From the flow tangency boundary condition, the value for the normal derivative of the velocity potential can be found:

$$\frac{\partial \phi}{\partial \mathbf{n}} = -\mathbf{n} \cdot \mathbf{U}_\infty \tag{3.3}$$

where $\mathbf{U}_\infty$ is the freestream velocity vector.

The potential jump in the wake is constant in flow direction and is, according to the Kutta condition, equal to the jump in potential at the trailing edge of the wing, so the two surface integrals can be joined together. The isogeometric principle is invoked to discretise the geometry and the perturbation velocity potential as well as its normal derivative, leading to the following discretised boundary integral equation:

$$\frac{\mathbf{R}(\xi_0, \eta_0) \cdot \boldsymbol{\phi}}{2} + \frac{1}{4\pi} \iint_{S_b \cup S_w} \left(\mathbf{R}(\xi, \eta) \frac{\mathbf{n} \cdot \mathbf{r}}{r^3} \right) \mathrm{d}S \cdot \boldsymbol{\phi} = -\frac{1}{4\pi} \iint_{S_b} \left(\mathbf{R}(\xi, \eta) \frac{1}{r} \right) \mathrm{d}S \cdot \boldsymbol{\sigma} \tag{3.4}$$

where $\mathbf{R}$ is the matrix with NURBS basis function values, $\boldsymbol{\phi}$ and $\boldsymbol{\sigma}$ are the control points for the perturbation velocity potential and its normal derivative, and $\mathbf{r}$ is the vector, with length r, pointing from the integration point $\mathbf{x}$ to the surface point $\mathbf{x}_0$. At this stage the Prandtl-Glauert correction can be introduced. This is done through scaling the geometry in the flow direction by a factor $\beta = \sqrt{1 - M^2}$ in the integrals, where M is the Mach number:

$$\frac{\mathbf{R}(\xi_0, \eta_0) \cdot \boldsymbol{\phi}}{2} + \frac{1}{4\pi} \iint_{S_b \cup S_w} \left(\mathbf{R}(\xi, \eta) \frac{\mathbf{n}(\tilde{\mathbf{x}}) \cdot \mathbf{r}(\tilde{\mathbf{x}}, \tilde{\mathbf{x}}_0)}{r(\tilde{\mathbf{x}}, \tilde{\mathbf{x}}_0)^3} \right) \mathrm{d}S \cdot \boldsymbol{\phi} = -\frac{1}{4\pi} \iint_{S_b} \left(\mathbf{R}(\xi, \eta) \frac{1}{r(\tilde{\mathbf{x}}, \tilde{\mathbf{x}}_0)} \right) \mathrm{d}S \cdot \boldsymbol{\sigma} \tag{3.5}$$

where the overhead tilde indicates the coordinates scaled in flow direction by a factor β.

The surface integrals are broken up into the elements that are formed by the non-zero knot spans in the parametric domain. The higher-order discretisation prohibits the use of analytical expressions for the integrals, so Gaussian quadrat-

ure is used to evaluate them numerically. The resulting equation is

$$\frac{\mathbf{R}(\xi_0,\eta_0)\cdot\boldsymbol{\phi}}{2}+\frac{1}{4\pi}\left[\sum_{i=1}^{n_e}\sum_{g=1}^{n_{gp}}\mathbf{R}(\xi_g,\eta_g)\frac{\mathbf{n}(\xi_g,\eta_g)\cdot\mathbf{r}(\xi_g,\eta_g)}{r(\xi_g,\eta_g)^3}J_1(\xi_g,\eta_g)J_g w_g\right]\cdot\boldsymbol{\phi}$$
$$=-\frac{1}{4\pi}\left[\sum_{i=1}^{n_e}\sum_{g=1}^{n_{gp}}\mathbf{R}(\xi_g,\eta_g)\frac{1}{r(\xi_g,\eta_g)}J_1(\xi_g,\eta_g)J_g w_g\right]\cdot\boldsymbol{\sigma} \quad (3.6)$$

where n_e and n_{gp} are the number of elements and Gaussian quadrature points per element, J_1 the Jacobian for the transformation from the physical to the parametric domain, J_g the Jacobian for the transformation from the parametric to the parent domain in which the Gaussian quadrature points are defined, and w_g the quadrature weights. Equation 3.6 can be rewritten in short as

$$\mathbf{h}\cdot\boldsymbol{\phi}=\mathbf{g}\cdot\boldsymbol{\sigma} \quad (3.7)$$

The integrals are unfortunately not well behaved as the surface point $\mathbf{x}_0$ approaches the integration point. In the limit, they even become singular since the distance r will go to zero. Special care has to be taken in computing these integrals to be able to obtain accurate results. The singular integrals are computed by splitting the singular element into four triangular elements originating from the singular point to the four corner points. A quadratic transformation is applied to introduce a Jacobian that is zero in the singular point and thus cancels the singularity. The sum of the four triangular integrals will give an accurate result for the integral. For the nearly singular integrals, an adaptive refinement scheme is implemented. Depending on the distance the element under consideration is partitioned into four smaller elements until the characteristic size of the elements is small enough compared to the distance between the element and the surface point $\mathbf{x}_0$.

The collocation method is applied to create a system of equations that can be solved for the unknown perturbation velocity potential control points, as in Equation 3.8,

$$\mathbf{H}\cdot\boldsymbol{\phi}=\mathbf{G}\cdot\boldsymbol{\sigma} \quad (3.8)$$

where the rows of $\mathbf{H}$ and $\mathbf{G}$ are the $\mathbf{h}$ and $\mathbf{g}$ taken from Equation 3.7. In most of the literature on the application of IGA in BEM formulations, the Greville abscissae are used as collocation points. In previous work of the authors on 2-dimensional aeroelastic analysis using IGA, these points were also used, so this was also the starting point for the present work. The results when using these collocation points show poor convergence at the trailing edge of the wing. The pressure distribution on the top and bottom side of the wing does not converge at a single point, but instead crosses shortly before the trailing edge point and diverges, as is shown in Figure 3.3.

The dynamic Kutta condition, as described in the work of Kim et al. [65], is implemented to reduce this problem. However, to be able to enforce this condition, it

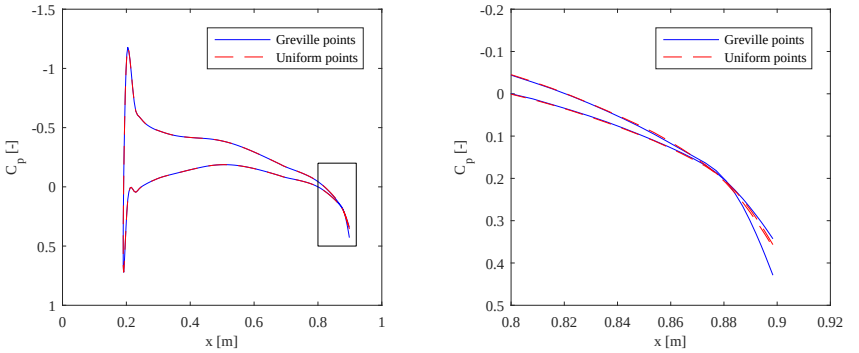

(a) Full pressure distribution **(b)** Trailing edge pressure distribution

Figure 3.3: Pressure distribution of the Onera M6 wing at 33% span using Greville abscissae or uniform points as collocation points

is necessary to solve the system of Equation 3.8 in a constrained least squares way. The overdetermined system is constructed by placing four collocations points uniformly on every element resulting in more collocation points compared to control points. Together with the dynamic Kutta constraint, it shows better convergence of the pressure distribution at the trailing edge. This is shown in Figure 3.3 with the dashed line.

Once the perturbation velocity potential is known, the pressure distribution on the body and the resulting aerodynamic loads can be computed. The loads in the control points are computed by integrating the pressure distribution multiplied by the normal vector and the basis function values over the wing surface area. The induced drag is computed using a Trefftz plane analysis [54]. The intersection of the wake with the Trefftz plane is modelled as a NURBS curve to maintain the exact geometrical concept of the isogeometric principle. The singularity subtraction technique (SST) [66] is used to take care of the hypersingular integrals and the Telles transformation [67, 68] is applied to the nearly singular integrals.

For a multipatch geometry, the system of Equation 3.8 is computed for the entire geometry in one go. At this point, however, measures have to be taken to ensure the proper continuity of the solution. The lowest requirement is to enforce C_0-continuity, so that overlapping control points of the different patches have the same value for the perturbation velocity potential in the final solution. This is done by introducing a transformation matrix that couples these overlapping control points at the edges of neighbouring patches:

$$\mathbf{H} \cdot \mathbf{T}_{C_0} \cdot \boldsymbol{\phi} = \mathbf{G} \cdot \boldsymbol{\sigma} \tag{3.9}$$

In Figure 3.4, the pressure distribution for the Onera M6 wing is shown resulting from the transformation as shown in Equation 3.9. The black lines on the surface

indicate the boundaries of the 39 NURBS patches forming the wing geometry. The relative difference with the unconstrained pressure distribution is also shown. The extreme values are found at the leading edge around the patch interfaces and exceed 100%, illustrating that enforcing C_0-continuity is essential for an accurate solution. The large difference in the leading edge zone can be explained by the strong changes in pressure distribution and the pressure distribution crossing zero in this zone. A small deviation in the location where it crosses zero results in large relative differences.

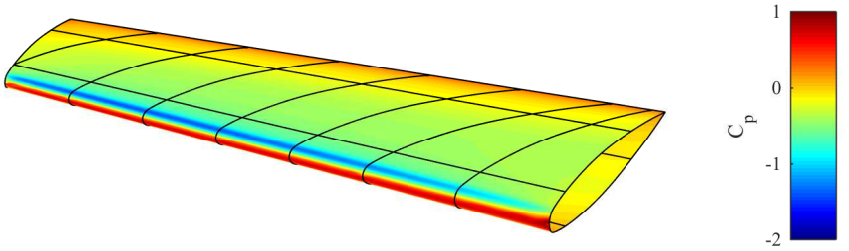

(a) C_0-continuous pressure distribution

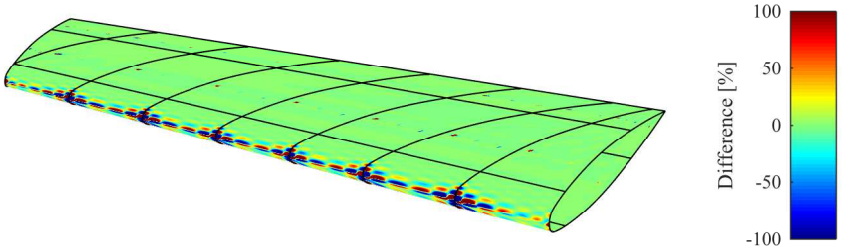

(b) Difference between C_0- and C_{-1}-continuous pressure distribution

Figure 3.4: Comparison of Onera M6 results with C_{-1}- and C_0-continuity for a geometry consisting of 39 NURBS patches

The IGA aerodynamic model is verified by comparing it to the results of the panel code TriPan and the Euler CFD code SUmb [69], as presented in the work of Kennedy and Martins [23]. The pressure distribution of the Onera M6 wing at Mach numbers 0.5 and 0.7 is compared between the three different models at two spanwise locations of the wing. The incoming flow is at an angle of attack of 3.06 degrees. The TriPan results were obtained using 8,000 surface panels, the SUmb results with 3.15 million volume cells including 32,768 surface cells, and the present model uses 39 patches with in total 1,096 cubic surface elements and 2,835 degrees of freedom. The comparison is shown in Figure 3.5. For a Mach number

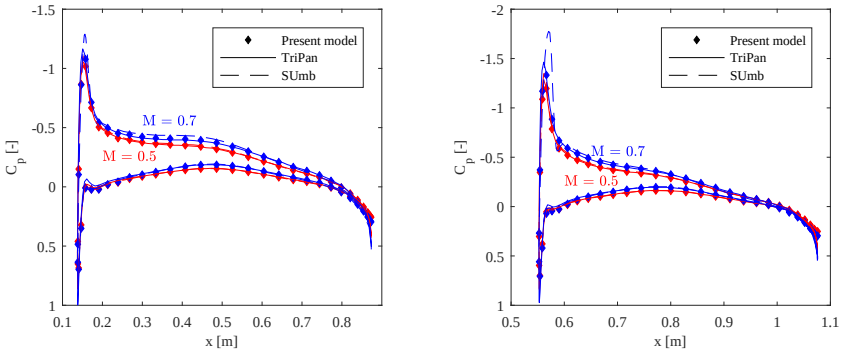

(a) 20% span **(b)** 80% span

Figure 3.5: Comparison of the IGA aerodynamic model with TriPan and SUmb for the Onera M6 wing

of 0.5, the results of the three different models are very similar for both spanwise locations. For Mach 0.7 the results of the present model and TriPan are still close together, but they start to deviate from the results of SUmb especially at the suction peak at the leading edge. This demonstrates that the limit of the potential flow theory including the Prandtl-Glauert correction is indeed somewhere around a Mach number of 0.6 to 0.7. Above this limit, the compressibility effects start to play a significant role in the solution, which the present model is unable to capture.

3.1.3 STRUCTURAL MODEL

Considering the shell-like nature of the aerodynamic model, the natural choice for shell elements for the structural representation was made. In general, the wingbox of an aircraft can be seen as a thin-walled structure. Kirchhoff-Love shell elements would be sufficient to represent such a structure. The use of IGA has opened up the doors to applying the Kirchhoff-Love theory due to the increased order of the basis functions [70]. The absence of rotations in the formulation, calls for C_1 continuity of the displacements. In the interior of a NURBS patch, the functions can be of as high a degree as the user requires. Only on the edges of a patch, the continuity decreases to zero, due to the nature of the open knot vectors that are used. Inside the patch, it is thus no problem to use the Kirchhoff-Love theory. For a multipatch model, however, special care has to be taken at the patch interfaces due to the C_0 continuity at these locations [71].

The alternative is using the Reissner-Mindlin shell theory, which includes the rotations and can also be used for thicker shells. The lower complexity of the multip-

atch implementation of the Reissner-Mindlin theory compared to the Kirchhoff-Love theory has motivated the authors to use this theory for the aeroelastic model presented in this work. A linear shell model based on the work of Dornisch et al. [72, 73] is implemented with the addition of the capability to analyse anisotropic structures as well as isotropic ones. The membrane, bending, and shear stiffnesses of the composite materials are parametrised using lamination parameters [74] for future optimisation purposes. In the following subsection, an overview of the implementation of the anisotropic material in the shell model is given and it is verified.

The stiffness matrix for a Reissner-Mindlin shell made of isotropic material is computed as the volume integral

$$\mathbf{K} = \int_V \mathbf{B}^\top \cdot \mathbf{C} \cdot \mathbf{B} \, \mathrm{d}V \tag{3.10}$$

where the superscript $\top$ indicates the transpose, $\mathbf{C}$ is the material stiffness tensor and $\mathbf{B}$ the matrix describing the relation between the strains and the displacements and rotations. For a derivation of the $\mathbf{B}$ matrix see the work by Dornisch and Klinkel. [72]. Both matrices can be split into components related to the membrane, bending, and shear deformations:

$$\mathbf{K} = \int_V (\mathbf{B}^m)^\top \cdot \mathbf{C}^m \cdot \mathbf{B}^m \, \mathrm{d}V + \int_V \left(\mathbf{B}^b\right)^\top \cdot \mathbf{C}^b \cdot \mathbf{B}^b \, \mathrm{d}V + \int_V (\mathbf{B}^s)^\top \cdot \mathbf{C}^s \cdot \mathbf{B}^s \, \mathrm{d}V \tag{3.11}$$

The superscripts m, b and s indicate the membrane, bending and shear components, respectively.

For an anisotropic material, it is possible that there is a coupling between the different components of the deformation. For example, an in-plane load may introduce not only in-plane stretching, but also out-of-plane bending deformation. The material stiffness tensor, $\tilde{\mathbf{C}}$, for an anisotropic material can be written as

$$\tilde{\mathbf{C}} = \begin{bmatrix} \mathbf{A} & \mathbf{B} & \mathbf{0} \\ \mathbf{B} & \mathbf{D} & \mathbf{0} \\ \mathbf{0} & \mathbf{0} & \mathbf{A}_s \end{bmatrix} \tag{3.12}$$

where the $\mathbf{A}$, $\mathbf{B}$, $\mathbf{D}$ and $\mathbf{A}_s$ matrices are the extensional stiffness, bending-extensional coupling stiffness, bending stiffness, and transverse shearing stiffness, respectively [75]. Stiffened panels are commonly used for aircraft structures. The stiffeners are not explicitly modelled in the present structural model, but their effect is taken into account by computing a so-called smeared panel stiffness that adds the effect of the stiffeners to all four material stiffness matrices [76]. The global structural stiffness matrix can now be computed as follows:

$$\begin{aligned} \mathbf{K} = &\int_V (\mathbf{B}^m)^\top \cdot \mathbf{A} \cdot \mathbf{B}^m \, \mathrm{d}V + \int_V (\mathbf{B}^m)^\top \cdot \mathbf{B} \cdot \mathbf{B}^b \, \mathrm{d}V + \int_V \left(\mathbf{B}^b\right)^\top \cdot \mathbf{B} \cdot \mathbf{B}^m \, \mathrm{d}V \\ &+ \int_V \left(\mathbf{B}^b\right)^\top \cdot \mathbf{D} \cdot \mathbf{B}^b \, \mathrm{d}V + \int_V (\mathbf{B}^s)^\top \cdot \mathbf{A}_s \cdot \mathbf{B}^s \, \mathrm{d}V \end{aligned} \tag{3.13}$$

Once the displacements and rotations of the structural nodes have been determined, the strains in the structure can be computed. The $\mathbf{B}$ matrix is stored at a selection of the integration points and by using Equation 3.14 the strains in these integration points can be computed:

$$\boldsymbol{\epsilon}^i = \begin{bmatrix} \epsilon^i_{11} \\ \epsilon^i_{22} \\ 2\epsilon^i_{12} \\ \kappa^i_{11} \\ \kappa^i_{22} \\ 2\kappa^i_{12} \\ \gamma^i_1 \\ \gamma^i_2 \end{bmatrix} = \mathbf{B}^i \cdot \mathbf{u} \tag{3.14}$$

where $\boldsymbol{\epsilon}$ is a vector with the all the strain components: ϵ_{ij} the membrane strains, κ_{ij} the bending strains, and γ_i the transverse shear strains, and $\mathbf{u}$ is the vector with degrees of freedom. The superscript i indicates the values at integration point i. The strain components are used to compute the engineering strains at the top and bottom of the shells, as the extreme value will be located at either of those. The principal strains at the top and bottom can subsequently be computed by determining the eigenvalues of the infinitesimal strain tensor.

The stresses or strains occurring in the structure can be compared to the material strengths through the available composite strength failure criteria to evaluate whether structural failure occurs or not. However, with a future application in gradient-based structural optimisation in mind, lamination parameters are used for the description of the composite laminates. This means no explicit stacking sequence is available in the analysis and thus the extreme values of the stresses or strains cannot be determined, rendering the strength failure criteria useless in this case. IJsselmuiden et al. [74] derived a failure envelope based on the Tsai-Wu failure criterion which ensures that no failure occurs regardless of the ply angle in the composite laminate. In the present model, the implementation by Khani et al. [77] is used, who reformulated the failure envelope of IJsselmuiden in terms of the principal strains.

The implementation of the anisotropic materials is verified by comparing the results from the present model to those obtained with the commercial finite element analysis (FEA) software Abaqus version 6.13. For the verification, a wingbox for the Onera M6 wing was modelled. It consists of the top and bottom skin panels, a front and rear spar, and eight ribs. All elements have the same thickness of 5 mm. The composite material that is used has the specifications as listed in Table 3.1. For all elements, a symmetric, unbalanced lay-up of [0/45/45/0] was used. The 0 and 90 degree directions are as shown in Figure 3.6 for the first wingbox bay. The remaining bays follow the same definition. A concentrated load of 50 kN

Table 3.1: Material properties (Source: [78])

UD Carbon/Epoxy (AS4/3501-6)	
E_{11}	147.0 GPa
E_{22}	10.3 GPa
G_{12}	7.0 GPa
G_{23}	3.7 GPa
G_{13}	7.0 GPa
ν_{12}	0.27
ρ	1600 kg/m^3

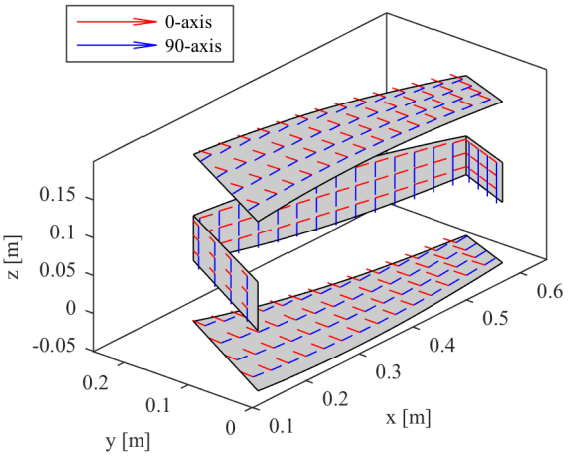

Figure 3.6: 0 and 90 degree axes for the composite lay-up definition for the first wingbox bay

is applied to the tip of the wing at the trailing edge spar, and the wingbox is fully clamped at the root. The Abaqus shell model consists of 12,032 linear S4R elements with a total of 70,800 degrees of freedom, and the IGA model consists of 1,412 cubic elements with a total of 12,994 degrees of freedom. The comparison of the displacement field is shown in Figure 3.7, where the result of the Abaqus model is shown with on top of that the outline of the deformed geometry obtained using the present model. The maximum displacement of the Abaqus model is 0.2508 m and for the IGA model it is 0.2% lower at 0.2503 m. The comparison of the res-

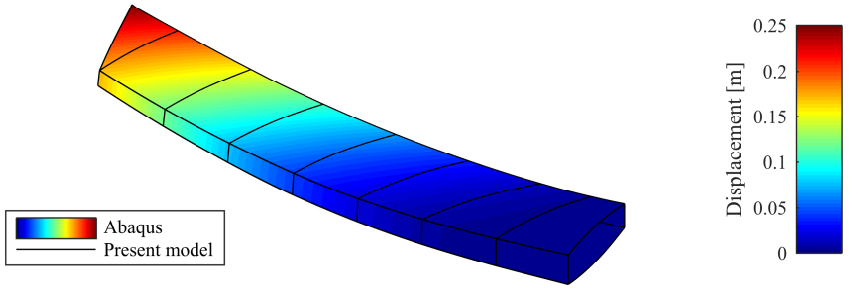

Figure 3.7: Structural displacements of the Onera M6 wingbox under a tip load obtained with Abaqus with an overlay of the outline of the deformed wingbox obtained using the present model

ulting strain field is shown in Figure 3.8. The minimum principal strain of the top outside surface is shown for the two models, which again show a good similarity. The white lines in the results obtained with the present model are caused by the fact that the strains are computed in the integration points, so at the edges of the patches a small gap occurs due to the integrations points being in the interior of the elements. The strains in the rest of the structure, as well as the maximum principal strains, show similar likeness between the models.

3.1.4 AEROELASTIC COUPLING

Coupling the previously described aerodynamic and structural models will enable the simulation of the static aeroelastic behaviour of aircraft wings. In previous work of the authors on two-dimensional isogeometric aeroelastic analysis, it was concluded that the non-interpolatory nature of the NURBS geometry introduces some difficulties in the coupling process.[79] In that work, the gradient matrices that contain the gradients of the control points of the aerodynamic and structural mesh with respect to the control points of the coarse CAD mesh were used to couple the two disciplines. The fact that all three geometries were largely the same, made it relatively easy to use this procedure.

In the present work, the CAD model contains all geometrical features, but the

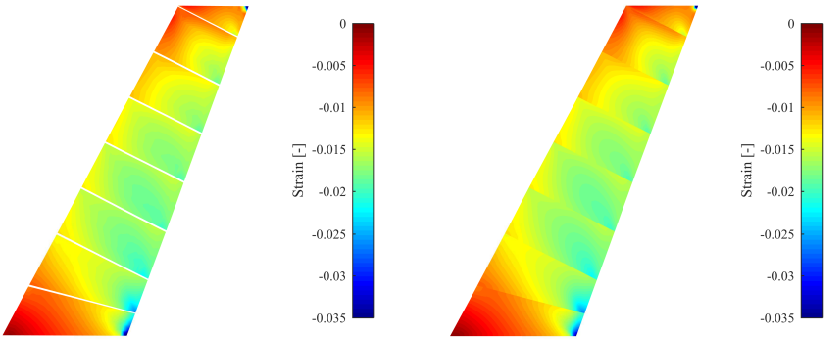

(a) Present model **(b)** Abaqus

Figure 3.8: Minimum principal strain in the top surface of the Onera M6 wingbox obtained using the present model and Abaqus

aerodynamic model consists of only the outer skin of the wing model, and the structural model consists of only the wingbox, as is shown in Figure 3.9. This complicates the coupling using the gradient matrices, as this requires the extrapolation of the displacements of the wingbox to the leading and trailing edge sections of the wing before transferring the displacements to the aerodynamic mesh. Considering the non-interpolatory nature of the NURBS and that the aeroelastic model is meant to be used in a fully free shape optimisation, this is not a trivial task. Furthermore, the structural displacements are mapped onto the coarser CAD mesh before being mapped onto the aerodynamic mesh in the aforementioned method. As a result, the displacement field of the aerodynamic mesh can only be as complex as the CAD mesh allows it to be. This thus increases the requirements of the CAD mesh in terms of the number of control points and degree of the basis functions. These two problems made the gradient matrix method unappealing for the present work, and a different approach was sought for this three-dimensional coupling problem.

Coupling the control points directly is difficult due to them not lying on the surface and thus not being interpolatory. To circumvent this problem, the NURBS geometry of the aerodynamic model is evaluated in the Greville abscissae and the structural model in a user defined selection of points. The Greville abscissae can be also be used for the structural points, but a reduced set of points will lower the computational cost of the RBF interpolation [80] without compromising the accuracy. The Greville abscissae in the parametric space of the NURBS patches can be computed as follows:

$$\bar{\xi}_i = \frac{\xi_{i+1} + \xi_{i+2} + \cdots + \xi_{i+p}}{p}, \qquad i = 1, 2, \ldots, n \tag{3.15}$$

The computed surface points can subsequently be coupled to each other through

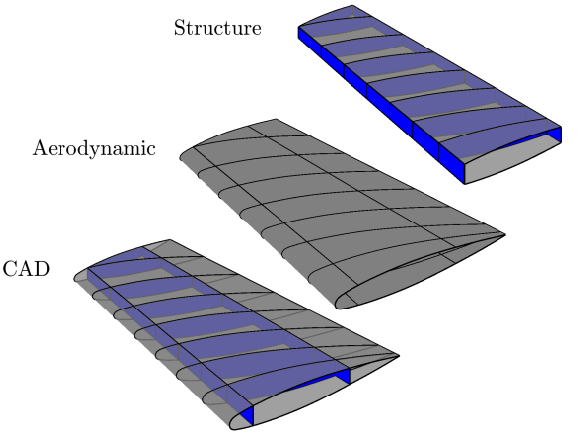

Figure 3.9: The CAD, aerodynamic and structural geometries

RBF interpolation. The basis function values at the surface points are stored in separate matrices, $\mathbf{R}_a$ and $\mathbf{R}_s$, and are used to retrieve the coupling matrix $\tilde{\mathbf{H}}$ that couples the structural (subscript s) and aerodynamic (subscript a) control points:

$$\mathbf{R}_a \cdot \mathbf{P}_a = \mathbf{H} \cdot \mathbf{R}_s \cdot \mathbf{P}_s \tag{3.16}$$

$$\mathbf{P}_a = \tilde{\mathbf{H}} \cdot \mathbf{P}_s \tag{3.17}$$

$$\tilde{\mathbf{H}} = \mathbf{R}_a^{-1} \cdot \mathbf{H} \cdot \mathbf{R}_s \tag{3.18}$$

where $\mathbf{P}_a$ and $\mathbf{P}_s$ are the aerodynamic and structural control points, and $\mathbf{H}$ the coupling matrix for the surface points $\mathbf{x}_a = \mathbf{R}_a \cdot \mathbf{P}_a$ and $\mathbf{x}_s = \mathbf{R}_s \cdot \mathbf{P}_s$. Using the Greville abscissae for the aerodynamic surface points, results in a invertible square matrix $\mathbf{R}_a$ with a good coverage of the complete model. The transformation matrix can now be used to couple the translational structural degrees of freedom to the translations of the aerodynamic control points.

The aerodynamic and structural geometries are split up into two groups for the coupling. The leading and trailing edges of the aerodynamic geometry are coupled to the spars and ribs only. The remaining aerodynamic panels are coupled to the upper and lower skin panels of the wingbox. This is done to avoid problems with local peak loads on the skin of the wingbox. Direct coupling of the full aerodynamic model to the full structural model would result in considerable out-of-plane forces on the wingbox skin panels. The panels would deform excessively, as they are not designed to carry such a load. By coupling the leading and trailing edges to the spars and ribs only, a more realistic load transfer is obtained and the

skin panels carry only the load for which they were designed. The two coupling matrices are in the end assembled into a single matrix.

Once the coupling matrix is determined, the structural displacements can be transferred to the aerodynamic mesh using Equation 3.19:

$$\mathbf{u}^a = \tilde{\mathbf{H}} \cdot \mathbf{u}^s \tag{3.19}$$

where the superscripts a and s indicate whether the variable is defined on the aerodynamic or the structural mesh, respectively. With the transpose of the coupling matrix, the aerodynamic loads can be transferred to the structural mesh:

$$\mathbf{f}_a^s = \tilde{\mathbf{H}}^\top \cdot \mathbf{f}_a^a \tag{3.20}$$

The accuracy of the coupling method is verified through graphical inspection of the aerodynamic and structural meshes and by numerically inspecting the force transfer and resultant forces and moments. In Figure 3.10, both the aerodynamic and structural geometries under aeroelastic deformation are shown on top of each other. The interpolation and transfer of the structural displacements to the aerodynamic mesh give accurate and smooth aerodynamic displacements. The force and moment resultants on both meshes are identical, as is shown in Table 3.2.

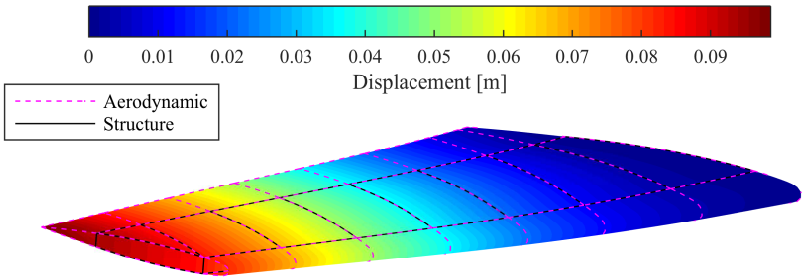

Figure 3.10: The deformed aerodynamic and structural models on top of each other

Table 3.2: Aerodynamic and structural force and moment resultants

	F_x [N]	F_y [N]	F_z [N]	M_x [Nm]	M_y [Nm]	M_z [Nm]
Aerodynamic	-159.93	120.86	2418.2	1269.1	-1126.2	162.99
Structure	-159.93	120.86	2418.2	1269.1	-1126.2	162.99

The coupling matrix $\tilde{\mathbf{H}}$ can now be used to set up the governing equations for the aeroelastic system comprised of the IGA aerodynamic and structural models described before. The first equation is the balance of internal and external loads:

$$\mathbf{f}_{in} - \mathbf{f}_{ext} = \mathbf{f}_s - \mathbf{f}_a - \mathbf{f}_e = \mathbf{0} \tag{3.21}$$

where $\mathbf{f}_s$ are the internal structural loads, $\mathbf{f}_a$ the aerodynamic loads, and $\mathbf{f}_e$ any remaining external loads, such as for instance gravitational loads, fuel loads or

engine thrust. The equation is linearised using a Taylor series expansion to end up at the monolithic governing linear system, which is solved on the structural mesh:

$$\begin{aligned}(\mathbf{K}_s^s - \mathbf{K}_a^s - \mathbf{K}_e^s) \cdot \mathbf{u}^s &= \mathbf{f}_{a,0}^s + \mathbf{f}_{e,0}^s \\ \left(\mathbf{K}_s^s - \tilde{\mathbf{H}}^\top \cdot \mathbf{K}_a^a \cdot \tilde{\mathbf{H}} - \mathbf{K}_e^s\right) \cdot \mathbf{u}^s &= \tilde{\mathbf{H}} \cdot \mathbf{f}_{a,0}^a + \mathbf{f}_{e,0}^s \\ \mathbf{J} \cdot \mathbf{u}^s = \tilde{\mathbf{H}} \cdot \mathbf{f}_{a,0}^a + \mathbf{f}_{e,0}^s &= \mathbf{R}_0 \end{aligned} \tag{3.22}$$

where $\mathbf{K}_s$, $\mathbf{K}_a$ and $\mathbf{K}_e$, are the gradients of the forces with respect to the displacement and thus the structural, aerodynamic and external force stiffness matrices. The subscript 0 refers to the forces as computed for the undeformed initial configuration. The structural stiffness matrix is directly available from the structural model. The aerodynamic and external stiffness matrices are the gradients of the corresponding forces with respect to the structural degrees of freedom and are computed analytically. This monolithic system can be solved in one go to find the aeroelastic solution, whereas a typical staggered approach requires an iterative process to end up in the point of equilibrium. The monolithic approach is thus computationally more efficient and stable.

With Equation 3.22 the aeroelastic deformation can be determined at a constant angle of attack of the wing. To be able to perform aeroelastic analysis in a trimmed configuration, an additional equilibrium equation is required. The trim equation makes sure that the lift is equal to the weight:

$$L - W = 0 \tag{3.23}$$

The same linearisation procedure is followed with the unknown now being the angle of attack α of the wing. Combining the two governing equations results in the complete aeroelastic system:

$$\begin{bmatrix} \mathbf{J} & -\left(\frac{\partial \mathbf{f}_a^s}{\partial \alpha} + \frac{\partial \mathbf{f}_e^s}{\partial \alpha}\right) \\ \frac{\partial L}{\partial \mathbf{u}} & \frac{\partial L}{\partial \alpha} \end{bmatrix} \cdot \begin{bmatrix} \mathbf{u}^s \\ \Delta\alpha \end{bmatrix} = \begin{bmatrix} \mathbf{R}_0 \\ W - L_0 \end{bmatrix} \tag{3.24}$$

Once the aeroelastic deformations and the trimmed angle of attack are determined, the strains can be computed as was already described in subsection 3.1.3, as well as the buckling and boundary layer behaviour as is described in the next subsection.

The aeroelastic analysis is verified by comparing results for the Onera M6 wing with results obtained using SOL 144 in MSC.Nastran version 2014.1. The Onera M6 was originally not designed with an aeroelastic application in mind. The wing is relatively short and stiff and thus shows little aeroelastic coupling. The skin panels can be made thinner to promote aeroelastic deformations. This, however, will at some point result in significant deformations of the airfoil in between the ribs due to the aerodynamic pressures acting on the skin. In the present verification case the material stiffness properties are lowered instead of lowering

the skin thickness to ensure sufficient bending stiffness and consequently avoid too large airfoil deformations.

The isotropic material that is used for the verification has a Young's modulus of 147 MPa and a Poisson's ratio of 0.27. A thickness of 10 mm is used for all skin, spar and rib panels. The Mach number is 0.7, the altitude 35 000 ft, and the angle of attack 3 degrees. The wingbox is modelled in MSC.Nastran using CQUAD4 elements and the aeroelastic coupling is created using the SPLINE4 card with all aerodynamic and all structural nodes included.

The results of the two models are shown in Table 3.3. The tip displacement of the present model is about 6.5% higher compared to that of the MSC.Nastran model. This can be explained by the different aerodynamic models that are used. The MSC.Nastran model uses the doublet lattice model, in which the wing thickness is not modelled and thus not taken into account. This results in a lower aerodynamic lift as is also shown in Table 3.3.

Table 3.3: Aeroelastic results for Onera M6 wing at an equal angle of attack for the present and MSC.Nastran models

	Present model	MSC.Nastran	Difference
Angle of attack [deg]	3	3	0.00%
Rigid lift [N]	1387.7	1313.6	5.64%
Elastic lift [N]	899.6	856.8	5.00%
Tip displacement [m]	0.1494	0.1403	6.49%

To compensate for the lower lift the angle of attack of the MSC.Nastran model is slightly increased, such that the rigid lift of the two models are approximately equal. The results of this updated simulation are shown in Table 3.4 and show that the displacement results are now within 1% of each other.

Table 3.4: Aeroelastic results for Onera M6 wing at an equal rigid lift for the present and MSC.Nastran models

	Present model	MSC.Nastran	Difference
Angle of attack [deg]	3	3.16	-5.06%
Rigid lift [N]	1387.7	1387.9	-0.01%
Elastic lift [N]	899.6	905.2	-0.62%
Tip displacement [m]	0.1494	0.1483	0.74%

3.1.5 Post-processing

The results of the aeroelastic analysis are used to determine whether or not any buckling is occurring in the structure and to compute the viscous drag in the

deformed trimmed configuration in a post-processing step. First, the buckling implementation is described.

Typically, the wingbox inside aircraft wings consists of the top and bottom stiffened skin panels, two or more spars, and a number of ribs. As explained in Subsection 3.1.3, in the present work, the stiffeners on the skin panels are not explicitly modelled. These stiffeners do have a large influence on the buckling behaviour of the wingbox, so for the buckling analysis the user can add stiffeners for buckling purposes only. To reduce the computational cost of the complete model it is also possible to reduce the number of modelled ribs and add ribs for the buckling analysis only.

The curvatures in the wingbox structure are typically low, so they can be modelled as flat plates instead of curved shells to reduce the computational cost. This will result in a conservative approximation of the buckling load. The IGA plate buckling model follows the derivation of Shojaee et al. [81], but with a more general load definition instead of expressing the in-plane loads as a factor times one load value. The Kirchhoff-Love plate model only has the out-of-plane deformations as unknowns, since the buckling panels are modelled as simply supported plates. This choice is made to ensure a conservative approximation of the buckling load by assuming the bending loads of any individual plate cannot be transferred to the surrounding structure.

The eigenvalue problem that has to be solved to find the buckling load is as follows:

$$(\mathbf{K} - \lambda_i \mathbf{K}_g) \cdot \mathbf{w}_i = 0 \tag{3.25}$$

where $\mathbf{K}$ is the global stiffness matrix, $\mathbf{K}_g$ the geometric stiffness matrix, and λ_i and $\mathbf{w}_i$ the i^{th} buckling load and mode shape, respectively. The global stiffness matrix is obtained in a similar way as was done for the Reissner-Mindlin shell model, except that the strain-displacement relation is now different and only the $\mathbf{D}$ material matrix is used for the out-of-plane displacement . The geometric stiffness matrix is obtained as a function of the internal in-plane loads:

$$\mathbf{K}_g^{ij} = \int_V \tilde{\mathbf{B}}_i^\top \cdot \tilde{\mathbf{n}} \cdot \tilde{\mathbf{B}}_j \, \mathrm{d}V \tag{3.26}$$

where $\tilde{\mathbf{n}}$ is the integral through the plate thickness of the in-plane internal stresses and $\tilde{\mathbf{B}}_i$ a vector with shape function derivatives in integration point i:

$$\tilde{\mathbf{B}}_i = \begin{bmatrix} \frac{\partial R_i}{\partial x} \\ \frac{\partial R_i}{\partial y} \end{bmatrix} \tag{3.27}$$

The geometry of the buckling plates is derived from the structural model and the user-supplied information on stiffener and additional rib locations. The corner point of every panel bounded by the stiffeners and ribs are used to find a flat plate through a projection procedure. The in-plane loads in the integration points are determined by projecting the plate integration points onto the shell geometry and

evaluating the loads in those points while taking into account the transformation in coordinate systems.

The other post-processing step is computing the viscous drag. The inviscid potential flow model as described in Subsection 3.1.2 can only provide the induced drag. A higher fidelity model is necessary to obtain the viscous drag component. In the present work, a quasi-3D boundary layer model is implemented based on the previous work from the authors on 2D aeroelastic analysis [79]. Contrary to other literature on this subject, where for the drag analysis separate 2D aerodynamic analyses of the wing sections are done [82, 83, 84], in the present model the 3D flow field computed with the 3D aerodynamic model is directly used as input for the boundary layer analysis. Several sections of the flow field are extracted to obtain the velocity field around the local airfoils. This data is then used in the 2D boundary layer model to approximate the viscous drag.

The 2D sections of the geometry and flow field are determined by finding the intersection between the NURBS geometry and a vertical plane in flow direction at a number of spanwise locations, as is illustrated in Figure 3.11 for a single cutting plane. The intersection is determined by the marching algorithm as described by Hu et al. [85]. Once the local airfoil and tangential velocity field are determined, the boundary layer model, consisting of Thwaites' method for laminar flow, Head's method for turbulent flow, and Michel's method for the transition, is used to compute the growth of the boundary layer from the stagnation point to the trailing edge. The Squire-Young formula is used to predict the viscous drag resulting from the boundary layer.

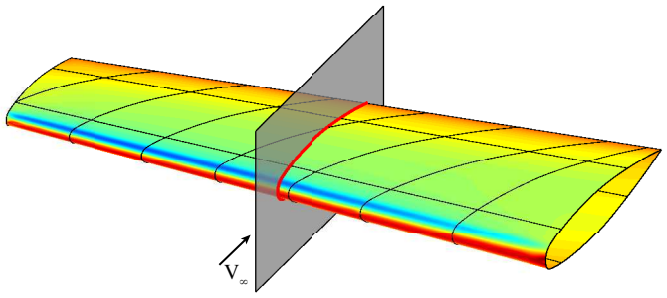

Figure 3.11: Onera M6 geometry with cutting plane and intersection curve

The sectional drag coefficients are used to approximate the drag of the complete wing through a piecewise constant integral over the surface, divided by the planform area:

$$C_{D_v} = \frac{2}{S} \int_0^{b/2} C_{d_v} c \, \mathrm{d}y \tag{3.28}$$

where C_{D_v} and C_{d_v} are the 3D and sectional viscous drag coefficients, S the wing planform area, b the span, and c the chord length.

The drag approximation method is verified by comparing the drag of the Fokker 50 and Fokker 100 wings to reference data taken from the work of Mariens et al. [82] and Elham [83]. In these references, their quasi-3D aerodynamic model is compared to results obtained using the higher-fidelity code MATRICS-V [86], which is based on full potential theory with a 3D integral boundary layer model. This data is used to verify the boundary layer model presented here.

In Figure 3.12, the total drag and its induced and viscous components of the Fokker 50 wing are compared at different lift coefficients. The present model shows a slightly steeper increase of the induced drag and an underestimation of the viscous drag. The movement of the transition lines on the top and bottom of the wing with increasing lift is accurately captured as can be seen by the similarity in the trend of the viscous drag component with respect to the reference data. For the Fokker 100 wing, an underestimation of the drag is observed as well, as is shown in Figure 3.13. The limitation of the potential flow model is also clearly seen in these results, as the increasing wave drag at higher Mach numbers is not taken into account, resulting in a larger deviation with respect to the reference data for increasing Mach number.

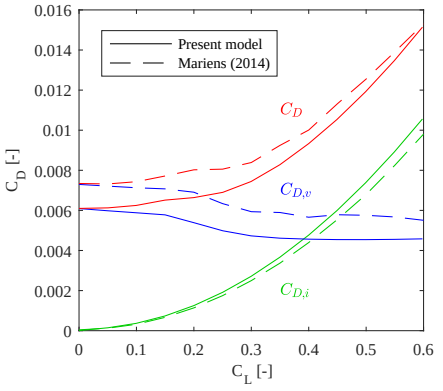

Figure 3.12: Comparison of drag components versus lift for the Fokker 50 wing for the present model and results from Mariens et al. [82]

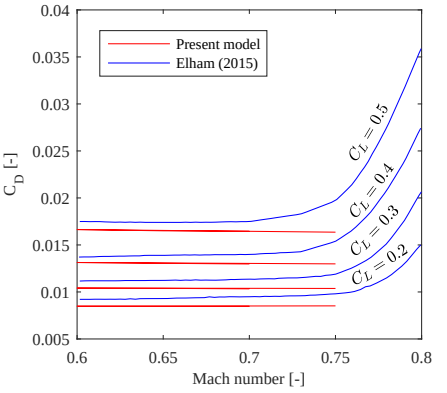

Figure 3.13: Comparison of total drag versus Mach number for the Fokker 100 wing for the present model and results from Elham [83]

The accuracy of the viscous drag estimation is suitable considering the goal and application of the present framework. For the future optimisation purposes, the trends of the viscous drag are more important than the actual values, especially when taking into account the complexity of computing viscous drag for complex geometries. It does, however, need to be taken into account that it is not directly possible to use the drag value in a combined aerostructural objective, as this would result in an unrealistic balance between the two disciplines.

3.2 RESULTS

To demonstrate the unified isogeometric aeroelastic framework as described in the previous sections, the uCRM wing is analysed, and the results are presented in this section. This model is derived from the well-known common research model (CRM) and provides the jig shape that results in the actual CRM outer mold shape in 1g cruise condition, as explained by Kenway et al. [87]. This wing model is thus ideally suited for aeroelastic analysis as it provides the geometry in an unloaded condition. The span of the uCRM measures 58.9 m, the leading edge sweep is 37 degrees, and the wing surface area is 383.7 m^2. The mass of the aircraft excluding the wing and all external masses connected to the wing is 130 202 kg. [88]

3.2.1 MODEL DESCRIPTION

The wingbox presented in the work of Kenway et al. consists of two spars and 48 ribs. In the present work, the layout of the ribs is modified slightly to avoid the rib-rib intersections at the transition from the centre wingbox to the actual wing structure. In the present model a gradual change in the angle of the ribs is implemented instead of the discrete jump, resulting in one less rib in total. This is done because of the requirement in the current framework to have a patch boundary at every connection between skin and internal structure. The rib-rib intersections would require an even higher number of patches, which would increase the computational cost considerably. The CAD model as used in the present work is shown in Figure 3.14.

The structural design of the wingbox used in the present work is based on engineering judgement and are by no means optimised for structural or aerodynamic performance. The goal is to analyse a feasible and realistic design to show the capabilities of the aeroelastic framework. The structural model as described in the remainder of this subsection results in a wingbox with a mass of around 16 000 kg without taking into account stiffener mass. Comparing this value to values found in literature and taking into account it is not optimised, it can be considered to be a realistic value [88, 21].

The stiffener and rib distribution used for the buckling analysis is shown in Figure 3.15. A stiffener pitch of around 25 to 30 cm is used. The stiffeners are placed along the parametric coordinates of the NURBS patches. The ribs are stiffened in both horizontal and vertical direction. The spars are only stiffened in the vertical direction.

The composite material for the skin, spars and ribs is the same as was used in the structural verification and is given in Table 3.1. Additionally, the material strengths, given in Table 3.5, are used for evaluating the failure criterion. The

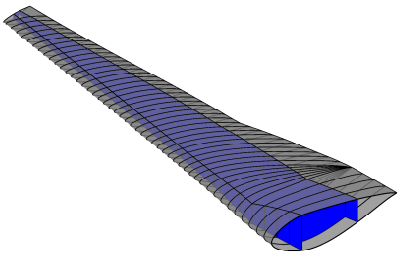

Figure 3.14: Complete CAD model of the uCRM wing with wingbox and aerodynamic surfaces

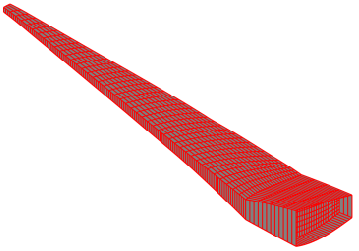

Figure 3.15: uCRM wingbox with stiffener and rib layout for the buckling analysis

Table 3.5: Material strengths (Source: [78])

UD Carbon/Epoxy (AS4/3501-6)	
X_t	948.5 MPa*
X_c	717.6 MPa*
Y_t	23.7 MPa*
Y_c	94.8 MPa*
S	31.6 MPa*

* Including knockdown factors for environmental, barely visible impact damage, and material scatter effects. [89]

directional stiffness distribution on the top skin resulting from the lamination parameters is shown in Figure 3.16, where the rosettes indicate the membrane and bending modulus of elasticity as a function of the polar angle θ as computed using Equations 3.29 and 3.30, respectively, [90]

$$E_{m11}(\theta) = \frac{1}{A_{11}^{-1}(\theta)} \tag{3.29}$$

$$E_{b11}(\theta) = \frac{1}{D_{11}^{-1}(\theta)} \tag{3.30}$$

where

$$\mathbf{A}^{-1}(\theta) = \mathbf{T}^{\top} \cdot \mathbf{A}^{-1} \cdot \mathbf{T} \tag{3.31}$$

$$\mathbf{D}^{-1}(\theta) = \mathbf{T}^{\top} \cdot \mathbf{D}^{-1} \cdot \mathbf{T} \tag{3.32}$$

and

$$\mathbf{T} = \begin{bmatrix} \cos^2(\theta) & \sin^2(\theta) & 2\cos(\theta)\sin(\theta) \\ \sin^2(\theta) & \cos^2(\theta) & -2\cos(\theta)\sin(\theta) \\ -\cos(\theta)\sin(\theta) & \cos(\theta)\sin(\theta) & \cos^2(\theta) - \sin^2(\theta) \end{bmatrix} \tag{3.33}$$

The stiffness is aligned with the swept leading edge and is the same for all the panels shown in Figure 3.16. The bottom skin has the same stiffness characteristics. The ribs and spars are composed of a quasi-isotropic laminate. The thickness of the wingbox panels is shown in Figure 3.17. The bottom skin experiences significantly higher strains compared to the top skin, as will be demonstrated later in this section, and is thus thicker. This is consistent with designs from other literature. [91, 21]

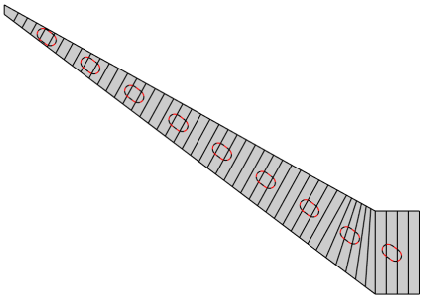

Figure 3.16: Stiffness distribution in top skin panels of the uCRM model

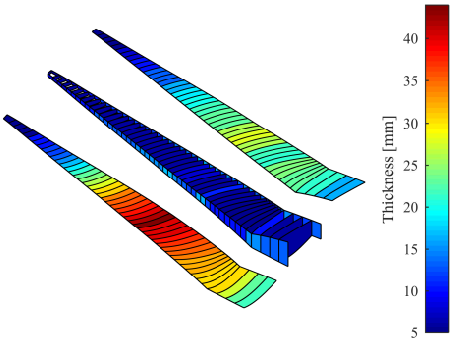

Figure 3.17: Thickness distribution of the uCRM model

The external masses and loads acting on the wing, such as landing gear, fuel and engine, are taken from the work of Werter [92] and are introduced as either

concentrated or distributed loads. An engine thrust of 60 kN is used based on the assumption of a lift-over-drag ratio of the aircraft of around 20.

Three load cases are analysed to demonstrate the computational framework. Firstly, the clamped wing at 1.0 g cruise condition is analysed for aeroelastic deformation and drag. Secondly and thirdly, a 2.5 g symmetric pull-up and a −1.0 g symmetric push-down condition are analysed for structural deformations, strength, and buckling. In general, a cruise Mach number of 0.85 is used for the CRM. In the present model, however, this would be outside of the region of applicability of the potential flow model. For the present work, a cruise Mach number of 0.7 is used instead. This reduced speed will lead to a lower lift generated by the wing, which would result in a relatively high angle of attack in the cruise condition. To compensate for this lower speed, the cruise altitude is lowered from the normally used 37 000 ft to 30 000 ft. The pull-up and push-down load cases are performed at the same Mach number, but at a lower altitude of 10 000 ft. All simulations are performed with a full fuel load.

3.2.2 CRUISE LOAD CASE

In the 1.0 g flight condition, the maximum tip displacement is 1.64 m. It occurs at the trailing edge tip due to the wash-out effect caused by the swept geometry. In the work of Kenway and Martins [21], a tip displacement of approximately 1.52 m was found, which indicates that the structural design used in the present work is indeed reasonable. The complete deformation field is shown in Figure 3.18, together with the deformation fields of the other load cases.

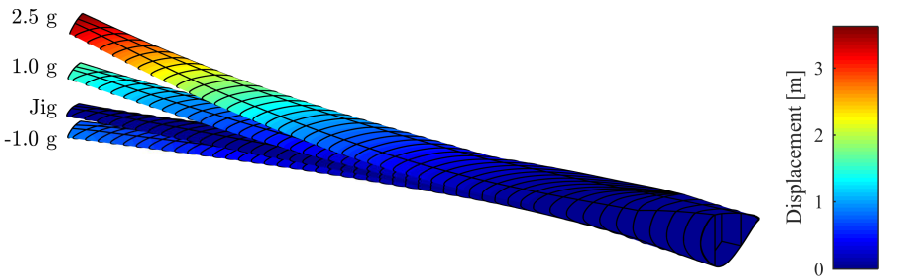

Figure 3.18: Initial and deformed geometry of the uCRM wing under 1.0 g cruise, 2.5 g pull-up, and −1.0 g push-down loading conditions

The be able to estimate the drag of the wing at cruise condition, the aerodynamic analysis is performed on the deformed geometry, as was explained before. The pressure distribution in the deformed configuration is shown in Figure 3.19. The angle of attack for the trimmed cruise flight is 3.5 degrees resulting in a lift coefficient of 0.78. The lift-induced drag is equal to 0.032.

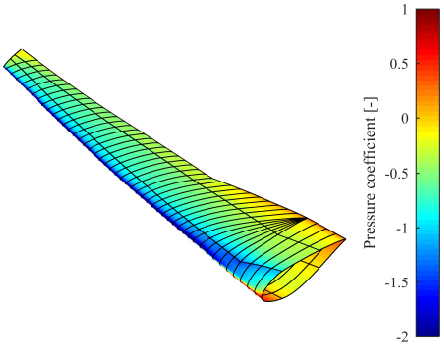

Figure 3.19: Pressure distribution of the uCRM wing at 1.0 g cruise condition

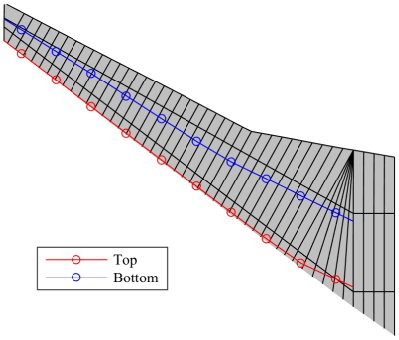

Figure 3.20: Transition lines on the top and bottom side of the uCRM wing at 1.0 g cruise condition

For the quasi-3D viscous drag prediction, the part of the wing that represents the centre wingbox is ignored and only the part that is actually in the airflow is taken into account. This part is sliced at ten uniformly distributed locations to determine the local 2D flow field. The boundary layer model results show that the upper side of the wing is almost fully turbulent, with the transition from the laminar zone in the first 10% of the chord. The lower side of the wing has a larger laminar zone and changes to turbulent at around 55% of the chord. The transition lines for the top and bottom side are shown in Figure 3.20. The resulting viscous drag coefficient is equal to 0.015, bringing the total drag coefficient to 0.047.

3.2.3 Pull-up load case

The maximum tip displacement for the 2.5 g load case is 3.63 m at the trailing edge tip. This is a relatively large displacement compared to the span of the wing, so caution has to be taken with respect to the use of the linear structural model in this case. In future work it would be advisable to switch to a non-linear structural solver. The full displacement is again shown in Figure 3.18.

The values of the Tsai-Wu failure criterion in the wingbox are shown in Figure 3.21a, where a value below 1 means that there is no failure. It can be seen that the bottom wing is most critical, which explains the required higher skin thickness on this side, as was already shown in Figure 3.17. At the intersections of the spars and ribs, local peaks in the strain can be observed. This is caused by the coupling of the leading and trailing edges to the structural members, as was explained before. The loads from these aerodynamic surfaces is fully transferred to the spars and ribs connections, resulting in load concentrations at these points. The

same effect can be seen at the points where the engine and landing gear loads are introduced in the structure. The fuel loads are distributed over the spars, so the effect is smaller there. In most of these peak locations, the Tsai-Wu criterion is higher than 1.0 meaning the current wing design would fail in these locations. A more accurate model of the load introduction and local structural reinforcement would overcome this issue, but this falls outside the scope of the demonstration of the present model.

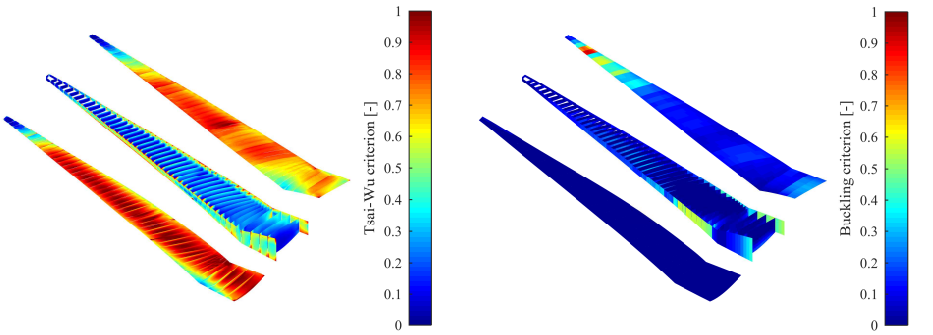

(a) Tsai-Wu criterion **(b)** Buckling criterion

Figure 3.21: Structural results for the uCRM wing under a 2.5 g symmetric pull-up load

The buckling criterion for all the buckling panels in the wingbox are shown in Figure 3.21b, where again a value below 1 means no buckling. The figure shows that only in the top skin towards the wing tip buckling plays a significant role. In the rest of the wingbox, the strength criterion is more important for the present model.

3.2.4 PUSH-DOWN LOAD CASE

The -1.0 g load case induces a displacement field in the opposite direction as the other two load cased, as is shown in Figure 3.18. This results in a downward displacement of -0.78 m at the leading edge tip. From the strength and buckling results in Figures 3.22a and 3.22b, it is clear that this load case is less critical than the 2.5 g load case for the present design. The strain concentrations due to the leading and trailing edge are more clearly visible now, due to the lower level of strain in the rest of the wingbox.

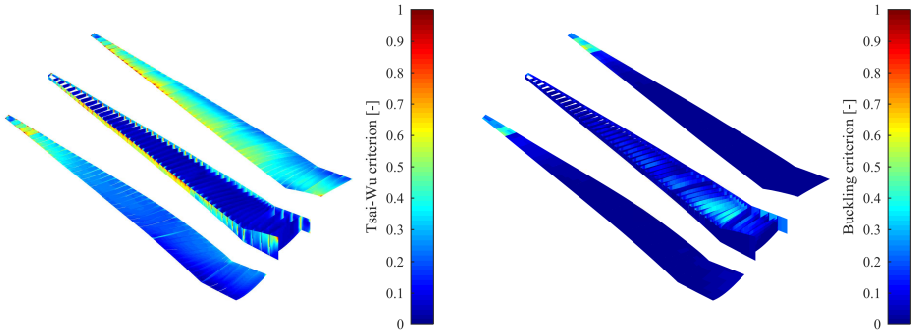

(a) Tsai-Wu criterion **(b)** Buckling criterion

Figure 3.22: Structural results for the uCRM wing under a $-1.0\,\mathrm{g}$ symmetric push-down load

3.3 SYNOPSIS

A computational framework was presented for the aeroelastic analysis of aircraft wings using the isogeometric analysis concept to create a consistent approach for the geometry throughout the analysis. A multi-patch isogeometric aerodynamic potential flow model of the full wing is coupled to a multi-patch isogeometric structural model of the wingbox through a RBF interpolation routine. The structural model supports anisotropic materials, and stiffened panels can be represented through a smeared stiffness approach. In both disciplines, the relevant parts of the same CAD model are used to ensure a consistent geometry throughout the analysis. The resulting aeroelastic deformations are used to compute strains and evaluate the strength criterion. The local buckling behaviour is investigated with an isogeometric plate buckling model, and the viscous drag is estimated using a quasi-3D boundary layer model that uses the 3D flow field from the potential flow model as input.

The separate parts of the framework were verified against reference solutions. The aerodynamic verification demonstrated that using the Greville abscissae as collocation points results in unfavourable convergence of the pressure distribution at the trailing edge. Using uniformly distributed collocation points in combination with a dynamic Kutta condition improves the convergence. The implementation of a C_0 transformation matrix for the multi-patch models further improves the quality of the solution.

The coupling of the aerodynamic and structural model is done through a RBF interpolation routine where the Greville abscissae are used to evaluate a set of points on both geometries to be able to achieve the interpolation. The coupling

matrix is then projected back onto the control points to be able to use it for setting up the aeroelastic system. The coupling is done for two separate sets of points to ensure a realistic transfer of the aerodynamic loads onto the wingbox.

Viscous drag is estimated in a post-processing step where the 3D flow field resulting from the potential flow model is used as input for a quasi-3D boundary layer model, instead of performing complete 2D airfoil analyses. The drag estimation compares well to existing literature in terms of trends, but underestimates the viscous drag by approximately 10%. This is deemed satisfactory when taking into account the scope and future application of the present computational framework.

The complete framework was demonstrated by performing an aeroelastic analysis of the uCRM wing for three different load cases. The cruise load case was used to demonstrate the aeroelastic analysis in combination with the drag estimation method. The 2.5 g symmetric pull-up and −1.0 g symmetric push-down manoeuvre load cases showed the material failure and the plate buckling analyses. Selected results were compared to results from literature and similar values were observed, confirming the capabilities of the present framework.

4

TOWARDS THREE-DIMENSIONAL ISOGEOMETRIC AEROSTRUCTURAL OPTIMISATION

The isogeometric aeroelastic analysis framework presented in the previous chapter was developed with the aim of aerostructural optimisation in mind. The analysis framework allows for a geometrically consistent formulation of the optimisation problem. Throughout the main part of the process, (parts of) the same exact CAD geometry are used, removing any costly mesh generation steps and avoiding the introduction of geometrical errors. Furthermore, the CAD geometry provides a natural environment for shape optimisation through the control points of the NURBS functions. In the present analysis model, approximate geometries are used only in the post-processing steps to reduce computational cost and complexity in these steps.

This chapter describes the initial steps towards the goal of geometrically consistent aerostructural optimisation of conventional and non-conventional aircraft wings. The optimisation formulations is presented in Section 4.1, including the objective function, constraints and design variables. Subsequently, the sensitivity analysis is described and verified. A design case example is presented in Section 4.3. Section 4.4 covers the remaining challenges that were identified in initial aerodynamic shape optimisation attempts.

4.1 OPTIMISATION FORMULATION

The goal of aerostructural optimisation in this research is to simultaneously find the best aerodynamic shape and structural stiffness and thickness to maximise the total performance of an aircraft wing. In traditional aircraft wing design, these two disciplines are kept separate. The aerodynamic shape is optimised for aerodynamic performance in the form of drag minimisation, and the structure is optimised for minimum weight.

A simple example, however, demonstrates that the total performance of a wing requires a trade-off between the two disciplines. The Breguet range equation, given in Equation 4.1, shows that both aerodynamic lift and drag and structural weight influence the range an aircraft can fly. A multi-disciplinary approach is thus crucial when striving for maximum performance in wing design.

$$R = \frac{V_\infty}{g} \frac{1}{C_T} \frac{C_L}{C_D} \ln\left(\frac{W_{initial}}{W_{final}}\right) \tag{4.1}$$

In the following subsections, the objective function, constraints and design variables that are used in such an aerostructural optimisation are described.

4.1.1 OBJECTIVE FUNCTION

The objective function for aerostructural optimisation is more complex compared to the traditional objective functions used in sequential design. If a single discipline is optimised, the absolute value of the objective function is not of critical importance, as the aim is to minimise it irrespective of the actual value. Once two or more disciplines are included in an objective function, such as in the Breguet range equation, it is essential that the parameters in the objective function represent the actual values, as trade-offs have to be made during the optimisation. Without accurate values, the balance between the different disciplines is incorrect, and thus an incorrect trade-off will be made by the optimiser.

In the present aeroelastic analysis model, the lift and drag of only the wing are computed. As a result, it would be incorrect to use this in the objective function directly, since that involves the complete aircraft. The empirical models as described in the work by Kenway and Martins [21] are used to estimate the drag introduced by the rest of the aircraft. Together with the wing drag, this gives an estimation of the drag of the full aircraft.

The aircraft wing mass is formed by the primary structural wingbox mass, computed from the structural model, and the secondary mass of the components attached to the leading and trailing edge of the wingbox, which is related to the wing surface [23]:

$$M_{wing} = 1.5 M_{wing}^{primary} + 15 S_{wing} \tag{4.2}$$

where the factor 1.5 takes into account any detail ignored in the wingbox model. Together with fixed design masses for the rest of the aircraft components, the full aircraft mass is estimated.

With these estimations of the full aircraft lift, drag and mass, an actual multi-disciplinary objective function such as the Breguet range equation, or equations derived from it, can be used in the aerostructural optimisation.

4.1.2 CONSTRAINTS

The constraint used in the optimisation can be divided into two groups. The first group are the geometrical constraints and the second group are the structural constraints. The geometrical constraints are aimed at making sure the optimised geometry satisfies some basic geometrical requirements. The following constraints are included in the framework:

- Lower limit on the volume per wingbox bay
- Upper limit on the wing span
- Lower limit on the wing area

The first constraint is to ensure enough space is available for fuel storage in the wings. The other constraints are there to avoid the optimiser to move to too extreme regions of the design space.

The second group consists of structural constraints and include the following:

- Feasibility constraints for lamination parameters
- Tsai-Wu failure constraints
- Buckling failure constraints

In the current work, eight lamination parameters are used to describe an unbalanced, symmetric laminate. Before a design can be realised, these lamination parameters have to be translated to a manufacturable composite layup. The feasibility constraints make sure the lamination parameters form a set of which the stiffness characteristics can actually be approximated by a physical layup.

A total of six feasibility constraints are used per set of lamination parameters. Two of these describe the relation between the in-plane lamination parameters and two the relation between the out-of-plane parameters. The remaining two equations provide a coupling between the in- and out-of-plane parameters [92].

The Tsai-Wu failure constraints are implemented to avoid any material failure in the structural wingbox. As explained in Subsection 3.1.3, the constraint is based on the principal strains instead of the more traditional formulation based on the stresses due to the use of lamination parameters. The principal strains are computed in every structural integration point. For a cubic NURBS discretisation, this results in 16 evaluation points per isogeometric element. The strains are expected to be highest at corner points of the elements, so only the four points closest to the corners are taken into account in the constraints. In order to further reduce the number of constraints, it is possible to select the n most critical points per patch in the initial design.

The buckling failure constraints originate from the panel buckling model, described in Subsection 3.1.5. For every buckling panel, the n most critical modes in the initial design are taken into account. Taking only the single most critical mode into account would result in incorrect gradient information in the case of mode switching. By taking a big enough selection of critical modes, the chance is high that any mode that would be critical throughout the optimisation is included in the set.

4.1.3 DESIGN VARIABLES

The design variables can be divided into the same two groups as was done for the constraints: geometrical and structural. The geometrical, or shape, design variables govern the aerodynamic shape of the wing. These are the control points of the NURBS patches making up de wing geometry.

Every patch, however, is a self-containing piece of the geometry, so without proper measures, the optimiser could basically disassemble the complete geometry into an unconnected set of patches. At every patch-patch interface, rules have to be implemented to tell the optimiser what is allowed at that interface. In the present framework, three options are available:

- C_{-1} connection: All interface control points of the two patches are free to move.
- C_0 connection: The patches have to remain connected, but a kink is allowed.
- G_1 connection: The patches have to remain connected in a smooth way without a kink in between the patches.

The consequences for the control points on the connected patches are obvious in the first two cases: In the first case all control points are free to move as illustrated in Figure 4.1b, and in the second case the overlapping control points on the interface have to remain overlapped as illustrated in Figure 4.1c. The smooth

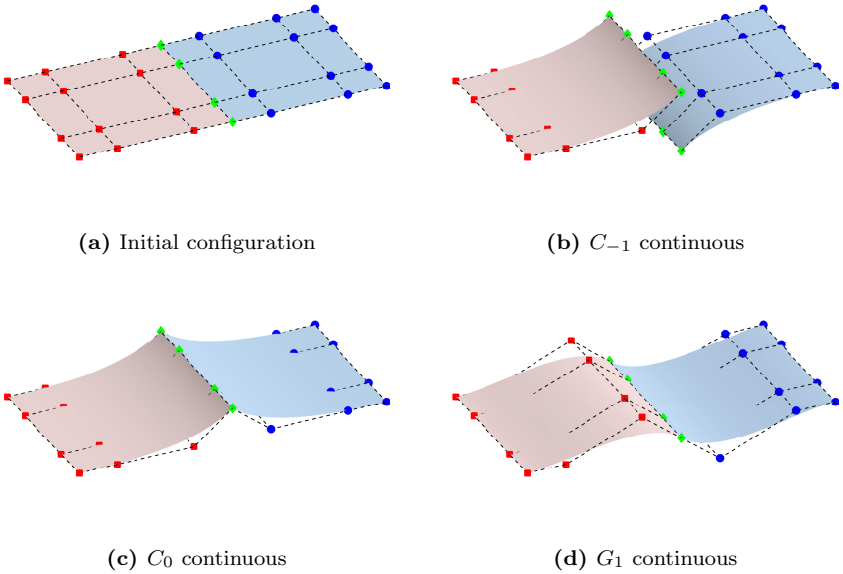

(a) Initial configuration

(b) C_{-1} continuous

(c) C_0 continuous

(d) G_1 continuous

Figure 4.1: Different options for patch connectivity. Blue and red indicate the two connected patches and the green markers the overlapping control points.

connection is achieved when the control points before and after the interface and the overlapping ones are on one line, as illustrated in Figure 4.1d.

This connectivity information can be used to reduce the number of design variables, as the value of the control points on the connecting, or slave, patch can be derived from the control points on the master patch. A transformation matrix is set up to enable the transfer between the reduced set of control points to the full set so that the shape perturbations originating from the optimiser can be introduced into the geometrical patches.

The structural design variables consist of lamination parameters and thicknesses. The lamination parameters consist of eight variables per laminate: four in-plane parameters and four out-of-plane variables. This set of parameters can represent unbalanced, symmetric layups. The possibility of having unbalanced laminates is included because these are essential for aeroelastic tailoring through laminate extension-shear coupling. The structural design variables are currently implemented per patch.

The possibility of assigning structural design variables to every control point is also implemented, which would allow the optimisation of the local layup. By using the same NURBS discretisation as in the CAD model, a smooth variation of the lamination parameters and thickness can be obtained. Proper restrictions on the

rate of change of the variables are required to ensure a design that can actually be manufactured [93]. The NURBS discretisation can provide the possibility of computing gradients of the variables due to its higher continuity.

4.1.4 OPTIMISER

The number of design variables for a typical aerostructural design case using the presented framework has an order of magnitude of a thousand, making using anything but gradient-based optimisation intractable. The built-in fmincon function in Matlab is used with its interior-point algorithm and user-supplied gradients.

4.2 SENSITIVITIES

As mentioned before, a gradient-based optimiser is used, meaning the gradients, or sensitivities, of the objective and constraints with respect to the design variables need to be computed. The sensitivities are computed analytically, as the number of design variables and computational cost of the framework prohibit simpler methods like finite differencing. The direct method, in contrast to the adjoint method, is used to compute all the sensitivities throughout all the models. The order of magnitude of the number of design variables and constraints is roughly equal, so implementing the adjoint in the current framework would not result in a significant reduction of the computational effort.

As explained in Subsection 3.1.4, the monolithic aeroelastic system can be written as in Equation 3.24. The sensitivities of the aeroelastic displacements and trim correction of the angle of attack can be computed by taking the derivative of this equation:

$$\frac{\mathrm{d}}{\mathrm{d}x}\begin{bmatrix}\mathbf{J}-\left(\frac{\partial \mathbf{f}_a^s}{\partial \alpha}+\frac{\partial \mathbf{f}_e^s}{\partial \alpha}\right)\\ \frac{\partial L}{\partial \mathbf{u}}\frac{\partial L}{\partial \alpha}\end{bmatrix}\cdot\begin{bmatrix}\mathbf{u}^s\\ \Delta\alpha\end{bmatrix} + \begin{bmatrix}\mathbf{J}-\left(\frac{\partial \mathbf{f}_a^s}{\partial \alpha}+\frac{\partial \mathbf{f}_e^s}{\partial \alpha}\right)\\ \frac{\partial L}{\partial \mathbf{u}}\frac{\partial L}{\partial \alpha}\end{bmatrix}\cdot\begin{bmatrix}\frac{\mathrm{d}\mathbf{u}^s}{\mathrm{d}x}\\ \frac{\mathrm{d}\Delta\alpha}{\mathrm{d}x}\end{bmatrix} = \frac{\mathrm{d}}{\mathrm{d}x}\begin{bmatrix}\mathbf{R}_0\\ W-L_0\end{bmatrix} \tag{4.3}$$

where x is a design variable.

Replacing the matrix with the symbol $\tilde{\mathbf{J}}$ and rearranging to solve for the required gradients gives the following equation for the sensitivities of the aeroelastic solution with respect the a design variable:

$$\begin{bmatrix}\frac{\mathrm{d}\mathbf{u}^s}{\mathrm{d}x}\\ \frac{\mathrm{d}\Delta\alpha}{\mathrm{d}x}\end{bmatrix} = \tilde{\mathbf{J}}^{-1}\cdot\left(\frac{\mathrm{d}}{\mathrm{d}x}\begin{bmatrix}\mathbf{R}_0\\ W-L_0\end{bmatrix} - \frac{\mathrm{d}\tilde{\mathbf{J}}}{\mathrm{d}x}\cdot\begin{bmatrix}\mathbf{u}^s\\ \Delta\alpha\end{bmatrix}\right) \tag{4.4}$$

The second term in the parenthesis involves the derivative of the aerodynamic stiffness matrix, which is part of $\mathbf{J}$ as was explained in Subsection 3.1.4. The aerodynamic stiffness matrix, being the first derivative of the aerodynamic forces with respect to the aeroelastic degrees of freedom, is computationally expensive to obtain. For shape optimisation, Equation 4.4 shows that also the second derivative would be required, which is prohibitively expensive to compute in the current framework.

One way around this problem is to use the governing Equations 3.21 and 3.23 to determine the sensitivities instead of the monolithic aeroelastic system. The approach, explained in detail by Martins and Hwang [94], is based on computing the derivatives in the point of equilibrium where it is known that the gradient of the governing equation is zero. This simplifies the computation. In the presented framework, however, only a single Newton iteration is done to find the aeroelastic solution and as such, the computation is not done in, or very close to, the point of equilibrium. Using this approach in the current framework thus only gives the approximate sensitivities, as is also explained in the early work of Grossman [6].

More concretely, it means that the variation of the matrix $\tilde{\mathbf{J}}$ multiplied by the aeroelastic solution is not taken into account when following this approach. To improve the accuracy of the sensitivities, the variation of the structural stiffness matrix is computed in the present framework and is included in the computation of the aeroelastic sensitivities, so at least part of the variation of $\tilde{\mathbf{J}}$ is taken into account.

In the remainder of this section, the analytical sensitivities are verified through comparison with finite difference results. A random perturbation in the design variables is applied and the combined induced change in objective and constraint equations is compared to the change predicted by the analytical sensitivities multiplied by the design variable perturbations.

First, the effect of the aforementioned approximation of the aeroelastic sensitivities is investigated. In Figure 4.2, the errors of the finite difference sensitivities with respect to the analytical ones are shown for the objective function and the first 10 Tsai-Wu and buckling failure constraints. This selection of the constraints is done for clarity of the figures. The remaining sensitivities show the same behaviour. These results are obtained while keeping the components that are ignored in the approximation constant. The analysis thus corresponds with the sensitivity computation in this case. The plots indeed show accurate convergence of the finite difference sensitivities to the analytical results for reducing step sizes. A step size of 10^{-4} or smaller makes the difference indistinguishable.

In Figure 4.3, the results are shown when all the variations in $\tilde{\mathbf{J}}$ are included in the analysis and the sensitivities are thus approximate. The finite difference results for the objective function sensitivities still closely converge to the analytical results. The results for the constraints, however, show that there is a difference of about

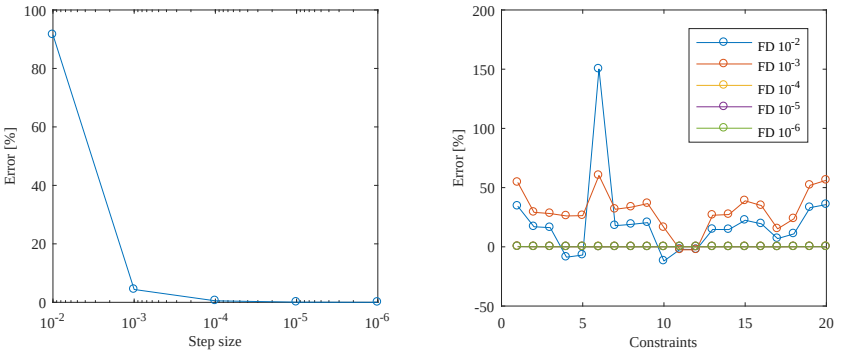

(a) Objective function **(b)** Constraints

Figure 4.2: Comparison of analytical and finite difference shape sensitivities for consistent analysis and sensitivity computation

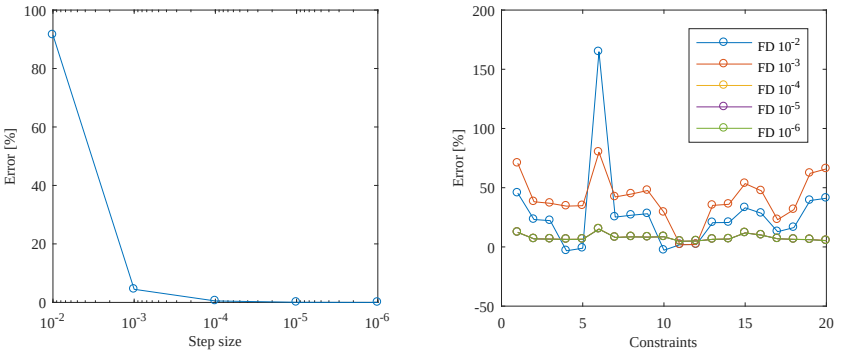

(a) Objective function **(b)** Constraints

Figure 4.3: Comparison of analytical and finite difference shape sensitivities for approximate sensitivity computation

10% between the analytical and finite difference results. The approximation of the sensitivities thus gives reasonable results in this case.

The sensitivities with respect to the structural design variables are also verified. The effect of the approximation is not found in the results of the lamination parameters as these structural design variables do not cause any variation in $\tilde{\mathbf{J}}$ outside the structural stiffness matrix. The variation in the structural stiffness matrix is taken into account, so the sensitivities should indeed still be exact. The results for the in-plane and out-of-plane variables are shown in Figures 4.4 and 4.5, respectively. In the objective function results, it can be seen that at smaller finite difference steps, the results diverge again. The change in drag values is so low at these perturbation levels that numerical noise starts playing a role in the finite difference results.

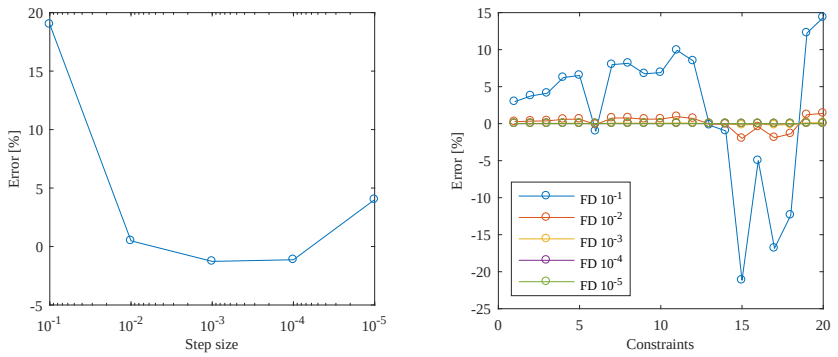

(a) Objective function **(b)** Constraints

Figure 4.4: Comparison of analytical and finite difference in-plane lamination parameter sensitivities for approximate sensitivity computation

The thickness variables do cause some variation in some of the terms of $\tilde{\mathbf{J}}$ as they influence the weight of the wing. The effect, however, is negligible in this case, as is shown in Figure 4.6. Both the objective and constraints converge to the analytical results.

4.3 Design case

The aerostructural optimisation framework is tested through the application to the design of a high-subsonic aircraft wing for an aircraft with a maximum take-off weight (MTOW) of 100 000 kg. The initial design is a simple rectangular wing with a constant symmetrical airfoil throughout the semi-span of 20 m. The untapered wing has a chord of 5 m and has no sweep. A neutral starting geometry

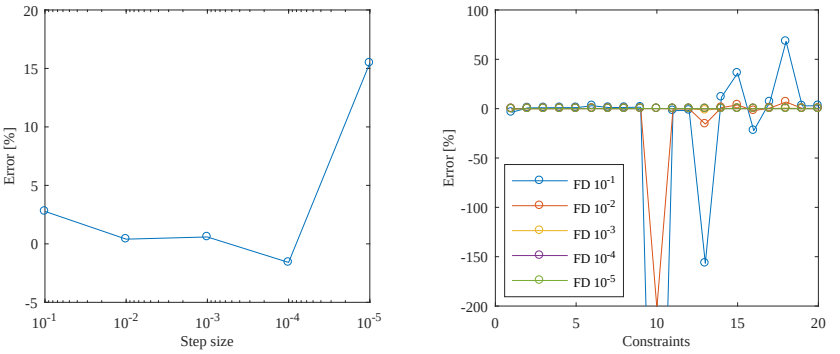

(a) Objective function **(b)** Constraints

Figure 4.5: Comparison of analytical and finite difference out-of-plane lamination parameter sensitivities for approximate sensitivity computation

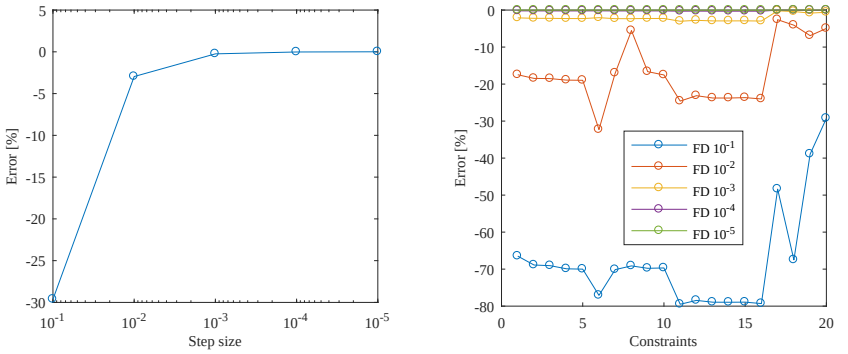

(a) Objective function **(b)** Constraints

Figure 4.6: Comparison of analytical and finite difference thickness sensitivities for approximate sensitivity computation

(no sweep, no taper, etc.) was chosen so that no bias towards a certain solution is included in the initial design.

The optimisation model is shown in Figure 4.7, where Figure 4.7a shows the patches making up the geometry and Figure 4.7b shows the control net taking into account the continuity requirements. The model consists of 10 spanwise sections, each composed of 8 patches totalling 80 patches for the complete model. The patches representing the skin of the wing are all bi-cubic, and the internal patches are cubic in the direction they are connected to the skin to ensure matching discretisations. In the vertical direction, these patches are linear to reduce the number of control points and to ensure that the spars and ribs remain flat.

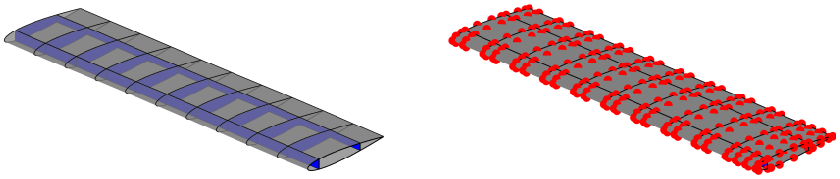

(a) Patches **(b)** Control net

Figure 4.7: Optimisation geometry showing the patch discretisation and control net

The implementation of the continuity requirements of the geometry can be seen in the absence of certain rows of control points. The values of these control points are computed from the other points to enforce C_1-continuity and as such are not included in the set of design variables.

The aerodynamic and structural meshes derived from the optimisation geometry are shown in Figure 4.8. The aerodynamic mesh consists of only the outer skin of the wing and the structural mesh of only the wingbox patches. The patches originating from the optimisation geometry are refined to ensure converged analytical results. The aerodynamic mesh consists of 50 patches and 2580 control points. The structural mesh is also built up out of 50 patches and consists of 3240 control points. The wingbox is constructed out of a front and rear spar and 10 ribs closed off by the upper and lower skin panels.

Before the full aerostructural optimisation, the aerodynamic shape was attempted to be optimised separately to gain trust and experience with the optimisation framework. The initial results showed several shortcomings in the current implementation that call for modifications to the framework. The remaining challenges towards the complete aerostructural optimisation capabilities are demonstrated and explained in the next section.

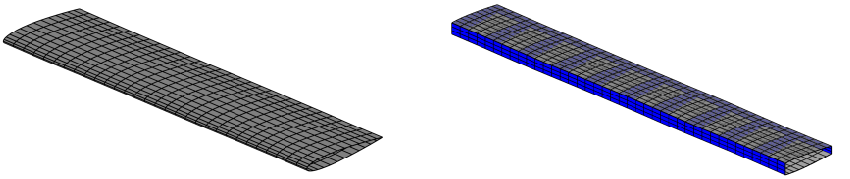

(a) Aerodynamic mesh **(b)** Structural mesh

Figure 4.8: Aerodynamic and structural optimisation meshes

4.4 CHALLENGES

The shape optimisation is performed using only the optimisation geometry and aerodynamic mesh. The control net, as depicted in Figure 4.7b, is used as design variables. The two main problem areas that are identified in the results are maintaining the mesh quality and the continuity of the boundary layer formulation. Additionally, the computational efficiency of the current framework is too low for direct use in a preliminary design phase of large complex wings. The following subsections will elaborate on these challenges, and potential solutions are proposed that can (partially) resolve these shortcomings.

4.4.1 MESH QUALITY

The shape optimisation is purely based on the modification of the NURBS control points. No global parameters as span, sweep or taper are included to reduce the restrictions placed on the possible optimised designs. Avoiding these global variables allows designs that deviate from the well-known solutions that are parametrised by these variables. This does, however, make maintaining a quality mesh throughout the optimisation more challenging. The geometry can change in many different ways, which could lead to unfavourable solutions, either because of reduced accuracy in the analysis due to severe mesh deformations or due to physically infeasible results.

The sensitivity analysis of the aerodynamic performance parameters with respect to the shape design variables revealed shortcomings in the current framework that result in these mesh quality issues. In Figure 4.9a, the sensitivities of the control points near the tip of the wing are shown. The high value at the trailing edge tip causes severe local deformations of the geometry, as illustrated in Figure 4.9b. Not only is this physically unfavourable, it also has a significant impact on the accuracy of the analysis as the deformation grows. The most likely cause of this

local spike in sensitivity is the requirement of the inclusion of a discretised wake in the potential flow model. The dimensions of the wake in the current aerodynamic model depend on the trailing edge points only. As the drag is computed using a Trefftz plane analysis, the dimensions of the wake have a direct influence on the lift-induced drag. This single point will thus have a strong influence on the induced drag, as is seen in Figure 4.9a.

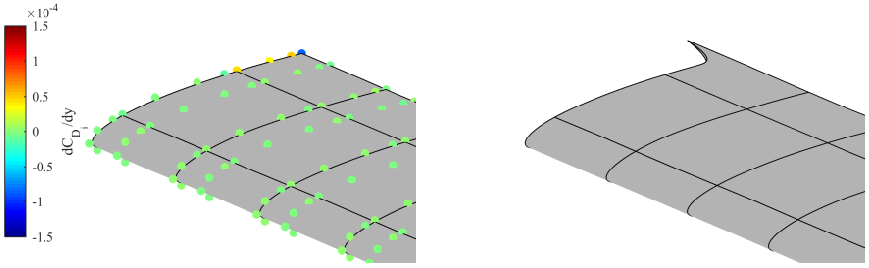

(a) Sensitivities **(b)** Deformation

Figure 4.9: Shape sensitivities of the induced drag with respect to the y coordinate at the wing tip and illustration of the resulting shape deformation

To smoothen the effect of this single point, the y-coordinate of the control points at the tip of the wing can be parametrised with a single design variable. This resolves the problem of the physically infeasible local deformation at the trailing edge tip, as is illustrated in Figure 4.10. The issue with the mesh deformation, however, is reduced but still present. The outer control points are moved in order to increase the span, but the rest of the control points remain stationary, as is shown in the same figure. As a result, the isogeometric elements near the tip become severely stretched (Figure 4.10b), and computational accuracy is reduced.

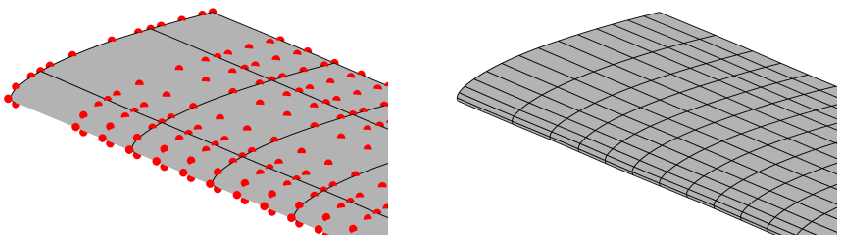

(a) Optimisation control points **(b)** Aerodynamic mesh

Figure 4.10: Illustration of the tip shape deformation with a single design variable for all tip y-coordinates showing the deformation of the optimisation control points and aerodynamic mesh

Two challenges can be identified from these results. The first challenge is that large local peaks in the sensitivities should be avoided, as these will force the optimiser into an infeasible direction. Although the resulting geometry is still smooth due to the use of NURBS functions, the deformations are too local and as such the optimised design will not be feasible in a real-life application. The second challenge is to maintain a high enough mesh quality throughout the optimisation. Control points should move in-plane to ensure a regular mesh, even though it may not result in actual modifications of the shape.

These challenges are similar to those encountered in node-based shape optimisation. Mesh regularisation and filtering techniques have been developed in this field to provide a solution to these challenges. For example, the vertex morphing method presented by Hojjat et al. [95] provides a synchronous approach to tackle both problems. Considering that in the optimisation framework presented in this dissertation the boundary between CAD and FEM has been removed, it can be interpreted as both CAD-based and node-based optimisation. As such, the vertex morphing method could provide a means to reduce the aforementioned issues of mesh quality and sharp sensitivity distributions in the framework presented here. The method has also been demonstrated for the node-based shape optimisation of a forward-swept wing, where it was demonstrated that the method allows the exploration of true design alternatives, contrary to the more traditional experience-based parametrisation [96].

The sensitivities of the induced drag with respect to the x-coordinates at the complete trailing edge section of the wing, shown in Figure 4.11a, exhibit a pattern where high values can be found on the patch boundaries, while very low values are found in between. This can be explained by the way the continuity of the patch connections is implemented. For G_1-continuity, the control point on the boundary and the two neighbouring ones should be on the same line. As a result, when one of the neighbouring control points is moved over a distance X in x-direction, the other neighbouring control points will move over a distance $-X$ in x-direction. The result is that these two deformations cancel each other.

The induced drag becomes smaller as the aspect ratio of the wing increases. As the two effects cancel each other, the resulting change in aspect ratio is small, and thus the sensitivity is very low. The control points on the patch boundaries do have a direct effect on the aspect ratio and as such have a higher sensitivity. The resulting deformation, however, is unfavourable as the movement of these control points automatically induces a wavy pattern in the trailing edge, as is illustrated in Figure 4.11b.

The most obvious solution for this problem would be to modify the CAD discretisation and avoid the use of G_1 connections. The current framework, however, can only work with conforming meshes between the different patches, so at every rib and spar interface a patch boundary should be present in the skin. If non-conforming meshes would be allowed, the problem could be reduced. A single

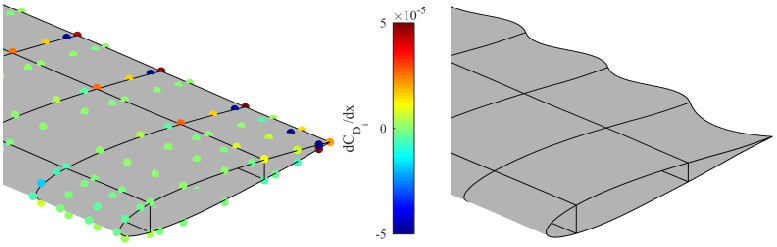

(a) Sensitivities **(b)** Deformation

Figure 4.11: Illustration of the tip shape deformation with a single design variable for all tip y-coordinates showing the deformation of the optimisation control points and aerodynamic mesh

patch throughout the span could be used instead of separate patches between the ribs and spars, removing the G_1 connections. Non-conforming multi-patch isogeometric implementations have been demonstrated using different methods. For example, Nguyen et al. [97] demonstrated an approach based on Nitsche's method, Dornisch et al. [98] applied the mortar method for coupling the patches, and Coox et al. [99] focussed on a master-slave technique that is both simple in implementation and use, and robust and flexible.

For more complex geometries it might not be possible to avoid the use of multiple patches over the span of the wing. The work of Kiendl et al. [100] identified a similar problem of strong influence of the geometry discretisation in the shape optimisation of shells. Along lines of C_0-continuity, they enforced the C_1-continuity in the same fashion as is done in this dissertation, which resulted in an increased geometrical influence of these points. They developed a sensitivity weighting method that spreads out the influence again, such that the shape optimisation follows a more physical path and wavy results, such as those shown in Figure 4.11b, can be avoided.

4.4.2 Boundary layer behaviour

As was already mentioned in Chapter 2, the optimisation framework has the tendency to get stuck in local optima due to the boundary layer model. In the two-dimensional work, this was countered by implementing a two-step optimisation approach. For the three-dimensional work, the issue becomes more apparent as now not one, but multiple sectional boundary layer analyses are combined to estimate the viscous drag, as explained in Subsection 3.1.5. Every one of these analyses could run into a situation where from one iteration to the next, a jump in the transition point or separation can occur. These discontinuous phenomena cause large inaccuracies in the sensitivity information and as such pose a challenge

for the optimisation algorithm.

Removing these discontinuities is challenging as the physical behaviour of the boundary layer can be seen as discontinuous. A possibility would be to use a fully turbulent boundary layer formulation instead of the current laminar/turbulent implementation. This will result in a conservative estimation of the drag, as a turbulent boundary layer generates more drag, but as there is no transition point any more, there will not be any jumps either. Additionally, it could be interesting to take into account the friction coefficient in the boundary layer. When it is zero, it means the flow has separated. This information can be used to create a continuous constraint that prevents separation over the complete section. Enforcing this on every point on the wing sections would result in a large number of additional constraints. Combining it with a constraint aggregation technique could overcome this, if necessary.

The current boundary layer implementation seems more suitable for a refining optimisation of an already globally optimised wing design instead of an optimisation starting from a very general wing shape. The chance of ending up in some local minimum that stops the optimisation before reaching the kind of designs that are sought after is currently too big. Another option to reduce the issues with the boundary layer would be to implement a multi-step optimisation formulation, as was demonstrated in Chapter 2. In that case, the boundary layer model was not included in the first step, where only the lift was maximised. This enabled the optimisation of the airfoil to a much greater extent compared to the single-step optimisation. In the second step, the boundary layer model was included through the drag coefficient, and the airfoil resulting from the first step was further refined.

A more general approach could be formulated by using a lower-fidelity drag estimation model in the first optimisation step. A semi-empirical model, such as the one used by Kenway and Martins [21], provides a much more robust estimation where phenomena like transition and separation of the flow are not taken into account. Implementing such a model would allow for a global optimisation of the wing shape. In the second optimisation step, the model as described in Subsection 3.1.5 could be used to further refine the design while taking into account the more complex flow phenomena.

4.4.3 COMPUTATIONAL EFFICIENCY

The final main challenge in the presented aerostructural optimisation framework is the computational efficiency. The computational cost of the current implementation is relatively high when considering its targeted application in a preliminary design phase. Despite parallelisation of large parts of the analysis models, an analysis run with sensitivity analysis of a design case such as presented in this chapter takes around 3 hours on a system with two Intel Xeon E5-2640 v4 pro-

cessors with a total of 20 cores and 128 GB of RAM. A run without sensitivity analysis takes about 40 minutes on the same system.

The main part of this computational cost originates from the aerodynamic model. The use of higher-order basis functions prohibits the use of analytical integrals for the aerodynamic influence coefficients. Numerical quadrature has to be used to compute the influence of every element on every collocation points, rapidly increasing the computational cost as the number of degrees of freedom increases. Additionally, this process results in fully populated matrices in the governing equation, making it expensive to solve this equation for the unknown flow variables. The gradients of these matrices are also required for creating the aerodynamic system and for the sensitivity analysis, which results in very high memory usage to store all this data.

The memory requirements have been reduced by avoiding the storage of the full gradient data of the aerodynamic influence matrices. Instead, the gradient data is computed in blocks, and the gradients of the flow variables are computed per block and only this information is stored.

A more substantial saving can be achieved by implementing the fast multipole method in the aerodynamic boundary element model. The method, regarded as one of the top 10 algorithms in scientific computing developed in the twentieth century [101], decreases the quadratic scaling of the computational time with the number of degrees of freedom in the conventional BEM to a linear scaling. Additionally, the aerodynamic influence coefficient will no longer be fully populated, potentially resulting in a significant decrease in memory usage in the gradient computation. [102]

Implementation of the fast multipole method in an isogeometric application has been demonstrated by Takahashi and Matsumoto [42] for two-dimensional potential problems governed by the Laplace equation. A decrease from quadratic to linear scaling of the computational time with respect to the number of degrees of freedom was indeed achieved. Simpson and Liu presented the implementation of a black-box multipole method to overcome the complexity of implementing the fast multipole method to an existing BEM model, again demonstrating the same reduction in scaling of computational time with the number of degrees of freedom.

4.5 Synopsis

An aerostructural optimisation framework for the preliminary design of non-conventional aircraft wings was presented. The formulation of the optimisation problem was described, including objective function, constraints and design variables. The sensitivity analysis required for the gradient-based optimisation was described, with extra focus on the approximate solution for the gradients of the

state variables of the aeroelastic system. The analytical design sensitivities were verified through comparison with finite difference results.

An aerostructural design case was presented. Initial shape optimisation results revealed several challenges still remaining before the fully free aerostructural optimisation can be attempted. The three main challenges were found to be the regulation of the mesh quality and sensitivity smoothness, the boundary layer behaviour and the computational efficiency of the framework. The shortcomings in the current implementation were identified and potential solutions were proposed.

5

CONCLUSIONS AND RECOMMENDATIONS

In the introduction of this dissertation, the basis of this research was formulated in the form of the following main research goal:

> *Develop a preliminary wing design framework for geometrically consistent aerostructural analysis and optimisation that enables the design of non-conventional wing configurations.*

Through further investigation of the state-of-the-art this goal was translated to a more concrete set of two sub-goals:

- Develop low-fidelity static aeroelastic analysis capabilities that are fully based on the isogeometric analysis (IGA) concept.
- Fit the aeroelastic analysis model in a geometrically consistent aerostructural optimisation routine that provides a high level of design freedom for exploring new wing configurations.

In this final chapter, the conclusions drawn throughout this dissertation are summarised, and the goals are reflected back upon in order to evaluate the successfulness of the research to achieve these goals. Subsequently, although already partly covered in Chapter 4, recommendations for future research are given.

5.1 CONCLUSIONS

Two low-fidelity computational frameworks for isogeometric aeroelastic analysis were presented that rely on the use of non-uniform rational b-splines (NURBS) basis functions to represent both the geometry and the unknown fields. The first framework was formulated in two-dimensional space and focuses on the aeroelastic analysis of airfoils.

The aerodynamic model is a multi-patch isogeometric potential flow boundary element method (BEM) model. A desingularised formulation is used to enable easy and accurate calculation of the singular contributions present in a boundary element model. The Greville abscissae are used as collocation points, and verification with numerical and experimental results showed the accurate performance of the model. A multi-patch curved Timoshenko beam model was implemented for the structural analysis. The model is formulated in the global reference frame instead of the conventional local reference frame to enable easy coupling with the aerodynamic model. A master-slave technique is used to couple the structural patches, allowing both rigid and hinged connections. Comparison with analytical solutions verified the accuracy of the model.

The aerodynamic and structural model are both derived from a shared computer-aided design (CAD) model. The gradient information computed analytically in these steps is used for the formulation of a novel coupling method. The gradient matrices containing the gradients of the aerodynamic and structural control points with respect to the CAD control points are used to couple the two models to each other and form a monolithic aeroelastic model. A semi-empirical boundary layer model is implemented for the computation of the viscous drag that is neglected by the potential flow model.

For the second computational framework the same concept was used, but now for three-dimensional aeroelastic analysis. An isogeometric potential flow model taken from literature was further extended to be able to deal with more complex geometries, and the Prandtl-Glauert transformation was included to allow more accurate simulations at high-subsonic Mach numbers. The structural model is based on a linear isogeometric Reissner-Mindlin shell model from literature, extended to include the analysis of anisotropic materials and lamination parameters. Both three-dimensional models were verified against reference numerical results.

A further development of the conventional radial-basis function (RBF) interpolation was presented to enable the coupling of the aerodynamic and structural models. Different parts of the shared CAD geometry are used in the two disciplines, calling for a different coupling method as was used in the two-dimensional situation. RBF interpolation was made possible by evaluating the Greville abscissae on the aerodynamic and structural models. These surface points are used to create the coupling matrix, which subsequently is projected back onto the control

points through the matrices containing the basis function values of the Greville abscissae points.

The boundary layer model from the two-dimensional work was used to create a quasi-three-dimensional model for the viscous drag estimation. Sections of the three-dimensional solution are analysed and integrated to find the drag. An isogeometric panel buckling model was implemented to analyse the local buckling behaviour of the wing.

The three-dimensional analysis framework was demonstrated through the simulation of a wing model based on the undeflected common research model (uCRM) wing. The wing was analysed at three different flight conditions and the aeroelastic deformations, deformed aerodynamics, material failure and buckling failure results were presented and discussed. The aeroelastic results compared well with results found in the literature.

Both aeroelastic analysis frameworks rely on the isogeometric concept and as such the first sub-goal has been achieved successfully. The models are geometrically consistent through the use of the CAD geometry for both the aerodynamic and structural disciplines. Only in the post-processing steps, the isogeometric concept is not always adhered to. This to allow for the use of existing simpler models. The frameworks have been demonstrated to produce accurate aeroelastic results.

Achieving the second sub-goal required the implementation of the aeroelastic analysis frameworks into an optimisation formulation. The two-dimensional version was applied to the optimisation of an active morphing airfoil. At this stage, no full aerostructural optimisation was performed to reduce the complexity of the optimisation. The goal of the optimisation was to improve the landing conditions of a unmanned aerial vehicle (UAV) through morphing of the trailing edge section of the airfoil. The actuation was provided by three vertically placed actuators. Only structural and morphing design variables were included.

A single step optimisation procedure was compared to an improved two-step procedure. The first one quickly ended up in local minima due to the boundary layer model. The two-step procedure avoided this problem by first optimising the lift coefficient without taking into account the viscous drag and in the second step refining the design by including it again. The two-step approach was used to optimise the airfoil design using different sets of design variables. As the number of design variables increased, the increase in lift also grew due to the increased design freedom. The optimisation result with all design variables included showed an increase in lift coefficient of 42%. The absence of flow separation was confirmed through a simulation in Xfoil.

The three-dimensional aerostructural optimisation formulation was presented, describing the objective, constraints and design variables. The analytical sensitivity analysis was described and the resulting gradients compared well to finite difference results. A design case for the fully free aerostructural optimisation was

described in the form of a relatively simple rectangular wing model that would allow geometrically unbiased optimisation.

Initial shape optimisation attempts identified three main challenges that require additional work before the aerostructural optimisation can be performed. The current implementation shows large peaks in shape sensitivity values resulting in large local deformations of the geometry. Additionally, the mesh deformations are very local deteriorating the quality of the mesh and reducing the quality of the analysis results. A potential improvement was proposed in the form of mesh regularisation and filtering techniques as encountered in node-based shape optimisation.

Additional challenges were found in the boundary layer behaviour. The problem, already encountered in the two-dimensional optimisations, originates from the discontinuous nature of the boundary layer model. Modification of the laminar/turbulent formulation to a fully turbulent one and implementation of a continuous constraint on the flow separations were proposed as an improvement. A multi-level approach such as used in the two-dimensional work was also described as a possible solution.

Finally, the computational cost of especially the aerodynamic boundary element method was identified as too high for preliminary design. The fast multipole method was proposed as a possible solution to reduce the computational time and memory usage.

In conclusion, the second sub-goal has not been realised completely in the presented work. The geometrical consistency was achieved through the use of the CAD geometry for all the relevant parts of the analysis and optimisation. The challenge, however, is to create a framework that allows a high level of design freedom. This requires a very robust framework that can deal with large deformations while maintaining accuracy. Furthermore, the framework should deliver a smooth objective function and constraints that allow optimisation over a big range of the design space. Only then will it be possible to achieve the fully free aerostructural optimisation that was envisioned for this research project. The improvements that were proposed based on the initial optimisation results provide the next steps towards such a framework.

5.2 RECOMMENDATIONS FOR FUTURE WORK

The main recommendations for improving the presented three-dimensional aerostructural optimisation framework were already proposed in Chapter 4 and were summarised in the previous section. The recommendations in this section are based on the assumption that these ideas have been implemented into the framework and the fully free aerostructural optimisation can be performed successfully.

The first step should be to compare the geometrically consistent optimisation framework to the traditional methods. This comparison will reveal whether the anticipated benefits of the implementation of the isogeometric analysis concept and uniform use of the CAD geometry are indeed realised in the form of increased accuracy and ability to more easily explore non-conventional layouts.

The constraints that are currently implemented in the framework are concerned with structural and aerodynamic limitations only. Including constraints for the combined field of aeroelasticity will further improve the quality of the optimisation results. The static aeroelastic model could be used to compute, for example, the divergence speed and control effectiveness. Especially when exploring non-conventional wing designs, it will be important to take into account such constraints, as these can make or break a design.

Continuing along these lines, dynamic aeroelastic effects like flutter or gust responses could be taken into account if the computational models are extended to their dynamic versions. The trend of more slender and flexible wings increases the coupling between aerodynamics and structures, so these phenomena become more and more important in the early design stages. The dynamic framework also allows the evaluation of more load cases besides the standard static ones covered in this dissertation. The more flexible wings of course also exhibit larger displacements, which could go outside the linear regime of the structural model. Extension to a non-linear shell model will enhance the analysis capabilities.

The potential flow theory used for the aerodynamic analysis limits the validity of the analysis to high subsonic speeds, despite the implementation of the Prandtl-Glauert correction. Most modern-day transport aircraft tend to fly at transonic speeds, making the current framework unreliable for the optimisation of such aircraft. Changing the complete aerodynamic to, for example, an Euler model would deteriorate the low-fidelity nature of the framework and would drive up the computational cost. Furthermore, it would destroy the natural combination of CAD, BEM, and shell finite element method (FEM) through the isogeometric analysis concept, as volume meshes would be required for such a model. The defect-correction approach as presented by Dillinger [90] could be a viable method to include the transonic effects in the current framework while maintaining its low-fidelity nature.

As was already shortly mentioned in Chapter 4, the NURBS discretisation could provide an interesting basis for the implementation of fibre steering for the composite laminates. Assigning the lamination parameters to the control points will guarantee a smooth and continuous variation of the parameters and as such smooth variation of the fibre angles in the laminates. The continuity of the variables over the wing surface can be used to place constraints on the rate of change of the lamination parameters, which could perhaps serve as manufacturing constraints to avoid large discrepancies between the structural performance before and after translation to physical layups. In any case, the lamination parameters

resulting from the optimisation will need to be translated to physical laminates, so a multi-step conversion method as, for example, described by Peeters [93] would have to be implemented.

Finally, the current clamped wing model is a simplification of the reality where the wing interacts with all the other parts of the aircraft, such as the fuselage, tail and engines. A first step would be to take into account the aerodynamic effects of these other components in order to increase the accuracy of the aerodynamic loads. The next step would be to also take the structural side into account and model a fully elastic aircraft. This would allow a better simulation of the aeroelastic behaviour of the full system. The current strategy, where the same CAD model is used for aerodynamics and structures, will still be applicable in this situation, although it might be worth considering changing from NURBS to more flexible basis functions, such as T-splines, for modelling these more complex geometries.

A

CONTROL-POINTS FOR NACA2412 AIRFOIL

Table A.1: Part 1 of the coarse mesh control points and weights for the NACA2412 airfoil

x [m]	y [m]	weight
0.6	0	1
0.596	-0.0003	1
0.5878	-0.0009	1
0.5738	-0.002	1
0.5564	-0.0033	1
0.5346	-0.0049	1
0.5088	-0.0067	1
0.4793	-0.0088	1
0.4467	-0.011	1
0.4115	-0.0133	1
0.3743	-0.0157	1
0.3358	-0.0181	1
0.2967	-0.0203	1
0.2575	-0.0222	1
0.2189	-0.0236	1
0.1817	-0.0248	1
0.1465	-0.0255	1
0.1138	-0.0254	1
0.0842	-0.0245	1
0.0583	-0.0226	1
0.0367	-0.0197	1
0.0197	-0.0157	1
0.0081	-0.0109	1
0.0015	-0.0053	1
-0.0003	0	1

Table A.2: Part 2 of the coarse mesh control points and weights for the NACA2412 airfoil

x [m]	y [m]	weight
0.0005	0.0056	1
0.006	0.0124	1
0.0167	0.0193	1
0.033	0.0263	1
0.0542	0.0327	1
0.0799	0.0382	1
0.1096	0.0427	1
0.1426	0.0458	1
0.1784	0.0475	1
0.2161	0.0477	1
0.2552	0.0463	1
0.295	0.0439	1
0.3346	0.0406	1
0.3736	0.0367	1
0.4111	0.0322	1
0.4465	0.0273	1
0.4793	0.0224	1
0.5089	0.0175	1
0.5348	0.0129	1
0.5566	0.0088	1
0.5739	0.0054	1
0.5879	0.0026	1
0.5961	0.0008	1
0.6	0	1

BIBLIOGRAPHY

[1] Airbus, Global market forecast 2017-2036: Growing horizons, ISBN: 978-2-9554382-2-6 (2017).

[2] European Commission, Flightpath 2050: Europe's vision for aviation, EUR 098 EN (2011).

[3] B. Grossman, Z. Gürdal, R. T. Haftka, G. J. Strauch, W. M. Eppard, Integrated aerodynamic/structural design of a sailplane wing, Journal of Aircraft 25 (9) (1988) 855–860. doi:10.2514/3.45670.

[4] S. Wakayama, I. Kroo, Subsonic wing design using multidisciplinary optimization, in: 5th Symposium on Multidisciplinary Analysis and Optimization, American Institute of Aeronautics and Astronautics, 1994, pp. 1358–1368. doi:10.2514/6.1994-4409.

[5] S. Wakayama, I. Kroo, Subsonic wing planform design using multidisciplinary optimization, Journal of Aircraft 32 (4) (1995) 746–753. doi:10.2514/3.46786.

[6] B. Grossman, R. T. Haftka, J. Sobieszczanski-Sobieski, P.-J. Kao, D. M. Polen, M. Rais-Rohani, Integrated aerodynamic-structural design of a transport wing, Journal of Aircraft 27 (12) (1990) 1050–1056. doi:10.2514/3.45980.

[7] J. W. Gallman, S. C. Smith, I. M. Kroo, Optimization of joined-wing aircraft, Journal of Aircraft 30 (6) (1993) 897–905. doi:10.2514/3.46432.

[8] A. Chattopadhyay, N. Pagaldipti, A multidisciplinary optimization using semi-analytical sensitivity analysis procedure and multilevel decomposition, Computers & Mathematics with Applications 29 (7) (1995) 55–66. doi:10.1016/0898-1221(95)00018-T.

[9] M. Baker, J. Giesing, A practical approach to MDO and its application to an HSCT aircraft, in: 1st AIAA Aircraft Engineering, Technology, and Operations Congress, American Institute of Aeronautics and Astronautics, 1995. doi:10.2514/6.1995-3885.

[10] A. A. Giunta, V. Balabanov, D. Haim, B. Grossman, W. H. Mason, L. T. Watson, R. T. Haftka, Multidisciplinary optimization of a supersonic transport using design of experiments theory and response surface modeling, Tech. rep., Virginia Polytechnic Institute & State University, Blacksburg, VA, USA (1997).

[11] K. Maute, M. Nikbay, C. Farhat, Coupled analytical sensitivity analysis and optimization of three-dimensional nonlinear aeroelastic systems, AIAA Journal 39 (11) (2001) 2051–2061. doi:10.2514/2.1227.

[12] J. Reuther, J. Alonso, J. Martins, S. Smith, A coupled aero-structural optimization method for complete aircraft configurations, in: 37th Aerospace Sciences Meeting and Exhibit, American Institute of Aeronautics and Astronautics, 1999. doi:10.2514/6.1999-187.

[13] J. Martins, J. Alonso, J. Reuther, Aero-Structural Wing Design Optimization Using High-Fidelity Sensitivity Analysis, in: Proceedings of the CEAS Conference on Multidisciplinary Aircraft Design and Optimization, 2001.

[14] K. Maute, M. Nikbay, C. Farhat, Sensitivity analysis and design optimization of three-dimensional non-linear aeroelastic systems by the adjoint method, International Journal for Numerical Methods in Engineering 56 (2003) 911–933. doi:10.1002/nme.599.

[15] P. Piperni, M. Abdo, F. Kafyeke, A. T. Isikveren, Preliminary Aerostructural Optimization of a Large Business Jet, Journal of Aircraft 44 (5) (2007) 1422–1438. doi:10.2514/1.26989.

[16] P. Piperni, A. DeBlois, R. Henderson, Development of a Multilevel Multidisciplinary-Optimization Capability for an Industrial Environment, AIAA Journal 51 (10) (2013) 2335–2352. doi:10.2514/1.J052180.

[17] A. Gazaix, P. Gendre, E. Chaput, C. Blondeau, G. Carrier, P. Schmollgruber, J. Brezillon, T. Kier, Investigation of multi-disciplinary optimisation for aircraft preliminary design, in: SAE Technical Papers, 2011. doi:10.4271/2011-01-2761.

[18] I. Ghazlane, G. Carrier, A. Dumont, J. A. Désidéri, Aerostructural Adjoint Method for Flexible Wing Optimization, in: 53rd AIAA/ASME/ASCE/AHS/ASC Structures, Structural Dynamics and Materials Conference 2012, 2012. doi:10.2514/6.2012-1924.

[19] I. Salah El Din, A. Dumont, C. Blondeau, Transonic wing-body civil transport aircraft aero-structural design optimization using a bi-level high fidelity approach - A focus on the aerodynamic process, in: 51st AIAA Aerospace Sciences Meeting including the New Horizons Forum and Aerospace Exposition, American Institute of Aeronautics and Astronautics, 2013. doi:10.2514/6.2013-144.

[20] G. K. W. Kenway, G. J. Kennedy, J. R. R. A. Martins, Scalable parallel approach for high-fidelity steady-state aeroelastic analysis and adjoint derivative computations, AIAA Journal 52 (5) (2014) 935–951. doi:10.2514/1.J052255.

[21] G. K. W. Kenway, J. R. R. A. Martins, Multipoint high-fidelity aerostructural optimization of a transport aircraft configuration, Journal of Aircraft 51 (1) (2014) 144–160. doi:10.2514/1.C032150.

[22] Z. J. Zhang, S. Khosravi, D. W. Zingg, High-fidelity aerostructural optimization with integrated geometry parameterization and mesh movement, Structural and Multidisciplinary Optimization 55 (4) (2017) 1217–1235. doi:10.1007/s00158-016-1562-7.

[23] G. J. Kennedy, J. R. R. A. Martins, A parallel aerostructural optimization framework for aircraft design studies, Structural and Multidisciplinary Optimization 50 (6) (2014) 1079–1101. doi:10.1007/s00158-014-1108-9.

[24] A. Elham, M. J. L. van Tooren, Coupled adjoint aerostructural wing optimization using quasi-three-dimensional aerodynamic analysis, Structural and Multidisciplinary Optimization 54 (4) (2016) 889–906. doi:10.1007/s00158-016-1447-9.

[25] T. J. R. Hughes, J. A. Cottrell, Y. Bazilevs, Isogeometric analysis: CAD, finite elements, NURBS, exact geometry and mesh refinement, Computer Methods in Applied Mechanics and Engineering 194 (39-41) (2005) 4135–4195. doi:10.1016/j.cma.2004.10.008.

[26] J. A. Cottrell, T. J. R. Hughes, Y. Bazilevs, Isogeometric analysis: Toward integration of CAD and FEA, John Wiley & Sons, 2009.

[27] Y. Bazilevs, M.-C. Hsu, I. Akkerman, S. Wright, K. Takizawa, B. Henicke, T. Spielman, T. E. Tezduyar, 3D simulation of wind turbine rotors at full scale. Part I: Geometry modeling and aerodynamics, International Journal for Numerical Methods in Fluids 65 (1-3) (2011) 207–235. doi:10.1002/fld.2400.

[28] Y. Bazilevs, M.-C. Hsu, J. Kiendl, R. Wüchner, K.-U. Bletzinger, 3D simulation of wind turbine rotors at full scale. Part II: Fluid-structure interaction modeling with composite blades, International Journal for Numerical Methods in Fluids 65 (1-3) (2011) 236–253. doi:10.1002/fld.2454.

[29] Y. Bazilevs, M.-C. Hsu, M. A. Scott, Isogeometric fluid-structure interaction analysis with emphasis on non-matching discretizations, and with application to wind turbines, Computer Methods in Applied Mechanics and Engineering 249-252 (2012) 28–41. doi:10.1016/j.cma.2012.03.028.

[30] M.-C. Hsu, Y. Bazilevs, Fluid-structure interaction modeling of wind turbines: simulating the full machine, Computational Mechanics 50 (6) (2012) 821–833. doi:10.1007/s00466-012-0772-0.

[31] J. Yan, A. Korobenko, X. Deng, Y. Bazilevs, Computational free-surface fluid-structure interaction with application to floating offshore wind turbines, Computers & Fluids 141 (Supplement C) (2016) 155–174. doi:10.1016/j.compfluid.2016.03.008.

[32] E. Ferede, M. M. Abdalla, G. J. W. Van Bussel, Isogeometric based framework for aeroelastic wind turbine blade analysis, Wind Energy 20 (2) (2016) 193–210. doi:10.1002/we.1999.

[33] Y. Bazilevs, V. M. Calo, Y. Zhang, T. J. R. Hughes, Isogeometric fluid-structure interaction analysis with applications to arterial blood flow, Computational Mechanics 38 (4-5) (2006) 310–322. doi:10.1007/s00466-006-0084-3.

[34] Y. Bazilevs, V. M. Calo, T. J. R. Hughes, Y. Zhang, Isogeometric fluid-structure interaction: theory, algorithms, and computations, Computational Mechanics 43 (1) (2008) 3–37. doi:10.1007/s00466-008-0315-x.

[35] Y. Bazilevs, J. R. Gohean, T. J. R. Hughes, R. D. Moser, Y. Zhang, Patient-specific isogeometric fluid-structure interaction analysis of thoracic aortic blood flow due to implantation of the Jarvik 2000 left ventricular assist device, Computer Methods in Applied Mechanics and Engineering 198 (45-46) (2009) 3534–3550. doi:10.1016/j.cma.2009.04.015.

[36] C. C. Long, A. L. Marsden, Y. Bazilevs, Fluid-structure interaction simulation of pulsatile ventricular assist devices, Computational Mechanics 52 (5) (2013) 971–981. doi:10.1007/s00466-013-0858-3.

[37] M.-C. Hsu, D. Kamensky, Y. Bazilevs, M. S. Sacks, T. J. R. Hughes, Fluid-structure interaction analysis of bioprosthetic heart valves: significance of arterial wall deformation, Computational Mechanics 54 (4) (2014) 1055–1071. doi:10.1007/s00466-014-1059-4.

[38] D. Kamensky, M.-C. Hsu, D. Schillinger, J. A. Evans, A. Aggarwal, Y. Bazilevs, M. S. Sacks, T. J. R. Hughes, An immersogeometric variational framework for fluid-structure interaction: Application to bioprosthetic heart valves, Computer Methods in Applied Mechanics and Engineering 284 (2015) 1005–1053. doi:10.1016/j.cma.2014.10.040.

[39] T. M. van Opstal, E. H. van Brummelen, G. J. van Zwieten, A finite-element/boundary-element method for three-dimensional,

large-displacement fluid-structure-interaction, Computer Methods in Applied Mechanics and Engineering 284 (2015) 637–663. doi:10.1016/j.cma.2014.09.037.

[40] L. Heltai, J. Kiendl, A. DeSimone, A. Reali, A natural framework for isogeometric fluid-structure interaction based on BEM-shell coupling, Computer Methods in Applied Mechanics and Engineeringdoi:10.1016/j.cma.2016.08.008.

[41] C. Politis, A. I. Ginnis, P. D. Kaklis, K. Belibassakis, C. Feurer, An isogeometric BEM for exterior potential-flow problems in the plane, in: 2009 SIAM/ACM Joint Conference on Geometric and Physical Modeling, SPM '09, ACM, New York, NY, USA, 2009, pp. 349–354. doi:10.1145/1629255.1629302.

[42] T. Takahashi, T. Matsumoto, An application of fast multipole method to isogeometric boundary element method for Laplace equation in two dimensions, Engineering Analysis with Boundary Elements 36 (12) (2012) 1766–1775. doi:10.1016/j.enganabound.2012.06.004.

[43] L. Heltai, M. Arroyo, A. DeSimone, Nonsingular isogeometric boundary element method for Stokes flows in 3D, Computer Methods in Applied Mechanics and Engineering 268 (2014) 514–539. doi:10.1016/j.cma.2013.09.017.

[44] R. N. Simpson, S. P. A. Bordas, J. Trevelyan, T. Rabczuk, A two-dimensional isogeometric boundary element method for elastostatic analysis, Computer Methods in Applied Mechanics and Engineering 209-212 (2012) 87–100. doi:10.1016/j.cma.2011.08.008.

[45] R. N. Simpson, M. A. Scott, M. Taus, D. C. Thomas, H. Lian, Acoustic isogeometric boundary element analysis, Computer Methods in Applied Mechanics and Engineering 269 (2014) 265–290. doi:10.1016/j.cma.2013.10.026.

[46] H. Lian, R. Simpson, S. Bordas, Stress analysis without meshing: isogeometric boundary element method, Proceedings of the ICE - Engineering and Computational Mechanics 166 (2) (2013) 88–99.

[47] M. A. Scott, R. N. Simpson, J. A. Evans, S. Lipton, S. P. A. Bordas, T. J. R. Hughes, T. W. Sederberg, Isogeometric boundary element analysis using unstructured T-splines, Computer Methods in Applied Mechanics and Engineering 254 (2013) 197–221. doi:10.1016/j.cma.2012.11.001.

[48] H. Lian, P. Kerfriden, S. P. A. Bordas, Implementation of regularized isogeometric boundary element methods for gradient-based shape optimization in two-dimensional linear elasticity, International Journal for Numerical Methods in Engineering (2015) n/a–n/adoi:10.1002/nme.5149.

[49] K. Li, X. Qian, Isogeometric analysis and shape optimization via boundary integral, Computer-Aided Design 43 (11) (2011) 1427–1437. doi:10.1016/j.cad.2011.08.031.

[50] S. Cho, S.-H. Ha, Isogeometric shape design optimization: exact geometry and enhanced sensitivity, Structural and Multidisciplinary Optimization 38 (1) (2008) 53–70. doi:10.1007/s00158-008-0266-z.

[51] L. Piegl, W. Tiller, The NURBS book, Springer Science & Business Media, 2012.

[52] L. Morino, Boundary integral equations in aerodynamics, Applied Mechanics Reviews 46 (8) (1993) 445–466. doi:10.1115/1.3120373.

[53] E. Klaseboer, C. R. Fernandez, B. C. Khoo, A note on true desingularisation of boundary integral methods for three-dimensional potential problems, Engineering Analysis with Boundary Elements 33 (6) (2009) 796–801. doi:10.1016/j.enganabound.2008.12.002.

[54] J. Katz, A. Plotkin, Low-speed aerodynamics, Cambridge University Press, 2001.

[55] M. Drela, XFOIL: An analysis and design system for low Reynolds number airfoils, in: T. J. Mueller (Ed.), Low Reynolds Number Aerodynamics, no. 54 in Lecture Notes in Engineering, Springer Berlin Heidelberg, 1989.

[56] I. H. Abbott, A. E. V. Doenhoff, Theory of wing sections, including a summary of airfoil data, Courier Corporation, 1959.

[57] R. Bouclier, T. Elguedj, A. Combescure, Locking free isogeometric formulations of curved thick beams, Computer Methods in Applied Mechanics and Engineering 245-246 (2012) 144–162. doi:10.1016/j.cma.2012.06.008.

[58] A. Cazzani, M. Malagù, E. Turco, Isogeometric analysis of plane-curved beams, Mathematics and Mechanics of Solidsdoi:10.1177/1081286514531265.

[59] A. Beckert, Coupling fluid (CFD) and structural (FE) models using finite interpolation elements, Aerospace Science and Technology 4 (1) (2000) 13–22. doi:10.1016/S1270-9638(00)00111-5.

[60] J. Moran, An introduction to theoretical and computational aerodynamics, John Wiley & Sons, 1984.

[61] H. Squire, A. Young, Air Ministry. Aeronautical Research Committee., The calculation of the profile drag of aerofoils., Aeronautical Research Committee reports and memoranda ; 1838; ARC technical report, HMSO, London, 1937.

[62] G. A. A. Thuwis, Stiffness and layout tailoring of a morphing high-lift system with aeroelastic loads, Ph.D. thesis, Delft University of Technology, Delft (Jun. 2012).

[63] K. Svanberg, A class of globally convergent optimization methods based on conservative convex separable approximations, SIAM Journal on Optimization 12 (2) (2002) 555–573. doi:10.1137/S1052623499362822.

[64] L. B. Rall, G. Goos, J. Hartmanis, W. Brauer, P. Brinch Hansen, D. Gries, C. Moler, G. Seegmller, J. Stoer, N. Wirth (Eds.), Automatic Differentiation: Techniques and Applications, Vol. 120 of Lecture Notes in Computer Science, Springer Berlin Heidelberg, Berlin, Heidelberg, 1981.

[65] G.-D. Kim, C.-S. Lee, J. E. Kerwin, A B-spline based higher order panel method for analysis of steady flow around marine propellers, Ocean Engineering 34 (14-15) (2007) 2045–2060. doi:10.1016/j.oceaneng.2007.02.013.

[66] V. Sladek, J. Sladek, Singular integrals in boundary element methods, Computational Mechanics Publications, 1998.

[67] J. C. F. Telles, Self-adaptive co-ordinate transformation for efficient nurmerical evaluation of general boundary element integrals, International Journal for Numerical Methods in Engineering 24 (5) (1987) 959–973.

[68] J. C. F. Telles, R. F. Oliveira, Third degree polynomial transformation for boundary element integrals: Further improvements, Engineering Analysis with Boundary Elements 13 (2) (1994) 135–141. doi:10.1016/0955-7997(94)90016-7.

[69] E. van der Weide, G. Kalitzin, J. Schlüter, J. Alonso, Unsteady turbomachinery computations using massively parallel platforms, in: 44th AIAA Aerospace Sciences Meeting and Exhibit, American Institute of Aeronautics and Astronautics, 2006, doi:10.2514/6.2006-421.

[70] J. Kiendl, K.-U. Bletzinger, J. Linhard, R. Wüchner, Isogeometric shell analysis with Kirchhoff-Love elements, Computer Methods in Applied Mechanics and Engineering 198 (49-52) (2009) 3902–3914. doi:10.1016/j.cma.2009.08.013.

[71] J. Kiendl, Y. Bazilevs, M.-C. Hsu, R. Wüchner, K.-U. Bletzinger, The bending strip method for isogeometric analysis of Kirchhoff-Love shell structures comprised of multiple patches, Computer Methods in Applied Mechanics and Engineering 199 (37-40) (2010) 2403–2416. doi:10.1016/j.cma.2010.03.029.

[72] W. Dornisch, S. Klinkel, On the choice of the director for isogeometric Reissner-Mindlin shell analysis, in: Blucher Mechanical Engineering Proceedings, Vol. 1, 2012, pp. 727–739.

[73] W. Dornisch, Interpolation of rotations and coupling of patches in isogeometric Reissner-Mindlin shell analysis, Ph.D. thesis, Lehrstuhls für Baustatik und Baudynamik der RWTH Aachen, Aachen (2015).

[74] S. T. IJsselmuiden, M. M. Abdalla, Z. Gürdal, Implementation of strength-based failure criteria in the lamination parameter design space, AIAA Journal 46 (7) (2008) 1826–1834. doi:10.2514/1.35565.

[75] J. N. Reddy, Mechanics of laminated composite plates and shells: Theory and analysis, 2nd Edition, CRC Press, 2004.

[76] G. J. Kennedy, G. K. W. Kenway, J. R. R. A. Martins, High aspect ratio wing design: Optimal aerostructural tradeoffs for the next generation of materials, in: 52nd Aerospace Sciences Meeting, American Institute of Aeronautics and Astronautics, 2014. doi:10.2514/6.2014-0596.

[77] A. Khani, S. T. IJsselmuiden, M. M. Abdalla, Z. Gürdal, Design of variable stiffness panels for maximum strength using lamination parameters, Composites Part B: Engineering 42 (3) (2011) 546–552. doi:10.1016/j.compositesb.2010.11.005.

[78] I. M. Daniel, O. Ishai, Engineering mechanics of composite materials, Oxford University Press, 2006.

[79] E. Gillebaart, R. De Breuker, Low-fidelity 2D isogeometric aeroelastic analysis and optimization method with application to a morphing airfoil, Computer Methods in Applied Mechanics and Engineering 305 (2016) 512–536. doi:10.1016/j.cma.2016.03.014.

[80] A. de Boer, A. H. van Zuijlen, H. Bijl, Review of coupling methods for non-matching meshes, Computer Methods in Applied Mechanics and Engineering 196 (8) (2007) 1515–1525. doi:10.1016/j.cma.2006.03.017.

[81] S. Shojaee, N. Valizadeh, E. Izadpanah, T. Bui, T.-V. Vu, Free vibration and buckling analysis of laminated composite plates using the NURBS-based isogeometric finite element method, Composite Structures 94 (5) (2012) 1677–1693. doi:10.1016/j.compstruct.2012.01.012.

[82] J. Mariens, A. Elham, M. J. L. van Tooren, Quasi-three-dimensional aerodynamic solver for multidisciplinary design optimization of lifting surfaces, Journal of Aircraft 51 (2) (2014) 547–558. doi:10.2514/1.C032261.

[83] A. Elham, Adjoint quasi-three-dimensional aerodynamic solver for multi-fidelity wing aerodynamic shape optimization, Aerospace Science and Technology 41 (2015) 241–249. doi:10.1016/j.ast.2014.12.024.

[84] J. I. Hileman, Z. S. Spakovszky, M. Drela, M. A. Sargeant, A. Jones, Airframe design for silent fuel-efficient aircraft, Journal of Aircraft 47 (3) (2010) 956–969. doi:10.2514/1.46545.

[85] C.-Y. Hu, T. Maekawa, N. M. Patrikalakis, X. Ye, Robust interval algorithm for surface intersections, Computer-Aided Design 29 (9) (1997) 617–627. doi:10.1016/S0010-4485(96)00099-1.

[86] A. van der Wees, J. van Muijden, J. van der Vooren, A fast robust viscous-inviscid interaction solver for transonic flow about wing/body configurations on the basis of full potential theory, in: 23rd Fluid Dynamics, Plasmadynamics, and Lasers Conference, Fluid Dynamics and Co-located Conferences, American Institute of Aeronautics and Astronautics, 1993. doi:10.2514/6.1993-3026.

[87] G. K. W. Kenway, G. J. Kennedy, J. R. R. A. Martins, Aerostructural optimization of the Common Research Model configuration, in: 15th AIAA/ISSMO Multidisciplinary Analysis and Optimization Conference, AIAA AVIATION Forum, American Institute of Aeronautics and Astronautics, 2014.

[88] T. Klimmek, Parametric set-up of a structural model for FERMAT configuration for aeroelastic and loads analysis, Journal of Aeroelasticity and Structural Dynamics 3 (2) (2014) 31–49.

[89] C. Kassapoglou, Design and analysis of composite structures: With applications to aerospace structures, John Wiley & Sons, 2013.

[90] J. K. S. Dillinger, Static aeroelastic optimization of composite wings with variable stiffness laminates, Ph.D. thesis, Delft University of Technology, Delft (2014).

[91] R. P. Liem, G. K. W. Kenway, J. R. R. A. Martins, Multimission aircraft fuel-burn minimization via multipoint aerostructural optimization, AIAA Journal 53 (1) (2014) 104–122. doi:10.2514/1.J052940.

[92] N. P. M. Werter, Aeroelastic modelling and design of variable stiffness composite and morphing wings, Ph.D. thesis, Delft University of Technology, Delft (2017).

[93] D. M. J. Peeters, Design optimisation of practical variable stiffness and thickness laminates, Ph.D. thesis, Delft University of Technology, Delft (2017). doi:10.4233/uuid:a07ea6a4-be73-42a6-89b5-e92d99bb6256.

[94] J. R. R. A. Martins, J. T. Hwang, Review and unification of methods for computing derivatives of multidisciplinary computational models, AIAA Journal 51 (11) (2013) 2582–2599. doi:10.2514/1.J052184.

[95] M. Hojjat, E. Stavropoulou, K.-U. Bletzinger, The Vertex Morphing method for node-based shape optimization, Computer Methods in Applied Mechanics and Engineering 268 (Supplement C) (2014) 494–513. doi:10.1016/j.cma.2013.10.015.

[96] D. Baumgärtner, A. Viti, A. Dumont, G. Carrier, K.-U. Bletzinger, Comparison and combination of experience-based parametrization with Vertex Morphing in aerodynamic shape optimization of a forward-swept wing aircraft, in: 17th AIAA/ISSMO Multidisciplinary Analysis and Optimization Conference, June, 2016.

[97] V. P. Nguyen, P. Kerfriden, M. Brino, S. P. A. Bordas, E. Bonisoli, Nitsches method for two and three dimensional NURBS patch coupling, Computational Mechanics 53 (6) (2014) 1163–1182. doi:10.1007/s00466-013-0955-3.

[98] W. Dornisch, G. Vitucci, S. Klinkel, The weak substitution method - an application of the mortar method for patch coupling in NURBS-based isogeometric analysis, International Journal for Numerical Methods in Engineering 103 (3) (2015) 205–234. doi:10.1002/nme.4918.

[99] L. Coox, F. Greco, O. Atak, D. Vandepitte, W. Desmet, A robust patch coupling method for NURBS-based isogeometric analysis of non-conforming multipatch surfaces, Computer Methods in Applied Mechanics and Engineering 316 (Supplement C) (2017) 235–260. doi:10.1016/j.cma.2016.06.022.

[100] J. Kiendl, R. Schmidt, R. Wüchner, K.-U. Bletzinger, Isogeometric shape optimization of shells using semi-analytical sensitivity analysis and sensitivity weighting, Computer Methods in Applied Mechanics and Engineering 274 (2014) 148–167. doi:10.1016/j.cma.2014.02.001.

[101] B. A. Cipra, The best of the 20th century: Editors name top 10 algorithms, SIAM News 33 (4) (2000) 1–2.

[102] Y. J. Liu, N. Nishimura, The fast multipole boundary element method for potential problems: A tutorial, Engineering Analysis with Boundary Elements 30 (5) (2006) 371–381. doi:10.1016/j.enganabound.2005.11.006.

LIST OF PUBLICATIONS

JOURNAL PUBLICATIONS

1. E. Gillebaart and R. De Breuker (2016), "Low-fidelity 2D isogeometric aeroelastic analysis and optimization method with application to a morphing airfoil", *Computer Methods in Applied Mechanics and Engineering*, vol. 305, pp. 512-536.

2. E. Gillebaart and R. De Breuker, "Geometrically consistent static aeroelastic simulation using isogeometric analysis", *Computer Methods in Applied Mechanics and Engineering*, under review.

3. D. Rajpal, E. Gillebaart and R. De Breuker, "Preliminary aeroelastic design framework for composite wings subjected to gust loads", *Journal of Composites*, to be submitted.

CONFERENCE PUBLICATIONS

1. E. Gillebaart and R. De Breuker, "Reduced-Order modeling of continuous-time state-space unsteady aerodynamics", In *Proceedings of 53rd AIAA Aerospace Sciences Meeting*, Kissimmee, Florida, USA.

2. E. Gillebaart and R. De Breuker, "Low-fidelity 2D isogeometric aeroelastic analysis and optimization method with application to a morphing airfoil", In *Proceedings of the International Forum on Aeroelasticity and Structural Dynamics 2015*, St. Petersburg, Russia.

ACKNOWLEDGEMENTS

The PhD project has been a tough nut to crack and only because of the help and support of many people around me have I been able to reach the finish line successfully. First of all, I would like to thank dr. Roeland De Breuker for supervising me during the challenging project this has been. Our cooperation started with my master thesis and continued with the PhD for a total duration of about 6 years. During this time you have always had confidence in my abilities as a researcher, especially in times where my own confidence was fading. With a healthy dose of humour, you always manage to see the positive side of things, resulting in many enjoyable meetings and conversations over the years.

I would like to thank prof. Chiara Bisagni for being my promotor and for helping me to improve the quality of my research. I would also like to thank the committee members, prof. Veldhuis, prof. van Brummelen, prof. Krüger, dr. Woods, and prof. Vuik for taking the time to read my thesis and for being part of my PhD defence committee.

My gratitude also extends to the rest of the staff of the ASCM department for providing an enjoyable environment both in the office and at social activities. Special thanks go to Laura for always being ready to help or give directions and information when it comes to the more practical sides of the PhD.

I would like to thank my fellow PhDs and post-docs for the technical discussions we had, and the time we spent both at and outside work. The conference trips were always much more enjoyable with your good company, and lunch is not complete without one of our discussions about a great variety of subjects. The regular LAN parties were an excellent way to vent some frustration and to have a great time.

Of course, I would also like to express my appreciation to my parents and brother and sister. I always enjoy our time together. All of you provided a listening ear in the times I needed it the most, enabling me to reach the finish of the PhD. Without your love and support this would have been impossible.

BIOGRAPHICAL NOTE

Erik Gillebaart was born on January 31, 1989 in Heemskerk, the Netherlands. He went to Jac P. Thijsse College in Castricum, the town where he grew up. After finishing high school he decided to study Aerospace Engineering at the Delft University of Technology. After half a year of travelling back and forth between Castricum and Delft, he decided to move to Delft. In 2010 he obtained his Bachelor of Science degree with distinction.

The next step in Erik's educational career was to start a master at the chair of Aerospace Structure and Design Methodologies, now known as Aerospace Structures and Computational Mechanics. In the second year of his master, he did a three month internship at Tata Steel in IJmuiden. At the research and development department, he worked on modelling the temper rolling process using the finite element method, focussing on how the roughness was transferred from the roll to the sheet material.

After his return to the university, he started his graduation project entitled *Optimisation of an Articulated Mechanism for a Morphing Winglet* under the supervision of dr. Roeland De Breuker. The topology optimisation of truss-based mechanisms was investigated and used to develop a mechanism suitable for morphing the winglet on an aircraft wing to improve the aerodynamic efficiency. Erik graduated in January 2013.

During his master he enjoyed doing research, so when his supervisor dr. Roeland De Breuker offered him a PhD position, he did not have to think about it for long. This very dissertation on geometrically consistent aerostructural optimisation using isogeometric analysis is the result of his PhD project.